POWER-FACTOR IMPROVEMENT IN CAGE INDUCTION MOTORS

by

Nicholas K. Adams B.Sc. (Eng.)

Thesis submitted for
The Degree of Doctor of Philosophy
in the Faculty of Engineering
University of London

Imperial College of Science and Technology
London

March 1987

ABSTRACT

The work described in this thesis may be divided into two parts. The first is concerned with power-factor improvement in induction motors by means of subharmonic fields, and the second with the analysis of cage machines with inter-rings.

The principle of using additional airgap fields to reduce reactive power consumption is reviewed in Section 2. It is shown how forwards-rotating subharmonic fields satisfy derived conditions for effective rotor power-factor improvement. The analysis of the inter-ring machine is presented in Section 3. It is based on a coupling-impedance technique, in which the rotor is modelled as a series of skewed loops.

Section 4 describes the method used to select a prototype motor suitable for an experimental investigation of power-factor behaviour. A design procedure is formulated which allows separate main and subharmonic windings to be incorporated into the stator of the original machine.

Experimental results obtained from the rewound prototype motor are presented in Section 5. It is demonstrated that the use of subharmonic fields may be beneficial in multipole machines. Section 5 also describes the verification of the inter-ring analysis. Experimental justification is provided by a series of steady-state performance tests on the original machine, and by a search-coil study of airgap flux density. The relationship between inter-rings and skew is further examined in Section 8.

ACKNOWLEDGEMENTS

I should like to thank Dr. S. Williamson for his invaluable help and guidance throughout this project. Thanks are also extended to fellow students and staff for participating in many useful discussions.

Acknowledgements are also due to the various machine designers at Bull Electric for their assistance in providing practical design details and the prototype motor, and to the Science and Engineering Research Council for their financial support.

TABLE OF CONTENTS

1. Introduction 8

2. Theoretical background 13

2.1 General discussion of power-factor improvement 13

2.2 Effect of the subharmonic field 15

3. Inter-ring analysis 24

3.1 Approach - rotor-loop model and assumptions 29

3.2 Formulation of coupling-impedance equations 30

3.3 Impedance calculations 34

3.3.1 Stator impedances 34

3.3.2 Rotor impedances 44

3.4 Steady-state performance 55

3.5 Search coil EMFs 67

3.6 Computer implementation 70

4. Investigation of power-factor improvement 71

4.1 Objective 71

4.2 Selection of prototype machine 72

4.3 Design of subharmonic winding 89

5. Experimental investigation and verification 102

5.1 Scope of experimental work 102

5.2 Verification of inter-ring analysis 103

5.2.1 Test procedure 105

5.2.2 Performance tests 108

5.2.3 Search-coil verification 113

5.3 Power-factor improvement 128

6. Conclusions 144

7. References 147

8. Appendices 151

8.1 Self-compensating induction motor tests 151

8.2 Conductor-density distributions 166

8.3 Magnetic-circuit calculations 169

8.4 Inter-ring effects 174

LIST OF PRINCIPAL SYMBOLS

a	band width
A	conductor density
b,B	flux density
c,C	conductor density
d	airgap diameter
e,E	electric field strength
f	supply frequency
g	airgap length
G	goodness factor
h	magnetic path length
H	magnetic field strength
i,j	band number
i,I	winding current
j	complex operator
j,J	surface-current density (MMF)
k,l,q	wavenumber
K	skew factor
K_b	slot-mouth width factor
l	length
m,n	winding number
M	number of coils per winding
N_b	number of bands
N_c	number of turns per coil
N_r	number of rotor bars
N_s	number of stator windings
P	active power (watts)
Q	reactive power (VArs)
r	contribtution from subharmonic field
R	resistance
s	per unit slip

S	complex (apparent) power
t	time
T	torque, input VArs to output watts ratio
u,U	induced EMF
v,V	applied voltage
w	effective machine length
x	band position
x,y,z	rectangular co-ordinates
Y,W	admittance
Z	impedance
α	coil pitch
β	phase axis position
γ	angle of skew
δ	relative coil position, peripheral skew
η	efficiency
θ	angular displacement
λ	power factor, slot pitch
μ_o	permeability of free space
υ	harmonic number
ρ	resistivity
σ	conductivity
φ	power-factor angle
Φ	magnetic flux
ω	supply angular frequency, rotor speed
ωT	rotor-leakage time constant

Subscripts

a	airgap, inter-ring
b,bar	bar
c	search coil, core
er	end-ring
g	airgap

i,j	band number
ir	inter-ring
k,l,q	wavenumber
m,n	winding number
r	rotor
s	stator
t	tooth, total
x,y,z	reactangular co-ordinates

Superscripts

a,A	airgap
k,l,q	wavenumber

-	denotes a complex quantity
Re	denotes 'real part of'
Im	denotes 'imaginary part of'
*	denotes 'complex conjugate of'
$\wedge$	denotes 'peak value of'

1. INTRODUCTION

Of all the different types of electrical machine, the squirrel-cage induction motor provides by far the greatest proportion of the world's total electrical drive output. A simply-constructed, robust rotor needing no electrical connection with the outside world is undoubtedly the chief reason for its success. Its two principal drawbacks are well known. The first concerns speed control and the second power factor.

The cage induction machine is capable of high efficiency only when operated over a limited range of speeds determined by its supply frequency and stator winding arrangement. Modern developments in solid-state, variable-frequency inverters provide a solution to this problem, but the inability of the induction motor to operate at anything other than lagging power factor makes such drives expensive and potentially unreliable. It is considerably easier and cheaper to supply a unity or leading power-factor load than a lagging one, as witnessed by the use of the over-excited synchronous machine in many variable-speed applications. The key point is that the inverter can be self-commutating at other than very low speeds, the motor itself drawing current at a leading power factor. The penalty paid for using a standard squirrel-cage motor as the prime mover is the present need for complicated forced-commutation circuitry or large capacitor banks. The advantage of dependable, maintenance-free operation under hazardous environmental conditions is somewhat negated by the reliability problems associated with variable-frequency induction motor drives. Cage machines capable of running at high lagging, or even leading, power factors would thus be highly desirable.

Even with sinusoidal supplies, the advantages of improved power-factor operation are considerable. Low power factor adversely affects power system performance in several ways. The physical size of generation and transmission equipment is largely determined by its voltage and current rating, regardless of power factor. High currents mean more losses and poor voltage regulation. Electricity supply authorities often encourage large industrial users to keep their reactive power requirements manageable by imposing tarrifs that penalise low power-factor loads.

In recent work on power-factor improvement, Laithwaite and Kuznetsov [1-3] claimed to have produced unity power-factor operation of a plain cage-rotor induction machine, using special windings occupying part of the stator periphery. The resulting VAr-generation effect was harnessed by driving the so-called 'self-compensating induction motor' from a simple six-step current-source inverter [4-7]. The previous need for power diodes and capacitors [8] was removed by natural load commutation of the inverter thyristors. A generalised theory capable of accommodating any stator winding configuration was subsequently developed by Williamson [9], whose work indicated that a cage induction motor must always draw positive VArs from the supply. Clearly, a conflict of opinions existed.

It was with this background that a CASE project was set up in collaboration with Bull Electric to investigate the general subject of power-factor improvement in cage-rotor induction machines. The work carried out under this project forms the main theme of this thesis.

The test motor used by Laithwaite and Kuznetsov [3,7] was still available at Imperial College; this afforded the opportunity to check their work experimentally. Compre-

hensive sinusoidal tests consistently failed to give any indication of possible unity power-factor operation. A current-source inverter was designed, built and tested to the same specification as that given by Kuznetsov [4-7]. Considerable external capacitance was needed to effect commutation of the inverter thyristors. The author was therefore led to support the theoretical conclusions arrived at by Williamson. This experimental investigation, carried out in the first year of the project, is not particularly relevant to the remainder of the thesis, and is detailed in Appendix 8.1.

During his theoretical investigation of the limits of power-factor improvement, Williamson [9] noted that it might be feasible to reduce reactive power input by introducing subharmonic fields into the airgap. He showed that whilst an improvement in airgap power factor could indeed be achieved using this technique, the degree of improvement, and the cost in terms of efficiency, was largely a matter of detailed design. Bull Electric agreed that the possibility of using subharmonic fields as a method of power-factor improvement should be investigated using one of their standard production motors.

Already an established manufacturer of DC machines, Bull have, in recent years, developed and produced a series of small- to medium-sized (4-100 kW) squirrel-cage induction motors, intended for lift applications. The range comprises singly- and doubly-wound machines, exploiting high resistance cages and deep-bar effects to obtain the kind of torque-speed characteristic required for variable-voltage, fixed-frequency speed control. A novel feature incorporated into the entire range of AC motors is the use of copper or brass bars, together with one or more bar-to-bar conducting

rings positioned equidistantly along the axial length of the rotor. The purpose of these 'inter-rings' is far from clear, since Bull themselves take no account of their effects in performance predictions. It is generally thought that their inclusion helps to reduce noise, a benefit of particular significance in lift applications.

In predicting the effects of the VAr-reducing sub-harmonic field, it was necessary to extend previous analyses [9,10] to accommodate rotors with inter-rings. The work presented in this thesis may therefore be divided into two parts. The first is the development and verification of an harmonic analysis of cage-rotor induction machines with inter-rings; the second, an investigation into the use of subharmonic fields as a method of power-factor improvement.

Section 2 attempts to clarify the relationship between active and reactive power flow in AC circuits, and introduces the concept of the subharmonic field as the VAr-reducing element. The analysis of the inter-ring machine is presented in Section 3. It is based on the coupling-impedance approach of Williamson and Laithwaite [10], whose representation of the rotor cage by a single bar is replaced by a loop model [11], considerably modified to include the effect of rotor inter-rings.

The process of selecting a candidate motor for power-factor improvement took the form of an investigation of rotor power factor and efficiency for each single-winding machine in the Bull range. This procedure, along with the design of the appropriate subharmonic winding, is detailed in Section 4.

Practical verification of the theoretical model was provided in part by a series of performance tests carried out on the prototype machine, as supplied by Bull. The

ability of the analysis to take inter-rings into account was further demonstrated by a search-coil study of airgap flux density. The effect of the subharmonic field on power factor, efficiency, etc., was investigated experimentally using a 'before-and-after' comparison. After the initial tests, the prototype motor was rewound to the appropriate subharmonic specification, and subsequently re-tested. Section 5 describes the practical work carried out.

2. THEORETICAL BACKGROUND

2.1 General discussion of power-factor improvement

The ideal power-factor improvement scheme is one in which reactive power consumed by an electrical machine is reduced without affecting active power flow. This is realised in practice by parallel connection of power-factor correction capacitors or synchronous compensators. An increase in power factor is obtained with no detrimental effect on efficiency.

However, a reduction in VAr demand is not the only way in which the power factor of an electrical machine can be improved. To illustrate this, consider a resistor connected in parallel with an induction motor excited from a constant voltage supply. For the purpose of this discussion it is convenient to express efficiency and power factor in terms of output watts P_{out}, input VArs Q_{in} and watts loss P_{loss} :

$$\eta = \frac{P_{out}}{P_{out} + P_{loss}} \; ; \qquad (2.1)$$

$$\lambda = \frac{1}{\sqrt{\left\{1 + \left(\frac{Q_{in}}{P_{out} + P_{loss}}\right)^2\right\}}} \; . \qquad (2.2)$$

The additional heat dissipated in the resistor increases the losses, although no change in output power is observed. As verified by eqn.2.1, poorer overall efficiency is the result. Despite the fact that the reactive power consumed at the machine terminals remains unaltered by the inclusion of the resistor, eqn.2.2 shows that the power factor has been improved. Such a scheme is clearly undesirable, since no

reduction in the size and weight of the compensation equipment is achieved. An improvement in power factor has been obtained simply by increasing the losses.

To a large extent, the physical size of an electric motor is determined by the active power loss which it can tolerate at rated speed. This loss is dissipated chiefly in the form of heat. Excessive temperature rises lead to insulation breakdown and eventual operational failure. It is therefore essential that losses be kept constant, or, better still, reduced, while attempts are made to improve power factor. In addition, the constraint of constant losses prevents the occurrence of the misleading situation described above, since the only way in which an improvement in power factor may then be obtained is by a reduction in input VArs. Machine derating and poorer efficiency result if such an improvement is accompanied by a reduction in output.

The feasibility of a scheme in which the reactive power demand is decreased at the expense of active power output depends upon the application. Consider, for example, a variable-frequency inverter feeding a cage-rotor induction machine. There is a trade-off between the reduction in size, weight and cost of inverter commutation circuitry on the one hand, and machine derating on the other. It is a question of economics whether the improvement in power factor justifies the accompanying reduction in output.

A suitable quantitative description of the ability of a particular method to improve power factor is provided by the ratio Q_{in}/P_{out}. In the following analytical treatment, an explicit expression for this quantity is derived for the specific case of a squirrel-cage induction motor.

2.2 Effect of the subharmonic field

In a recent paper, Williamson [9] discussed the theoretical possibility of using forwards-rotating subharmonic fields as a means of power-factor improvement. He developed an harmonic model of the cage-rotor induction machine, believed valid for any winding configuration and supply connection, to show that a cage motor always absorbs reactive power from the supply. Section 3 of this thesis derives a similar model suitably modified for application to the Bull Electric range of machines, but at this stage the conventional equivalent circuit serves as an introduction.

The stator of a standard induction motor carries one or more windings wound for a particular number of poles. Full-load torque is obtained at rated speed corresponding to a small slip as defined for the principal pole number. If the order of the harmonic under consideration is ν_k, corresponding to a p-pole field, the associated wavenumber is defined as

$$k = 2\nu_k/d = p/d \ . \qquad (2.3)$$

The complex power flowing into the airgap from the stator on the principal pole number may be written as

$$\bar{S}_a^{k1} = P_a^{k1} + jQ_a^{k1} . \qquad (2.4)$$

Since the machine is operating as a motor, it absorbs active and reactive power, so that P_a^{k1}, $Q_a^{k1} > 0$. The airgap power factor* angle therefore satisfies the inequality

$$0 < \varphi_a^{k1} < \pi/2 \ .$$

The situation is illustrated graphically in Fig.2.1a. In the absence of any other harmonic fields, the airgap power factor

* The ν_{k1}-th harmonic airgap power factor is defined formally by eqn. 4.16 (page 79)

is cos φ_a^{k1}.

Suppose that an additional harmonic field is introduced into the airgap. The total complex power is now

$$\bar{S}_a = \bar{S}_a^{k1} + \bar{S}_a^{k2}, \qquad (2.5)$$

where

$$\bar{S}_a^{k2} = P_a^{k2} + jQ_a^{k2}. \qquad (2.6)$$

VArs are consumed on the additional pole-number wave, and so $Q_a^{k2} > 0$. The conditions under which additional active power is **generated**, i.e., $P_a^{k2} < 0$, are illustrated in Fig.2.1b, from which it is evident that a poorer overall power factor cos φ_a is obtained. The two cases that result from the **consumption** of active power by the extra harmonic field are shown in Figs. 2.1c and d. In Fig.2.1c, the power factor of the additional harmonic field is greater than that of the principal harmonic, whereas in Fig.2.1d, the reverse is true.

Inspection of Figs.2.1b-d indicates that there are two conditions which should be satisfied if an improvement in airgap power factor is to be achieved:

(i) active power must be consumed, not generated, by the additional harmonic field;

(ii) the airgap power factor for the additional pole number must be greater than that for the principal pole number ($\varphi_a^{k2} < \varphi_a^{k1}$).

Recalling the discussion of Section 2.1, it is also important to consider the ratio of input VArs to output

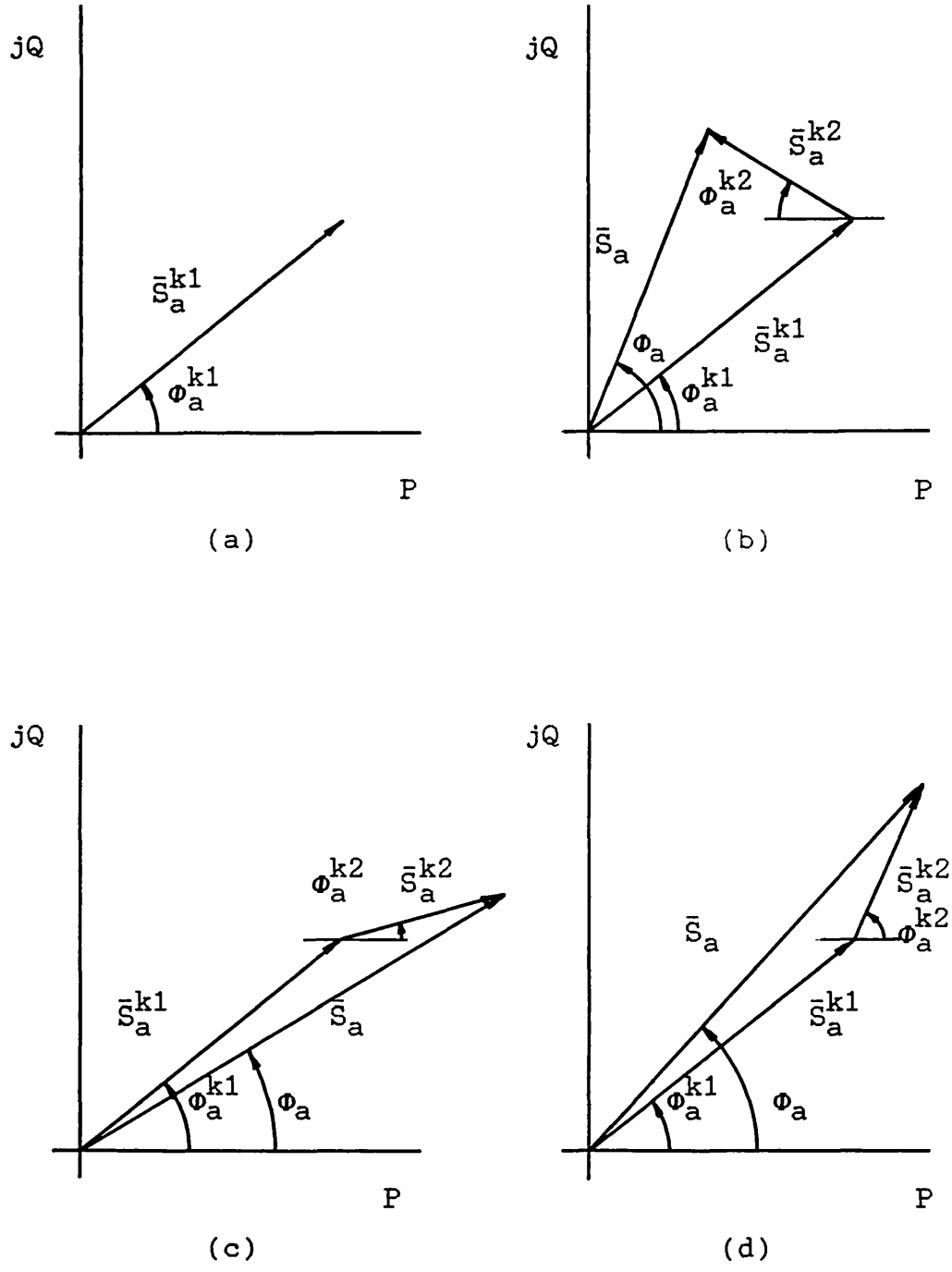


Fig.2.1: Conditions necessary for power-factor improvement

watts. In the presence of two harmonic fields, the total reactive power flowing into the airgap from the stator is

$$Q_{in} = Q_{in}^{k1} + Q_{in}^{k2} \quad . \tag{2.7}$$

The output power may be similarly expressed:

$$P_{out} = P_{out}^{k1} + P_{out}^{k2} \quad . \tag{2.8}$$

If the addition of the extra harmonic field is to improve the input VArs to output watts ratio, the following inequality must hold

$$\frac{Q_{in}}{P_{out}} < \frac{Q_{in}^{k1}}{P_{out}^{k1}} ,$$

i.e.,

$$\frac{Q_{in}^{k1} + Q_{in}^{k2}}{P_{out}^{k1} + P_{out}^{k2}} < \frac{Q_{in}^{k1}}{P_{out}^{k1}} ,$$

i.e.,

$$\frac{Q_{in}^{k2}}{P_{out}^{k2}} < \frac{Q_{in}^{k1}}{P_{out}^{k1}} \quad . \tag{2.9}$$

An additional requirement for **effective** airgap power-factor improvement may now be stated. The ratio of VArs input to watts output on the additional pole number must be less than that on the principal pole number.

As a first approximation, the usual per-phase equivalent circuit of Fig.2.2 can be used to investigate the feasibility of satisfying the conditions stated above.

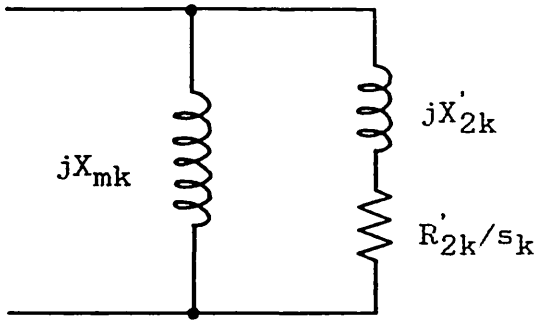


Fig.2.2 Harmonic rotor branch of standard equivalent circuit

Harmonic dependence of rotor parameters is indicated by adding the wavenumber subscript k to the usual notation. It is useful to introduce two related quantities; the goodness factor, defined [12] by

$$G_k = \frac{X_{mk}}{R'_{2k}} = \frac{\omega \mu_0 w N_r}{k^2 g \pi d R_r^k} , \qquad (2.10)$$

and the rotor-leakage time constant:

$$\omega T_k = \frac{X_{2k}}{R'_{2k}} = \frac{X_r^k}{R_r^k} . \qquad (2.11)$$

In eqns. 2.10 and 2.11,

$$R_r^k = \Phi R_{bar} + \frac{R_{er}}{2N_r \sin^2(\frac{\pi \nu_k}{N_r})} , \qquad (2.12)$$

and

$$X_r^k = \Psi X_{slot} . \qquad (2.13)$$

R_{bar} and R_{er} are the low-frequency values of rotor bar and end-ring resistance, respectively. X_{slot} is the DC slot leakage reactance per bar, and Φ and Ψ are skin-effect

correction factors [13].

The ν_k-th harmonic airgap power factor can now be written as

$$\lambda_k = \sqrt{\left\{ \frac{s_k^2 G_k^2}{s_k^2 G_k^2 + \{1 + s_k^2 \omega T_k (G_k + \omega T_k)\}^2} \right\}} , \qquad (2.14)$$

while the input VArs to output watts ratio may be similarly expressed: .

$$\frac{Q_{in}^k}{P_{out}^k} = \frac{1 + s_k^2 \omega T_k (G_k + \omega T_k)}{s_k (1 - s_k)\, G_k} . \qquad (2.15)$$

The ν_k-th harmonic rotor efficiency is

$$\eta_k = 1 - s_k . \qquad (2.16)$$

Airgap fields produced by the stator winding currents may be categorised according to their relative harmonic order and direction of rotation. A **superharmonic** field has a pole number greater than that of the principal harmonic, whilst a **subharmonic** field has less than the principal number of poles. A forwards-rotating harmonic is one which travels in the same direction as the principal pole-number wave.

Eqns. 2.10 to 2.16 can be used to investigate the effects of introducing each of these types of harmonic field into the airgap of a machine. As an example, consider a typical induction motor from the Bull Electric range, detailed in Table 2.1. Values of airgap power factor, efficiency, etc., calculated at the rated speed of 1398 rpm, are compared in Table 2.2.

Table 2.1: Specification of sample motor

Principal poles	4
Rated slip	6.8 %
Rated output	3.9 kW
Supply frequency	50 Hz
Effective core length	71.3 mm
Airgap length	0.65 mm
Number of rotor slots	59
Mean airgap diameter	164.4 mm
Rotor slot width	2.3 mm
Rotor slot depth	16 mm
Bar width	2 mm
Bar resistivity (hot)	2.39×10^{-8} Ωm
End-ring width	20 mm
End-ring depth	8.5 mm
End-ring resistivity (hot)	7.50×10^{-8} Ωm

Table 2.2: Calculated performance of sample machine at rated speed

Harmonic	principal	sub-	super-	principal	sub-	super-
Direction of rotation	FORWARDS			BACKWARDS		
Goodness factor	34.3	44.1	24.1	26.9	42.0	15.7
Rotor leakage time constant	0.416	0.130	0.648	0.257	0.109	0.316
Airgap power factor	0.909	0.994	0.938	0.887	0.985	0.782
VArs input/ watts output	0.491	0.241	-0.264	-0.558	-0.377	-0.564
Rotor efficiency	0.932	0.466	1.398	-0.932	-0.466	-1.391

For the backwards-rotating harmonics, active power is absorbed from the mechanical load, producing a braking effect. The electrical input power, although positive, is insufficient to supply the rotor copper losses. This is the so-called **plugging** condition, indicated in Table 2.2 by the presence of negative efficiencies and input VArs to output watts ratios. Although conditions (i) and (ii) above are satisfied in the case of the backwards-rotating subharmonic field, efficiency penalties prohibit the use of plugging harmonics.

Of the forwards-rotating fields, the superharmonic wave generates active power, violating condition (ii). At 1398 rpm, the superharmonic torque and slip are negative, confirmed in Table 2.2 by a negative input VArs to output watts ratio and an apparent rotor efficiency of more than 100%. The forwards-rotating subharmonic wave is thus seen to be the only practical possibility. Over the range of speeds corresponding to motoring operation, active power input on the subharmonic pole number is positive, meeting condition (i). Table 2.2 shows that condition (ii) is satisfied, and the ratio of rotor input VArs to output watts is also reduced. It can therefore be confidently predicted that the inclusion of a 2-pole subharmonic field will produce an effective improvement in airgap power factor at rated speed.

It is interesting to note, however, that this is not the case at all speeds. Fig.2.3 shows the variation of rotor power factor and VArs/watts ratio for principal slips between 0 and 1. Although the subharmonic airgap power factor exceeds that of the principal harmonic, no advantage is gained for speeds from 800 to 1200 rpm. Over this range, power factor improvement is achieved solely at the expense of active input power, since no reduction in the ratio of

input VArs to output watts is observed. In effect, the airgap power factor is improved simply by increasing the losses, as discussed in Section 2.1.

Attention has to date been focussed on conditions existing in the airgap as a result of rotor action alone. In order to study the effects of subharmonic fields on the overall, **terminal** power factor, it is necessary to consider the way in which the stator conductors should be arranged to produce the additional harmonic field. It is also important to develop a more accurate model of the machine under investigation.

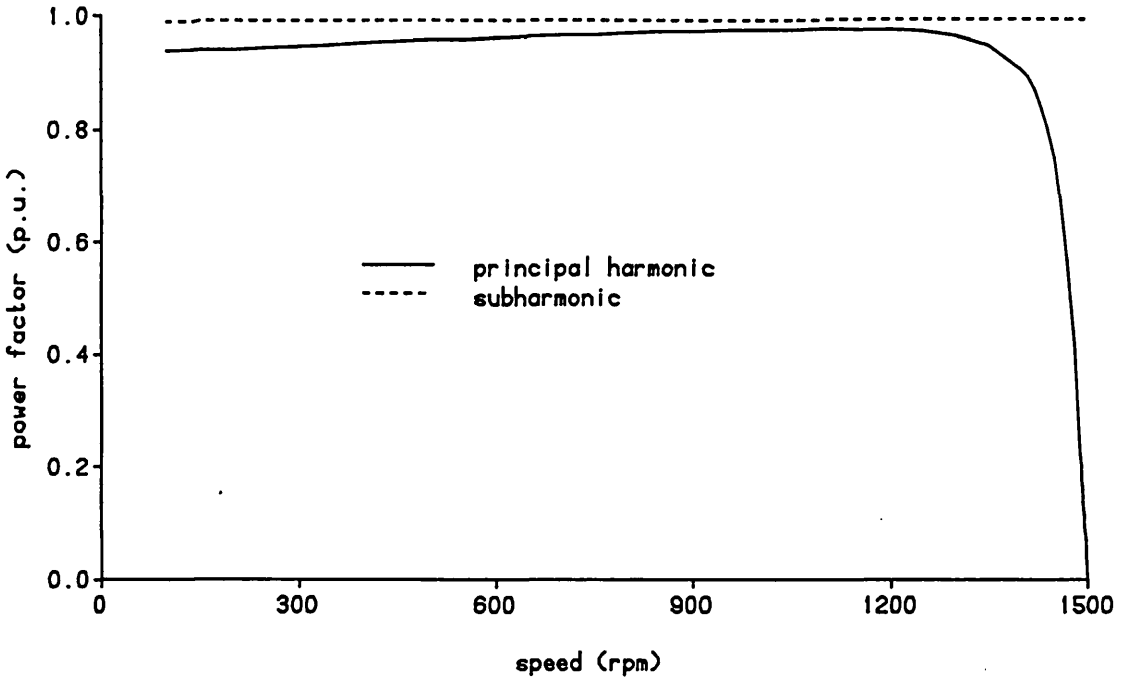


Fig.2.3a: Airgap power factor

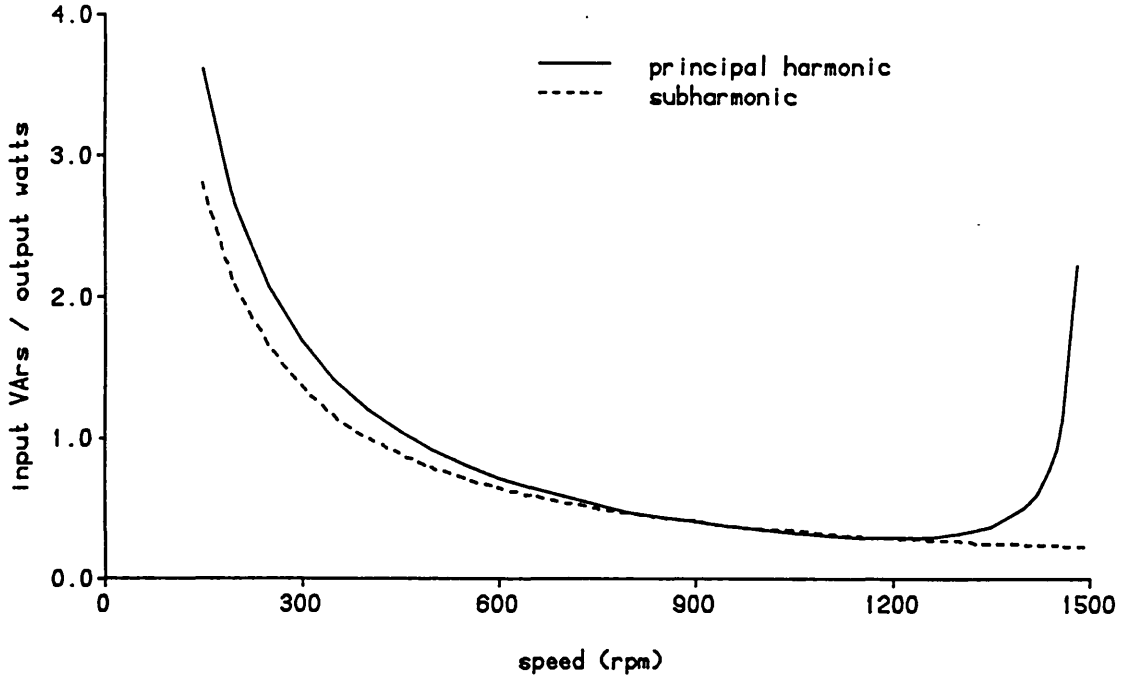


Fig.2.3b: Airgap input VArs to output watts ratio

3 INTER-RING ANALYSIS

3.1 Approach - Rotor-Loop Model and Assumptions

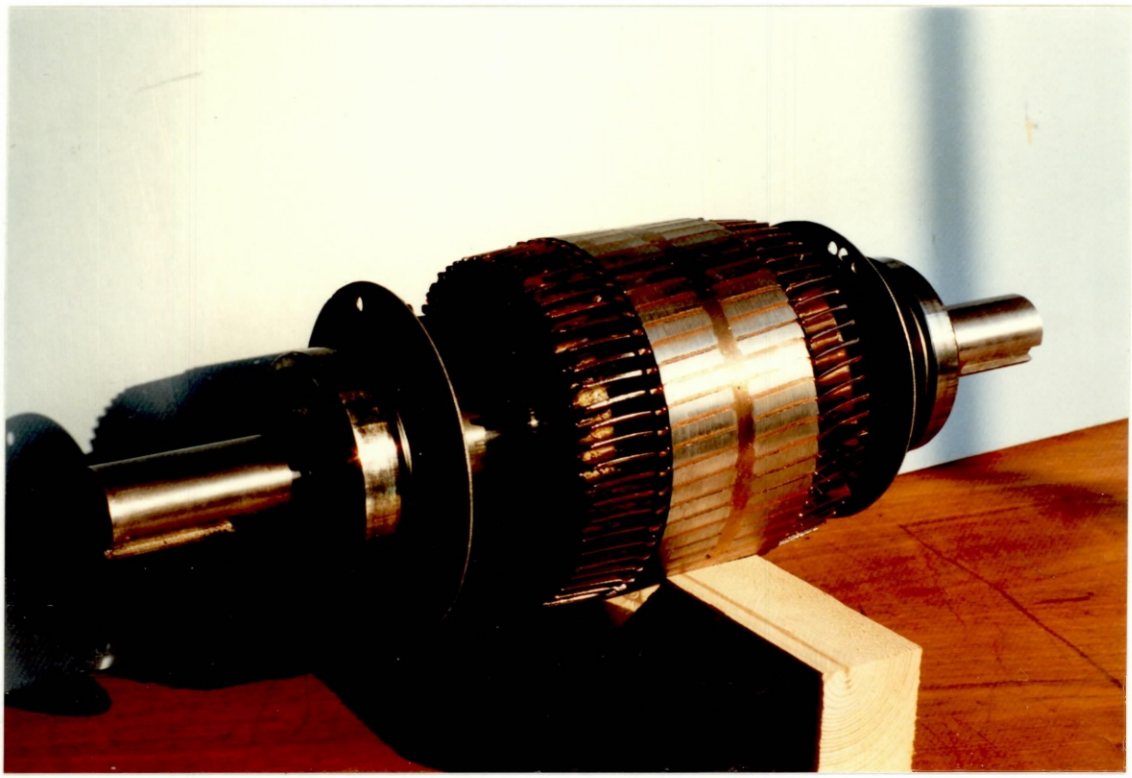
The analysis developed in this section is based on an harmonic impedance technique, in which the machine is modelled as a series of coupled linear circuits. Rotating-field theory is used to calculate impedances relating the EMFs induced in any one circuit to currents flowing in all the others. A general harmonic approach is adopted, suitable for investigating the effects of the VAr-reducing sub-harmonic field.

The stator is assumed to carry N_s windings, each of which can be thought of as a circuit, closed on itself by the supply connection. For the purposes of this analysis, a **winding** is defined as any series-connected set of coils, placing no restriction on the arrangement of stator conductors. The concept of a circuit is, however, a little less obvious when the squirrel-cage construction is being considered. Currents flowing in the stator windings establish a spectrum of sinusoidally-distributed, synchronously-rotating harmonic fields. Each such field induces EMFs in the rotor bars, resulting in a particular rotor-current distribution. Due to the symmetry of the cage, each distribution may be defined by the current flowing in one reference bar. The whole distribution is then obtained using a bar-to-bar phase shift. In this approach, the rotor bars are assumed to be insulated from the iron, precluding the possibility of inter-bar currents contributing to the overall distribution.

As mentioned in Section 1, the induction motors manufactured by Bull Electric for lift and industrial (fan-drive) applications incorporate bar-to-bar conducting

rings spaced at equidistant intervals along the axial length of the rotor (Fig.3.1). The cages of these machines are also skewed, and circumferentially-directed currents flow from bar to bar as a result. The number of 'inter-rings' varies with the length of the machine. The smallest machines, with core lengths of 150mm or less, have only one, whilst those with core lengths of over 250mm have three. During manufacture, the partially-assembled rotor is mounted in a lathe, and one or more slots are machined around the periphery. These slots are filled with copper braze to form conducting paths, and the rotor is then machined to the correct diameter.

To allow for the presence of inter-ring currents, it is convenient to model the rotor by a series of loops, rather than bars. This approach has been used in the study of cage machines with rotor-bar and end-ring faults [11], where the cage is asymmetric and explicit determination of individual bar and end-ring currents is required. In this case, the symmetry of the cage makes it possible to characterise an harmonic rotor current distribution by the currents flowing in a series of reference loops. One such loop is required for each 'band' of the machine, where a 'band' is defined as the region bounded on either side either by two adjacent inter-rings, or, at the axial ends of the machine, by an inter-ring and its adjacent end-ring. The rotor-loop model is shown in Fig.3.2. A right-handed cartesian co-ordinate system is employed, in which x is the axial distance along the core, and y is the circumferential displacement around the airgap periphery. In keeping with the generalised nature of the analysis, any number of inter-rings can be accommodated, illustrated in Fig.3.2 by assuming the i-th band to be of width a_i, and to be centred at $x=x_i$. The finite thickness of the inter-lamination insulation is taken



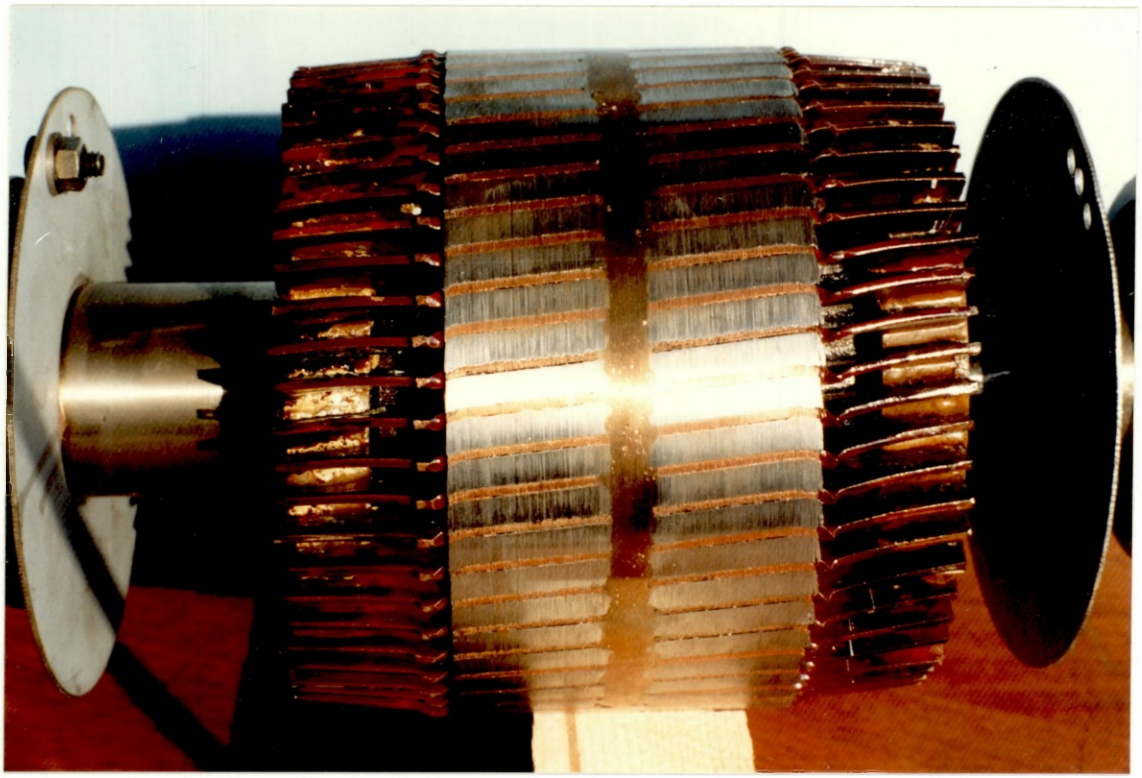


Fig.3.1: Cage rotor with inter-rings

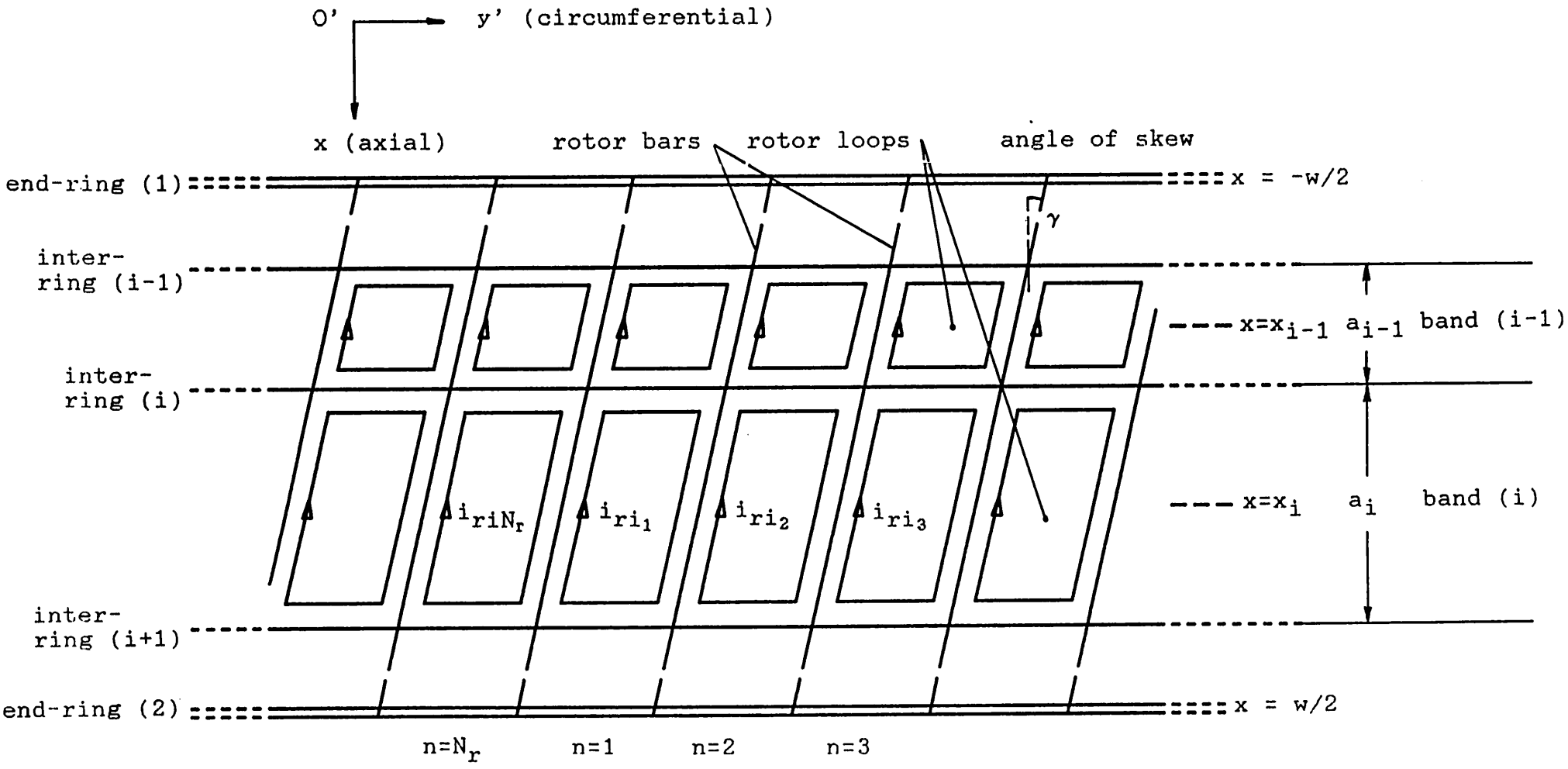


Fig.3.2: Rotor-loop model

into account in the normal way [14] by multiplying the actual core length l_c by a 'stacking factor' f_s.

A pair of concentric iron cylinders is used to model the stator and rotor airgap peripheries, with the stator windings and rotor cage both lying on smooth surfaces. The MMF produced by the current flowing in a slot is represented by an effective surface-current distribution of width equal to the slot opening. The airgap itself is assumed to be small enough for curvature effects to be negligible, and for the flux to cross the gap in straight lines. In this approach, harmonic effects due to the slotting itself are ignored, although the stator and rotor conductors are permitted to be of finite width. As far as the total flux in the machine is concerned, however, the effect of slotting is taken into account in the usual manner by employing Carter's coefficient to increase the actual airgap length [15].

Resolution of the stator windings and rotor cage into complex conductor density distributions allows the harmonic components of stator- and rotor-driven MMF to be evaluated. The iron is assumed to be infinitely permeable, enabling each harmonic component of MMF, now acting exclusively across the airgap, to be linearly related to the corresponding component of airgap flux density. The principle of superposition then remains valid throughout the calculation of the various coupling impedances. However, in a limited way it is possible to account for the non-linearity of the iron by assuming that only the principal harmonic component of flux is present in the iron parts of the magnetic circuit. The additional MMF required to produce this flux is included in the model by employing a saturation factor to increase the airgap length in the usual way [14,15].

Rotor skew is accommodated by introducing predetermined

axial variations in conductor density, and hence in rotor-driven airgap MMF. The axially-directed component of airgap flux density is neglected, an assumption justified by the laminated construction of the core [16]. Such an approach avoids the use of double harmonic series [17], since it is now unnecessary to resolve the rotor conductor density distribution in the axial (x), as well as circumferential (y) directions.

The dimensions of the inter-rings themselves remain constant, irrespective of frame size (Fig.3.3). This means that, for the smaller machines, the inter-ring extends over some 11% of the active core length of the rotor. In this region, the airgap is effectively lengthened by the presence of non-magnetic material. One method of accounting for this is to increase the gap over the entire length of the core, using a multiplicative factor equivalent to an axial Carter coefficient. This technique produces an adequate estimate of the overall flux level in the machine, but no axial variation in flux density is obtained. Such a procedure is sometimes adopted when the laminations are broken up into packets by cooling ducts [18]. In the analysis presented here, however, it is possible to specify a different airgap length for each band of the machine.

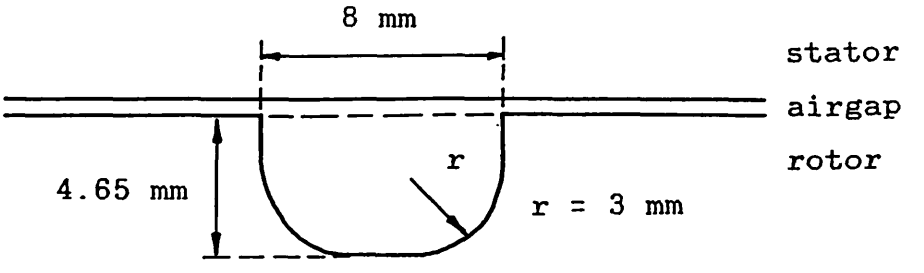


Fig.3.3: Inter-ring detail

3.2 Formulation of coupling-impedance equations

The line-frequency EMF induced in any one stator winding is determined not only by currents flowing in all N_s such windings, but also by the ensemble of harmonic currents in the rotor cage. A voltage balance equation for the m-th stator circuit may therefore be written as

$$\bar{V}_{sm} = \sum_{n=1}^{N_s} \bar{Z}_{m,n}\ \bar{I}_{sn}\ , \qquad (3.1)$$

in which $\bar{V}_{sm}$ is the RMS phasor of the m-th winding applied voltage, and $\bar{I}_{sn}$ is the n-th winding current. The objective of this and following section is to derive an expression for the 'effective stator coupling impedance' $\bar{Z}_{m,n}$ in terms of the physical details of the machine. For an N_b-band machine, the m-th winding EMF is given by

$$\bar{U}_{sm} = -\left\{ \sum_{n=1}^{N_s} \bar{Z}_{sm,sn}\ \bar{I}_{sn} + \sum_{\nu_k} \sum_{i=1}^{N_b} \bar{Z}^{k}_{sm,ri}\ \bar{I}^{k}_{ri} \right\}, \qquad (3.2)$$

where $\bar{I}^{k}_{ri}$ is the ν_k-th harmonic rotor current in the i-th rotor band reference loop. In eqn.3.2, the symbol

$$\sum_{\nu_k}$$

is used to indicate that all possible values of ν_k are included in the summation. In terms of notation :

$$\sum_{\nu_k} = \sum_{\nu_k=-\infty}^{\infty}$$

The minus sign in eqn.3.2 indicates induced EMF, balanced by

the applied terminal voltage:

$$\bar{V}_{sm} = - \bar{U}_{sm} \ . \qquad (3.3)$$

An expression similar to eqn.3.2 may be written for the ν_k-th harmonic component of EMF induced in the i-th band reference loop:

$$0 = \sum_{n=1}^{N_s} \bar{Z}^k_{ri,sn} \, \bar{I}_{sn} + \sum_{j=1}^{N_b} \bar{Z}^k_{ri,rj} \, \bar{I}^k_{rj} \ . \qquad (3.4)$$

Note that contributions are included from currents in all N_b rotor bands, as well as from those in all N_s stator windings. The applied voltage is zero, since the rotor is not connected to any external supply. In matrix notation, for all N_b bands,

$$\begin{bmatrix} 0 \\ 0 \\ \vdots \\ 0 \end{bmatrix} = \begin{bmatrix} \bar{Z}^k_{r1,s1} & \bar{Z}^k_{r1,s2} & \cdots & \bar{Z}^k_{r1,sN_s} \\ \bar{Z}^k_{r2,s1} & \bar{Z}^k_{r2,s2} & \cdots & \bar{Z}^k_{r2,sN_s} \\ \vdots & \vdots & & \vdots \\ \bar{Z}^k_{rN_b,s1} & \bar{Z}^k_{rN_b,s2} & \cdots & \bar{Z}^k_{rN_b,sN_s} \end{bmatrix} \begin{bmatrix} \bar{I}_{s1} \\ \bar{I}_{s2} \\ \vdots \\ \bar{I}_{sN_s} \end{bmatrix}$$

$$+ \begin{bmatrix} \bar{Z}^k_{r1,r1} & \bar{Z}^k_{r1,r2} & \cdots & \bar{Z}^k_{r1,rN_b} \\ \bar{Z}^k_{r2,r1} & \bar{Z}^k_{r2,r2} & \cdots & \bar{Z}^k_{r2,rN_b} \\ \vdots & \vdots & & \vdots \\ \bar{Z}^k_{rN_b,r1} & \bar{Z}^k_{rN_b,r2} & \cdots & \bar{Z}^k_{rN_b,rN_b} \end{bmatrix} \begin{bmatrix} \bar{I}^k_{r1} \\ \bar{I}^k_{r2} \\ \vdots \\ \bar{I}^k_{rN_b} \end{bmatrix} . \qquad (3.5)$$

A shorthand form of eqn.3.5 may be written as

$$[0]_{N_b} = [\bar{Z}^k_{ri,sn}]_{N_b x N_s} [\bar{I}_{sn}]_{N_s} + [\bar{Z}^k_{ri,rj}]_{N_b x N_b} [\bar{I}^k_{rj}]_{N_b},$$

where $[\bar{Z}_{i,j}]_{M x N}$ represents a matrix of M rows and N columns, the i,j-th element of which is the impedance $\bar{Z}_{i,j}$. The set of M currents, the i-th of which is $\bar{I}_i$, is similarly expressed as $[\bar{I}_i]_M$. $[0]_M$ represents a column vector composed entirely of zero elements. The system of simultaneous linear eqns.3.5 may now be rearranged to give

$$[\bar{I}^k_{rj}]_{N_b} = - [\bar{Z}^k_{ri,rj}]^{-1}_{N_b x N_b} [\bar{Z}^k_{ri,sn}]_{N_b x N_s} [\bar{I}_{sn}]_{N_s}. \quad (3.6)$$

Defining $\bar{W}^k_{ri,rj}$ to be the i,j-th element of the inverted rotor-rotor matrix $[\bar{Z}^k_{ri,rj}]_{N_b x N_b}$ enables eqn.3.6 to be re-written as

$$[\bar{I}^k_{rj}]_{N_b} = - [\bar{W}^k_{ri,rj}]_{N_b x N_b} [\bar{Z}^k_{ri,sn}]_{N_b x N_s} [\bar{I}_{sn}]_{N_s}. \quad (3.7)$$

Specifically, the ν_k-th harmonic component of the i-th band reference loop current is

$$\bar{I}^k_{ri} = - \sum_{j=1}^{N_b} \bar{W}^k_{ri,rj} \sum_{n=1}^{N_s} \bar{Z}^k_{rj,sn} \bar{I}_{sn}. \quad (3.8)$$

Substituting for $\bar{I}^k_{ri}$ from eqn.3.8, and for $\bar{U}_{sm}$ from eqn.3.2 gives

$$\bar{V}_{sm} = \sum_{n=1}^{N_s} \bar{Z}_{sm,sn} \bar{I}_{sn} - \sum_{n=1}^{N_s} \sum_{\nu_k} \sum_{i=1}^{N_b} \sum_{j=1}^{N_b} \bar{Z}^k_{sm,ri} \bar{W}^k_{ri,rj} \bar{Z}^k_{rj,sn} \bar{I}_{sn}. \quad (3.9)$$

A comparison of eqns.3.9 and 3.1 enables the effective impedance $\bar{Z}_{m,n}$ to be deduced:

$$\bar{Z}_{m,n} = \bar{Z}_{sm,sn} - \sum_{\nu_k} \sum_{i=1}^{N_b} \sum_{j=1}^{N_b} \bar{Z}_{sm,ri}\, \bar{W}_{ri,rj}\, \bar{Z}_{rj,sn} \quad (3.10)$$

Eqn.3.10 is the 'inter-ring equivalent' of the expression for $\bar{Z}_{m,n}$ derived previously [10], which, when written in the notation employed here, becomes

$$\bar{Z}_{m,n} = \bar{Z}_{sm,sn} - \sum_{\nu_k} \frac{\bar{Z}^k_{sm,r1}\ \bar{Z}^k_{r1,sn}}{\bar{Z}^k_{r1,r1}} \quad . \quad (3.11)$$

Eqn.3.10 reduces to 3.11 by recognising that, for a single-band machine, N_b=1 and $\bar{W}^k_{r1,r1} = 1/\bar{Z}^k_{r1,r1}$.

From a coupled-circuit viewpoint, eqns.3.1 and 3.10 form a complete mathematical description of the system. However, the applied winding voltages are seldom specified for a particular winding connection, and it is normally necessary to transform the set of linear equations represented by eqn.3.1 using a connection matrix [19] to take this into account. The reduced system of equations allows the given supply voltages to be used to determine a set of loop currents, from which the winding currents can be recovered using an inverse transformation. If required, the winding voltages can be calculated from eqn.3.1, and the rotor loop currents from eqn.3.8.

Explicit expressions for the various impedances in eqn. 3.10 are derived in Section 3.3.

3.3 Impedance calculations

Each impedance component introduced in the preceeding section falls into one of two categories. These are (i) stator impedances, relating EMFs induced in the stator ($\bar{Z}_{sm,sn}$) and rotor ($\bar{Z}_{ri,sn}$) to currents flowing in the stator windings, and (ii) rotor impedances, relating stator ($\bar{Z}_{sm,ri}$), and rotor ($\bar{Z}_{ri,rj}$) EMFs to currents in the rotor cage.

In either case, the basis of the method of impedance calculation is essentially the same. Firstly, current is assumed to flow either in a particular series-connected set of stator coils, or in the N_r loops that constitute a single band of the rotor cage. Complex harmonic conductor density distributions are then used to calculate the resulting infinite series of stator- or rotor-driven airgap MMF waves. Ampere's Law is applied to obtain the travelling flux density distributions, and Faraday's Law to deduce the EMFs induced in the stator windings and rotor cage.

Each category will be dealt with seperately.

3.3.1 Stator

Existing techniques for calculating the stator-stator harmonic coupling impedances [9,10,11] need to be extended to include the effects of increased gap length over short sections of the core length, as discussed in Section 3.1. In this analysis, it is assumed that the gap length is piece-wise constant, i.e.,

$$g(x)=g_i \qquad \text{for} \quad x_i-a_i/2 \leq x \leq x_i+a_i/2 \ . \tag{3.12}$$

Appendix 8.2 shows how an N-turn coil may be resolved into complex harmonic conductor density distributions. The m-th stator winding is composed of M series-connected coils, the n-th of which is situated with its coil sides in slots at $y=y_n+\alpha_n/2$ and $y=y_n-\alpha_n/2$. The overall distribution of the m-th winding is obtained by summing the contribution from each coil:

$$c_{sm}(y) = \sum_{\nu_k} \bar{C}^k_{sm}\ e^{-jky} \quad , \tag{3.13}$$

where

$$\bar{C}^k_{sm} = \frac{-2j}{\pi d}\ K^k_{bs} \sum_{n=1}^{M_m} N_n\ \sin(k\alpha_n/2)\ e^{jky_n} \quad . \tag{3.14}$$

The harmonic series of rotating MMF produced by the current

$$i_{sm}(t) = \mathrm{Re}\left\{\sqrt{2}\ \bar{I}_{sm}\ e^{j\omega t}\right\} \tag{3.15}$$

flowing in the m-th winding is

$$\begin{aligned} j_{sm}(y,t) &= c_{sm}(y)\ i_{sm}(t) \\ &= \left\{\sum_{\nu_k} \bar{C}^k_{sm}\ e^{-jky}\right\} \mathrm{Re}\left\{\sqrt{2}\ \bar{I}_{sm}\ e^{j\omega t}\right\} \quad . \end{aligned} \tag{3.16}$$

Since $c_{sm}(y)$ is wholly real, eqn.3.16 can be rewritten as

$$j_{sm}(y,t) = \mathrm{Re}\left\{\sum_{\nu_k} \sqrt{2}\ \bar{J}^k_{sm}\ e^{\ j(\omega t-ky)}\right\}, \tag{3.17}$$

where

$$\bar{J}^k_{sm} = \bar{C}^k_{sm}\ \bar{I}_{sm} \quad . \tag{3.18}$$

The stator-driven airgap flux density wave is obtained by applying Ampere's Law around the elemental loop shown in Fig.3.4.

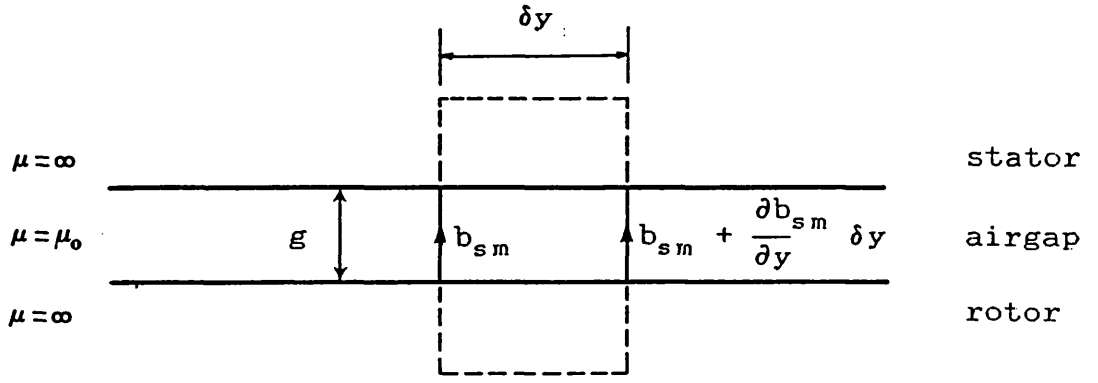


Fig.3.4 Elemental loop for application of Ampere's Law

Flux is assumed to cross the airgap in straight lines, giving, in the i-th band of the machine,

$$\frac{\partial b_{sm}}{\partial y}(x,y,t) = \frac{\mu_0}{g_i}\, j_{sm}(y,t) \quad \text{for} \quad x_i - a_i/2 \le x \le x_i + a_i/2 \tag{3.19}$$

The variation in gap length introduces a step change in airgap flux density at the junction of adjacent bands. In reality, fringing occurs around the slot forming the inter-ring, resulting in a smoother transition from one band to the next. A method of accounting for this phenomenon is discussed in Section 5.2.3.

The airgap flux density has the general form

$$b_{sm}(x,y,t) = \mathrm{Re}\left\{ \sum_{\nu_k} \sqrt{2}\, \bar{B}^k_{sm}(x)\, e^{j(\omega t - ky)} \right\}, \tag{3.20}$$

where

$$\bar{B}^k_{sm}(x) = \frac{j\mu_0}{k g_i}\, \bar{J}^k_{sm} \,. \tag{3.21}$$

Faraday's Law is used to calculate the electric field strength at the airgap surface of the stator, giving

$$\frac{\partial e_{sm}}{\partial y}(x,y,t) = \frac{\partial b_{sm}}{\partial t}(x,y,t) \ , \qquad (3.22)$$

and

$$e_{sm}(x,y,t) = \mathrm{Re}\left\{ \sum_{\nu_k} \sqrt{2}\ \bar{E}^{k}_{sm}(x)\ e^{j(\omega t - ky)} \right\} \ , \qquad (3.23)$$

where

$$\bar{E}^{k}_{sm}(x) = -\ \omega/k\ \bar{B}^{k}_{sm}(x) \ . \qquad (3.24)$$

The EMF induced in another stator winding (the n-th) is given by the line integral of the electric field strength around the appropriate circuit. In this case, the n-th winding is represented by the conductor density $c_{sn}(y)$, and so

$$u_{sn,sm}(t) = \int_{x=-w/2}^{w/2} \int_{y=-\pi d/2}^{\pi d/2} e_{sm}(y,t)\ c_{sn}(y)\ dx\ dy \ . \qquad (3.25)$$

Substituting from eqns.3.13 and 3.23 :

$$u_{sn,nm}(t) = \int_{x=-w/2}^{w/2} \int_{y=-\pi d/2}^{\pi d/2} \mathrm{Re}\left\{ \sum_{\nu_k} \sum_{\nu_l} \sqrt{2}\ \bar{E}^{k}_{sm}\ \bar{C}^{l}_{sn}\ e^{j\omega t}\ e^{-j(k+l)y} \right\} dx\ dy \qquad (3.26)$$

where

$$l = 2\nu_l/d \quad \text{and} \quad k+l = 2(\nu_k+\nu_l)/d \ . \qquad (3.27)$$

Now the integral term

$$\int_{-\pi d/2}^{\pi d/2} \exp\{-j(k+1)y\}\, dy$$

is zero for $k+1 \neq 0$, and πd for $k+1=0$, giving

$$u_{sn,sm}(t) = \int_{-w/2}^{w/2} \mathrm{Re}\left\{ \sum_{\nu_k} \sqrt{2}\pi d\ \bar{E}^k_{sm}(x)\ \bar{C}^{k*}_{sn}\ e^{\ j\omega t} \right\} dx \ . \tag{3.28}$$

Within any one band, the electric field strength does not vary in the x direction, allowing the integration to be performed by a summation. Substituting from eqns.3.24, 3.18, 3.21 and 3.12,

$$u_{sn,sm}(t) = -\ \mathrm{Re}\left\{ \sum_{\nu_k} \frac{j\omega\mu_0\pi d}{k^2}\ \ \bar{C}^k_{sm}\ \bar{C}^{k*}_{sn} \sum_{i=1}^{N_b} a_i/g_i\ \ \bar{I}_{sm}\ e^{j\omega t} \right\} \tag{3.29}$$

The induced EMF is of the standard form :

$$u_{sn,sm}(t) = \mathrm{Re}\left\{ \sqrt{2}\ \bar{U}_{sn,sm}\ e^{j\omega t} \right\} , \tag{3.30}$$

where

$$\begin{aligned} \bar{U}_{sn,sm} &= -j\omega\mu_0\pi d \sum_{i=1}^{N_b} a_i/g_i\ \ \bar{I}_{sm} \sum_{\nu_k} \frac{\bar{C}^k_{sm}\ \bar{C}^{k*}_{sn}}{k^2} \\ &= -\ \bar{Z}_{sn,sm}\ \bar{I}_{sm} \ , \end{aligned} \tag{3.31}$$

giving the stator-stator coupling impedance :

$$\bar{Z}_{sn,sm} = j\omega\mu_0\pi d \sum_{i=1}^{N_b} a_i/g_i \sum_{\nu_k} \frac{\bar{C}^k_{sm}\ \bar{C}^{k*}_{sn}}{k^2} \ , \tag{3.32}$$

For a machine with a constant airgap length g, note that

$$\sum_{i=1}^{N_b} a_i / g_i = w/g \ .$$

With this simplification, eqn.3.32 reduces to the expression obtained by Williamson [9].

The above derivation has been carried out by considering flux conditions in the airgap alone, although stator slot and end-winding leakage fields are additional sources of magnetic coupling between windings. The effects of both non-airgap fluxes and winding resistances are taken into account by adding an extra 'leakage' impedance term to the right hand side of eqn.3.32, giving

$$\bar{Z}_{sn,sm} = j\omega\mu_0 \pi d \sum_{i=1}^{N_b} a_i / g_i \sum_{\nu_k} \frac{\bar{C}^k_{sm} \bar{C}^{k*}_{sn}}{k^2} + \bar{Z}^L_{sn,sm} \ , \qquad (3.33)$$

where

$$\left.\begin{aligned} \bar{Z}^L_{sn,sm} &= j\{ X^{slot}_{sn,sm} + X^{end}_{sn,sm}\} \quad \text{for } m \neq n \\ \text{and} \qquad & \\ \bar{Z}^L_{sn,sn} &= j\{ X^{slot}_{sn,sn} + X^{end}_{sn,sm}\} + R_{sn} \ . \end{aligned}\right\} \qquad (3.34)$$

$X^{slot}_{sn,sm}$ the coupling impedance between the n-th and m-th stator windings due to slot leakage flux, is calculated on a slot-by-slot basis using standard formulae [15]. The coupling impedance due to end-winding leakage flux, $X^{end}_{sn,sm}$, is more difficult to evaluate. For the purposes of this analysis, the values estimated by Bull Electric in their equivalent-circuit approach are used. R_{sn} is the resistance of the n-th stator winding, obtained by summing contributions from each coil.

Each harmonic component of airgap flux produced by current flowing in the m-th stator winding also induces EMFs of a particular frequency in the rotor cage. The rotor-stator coupling impedance is calculated by considering the EMF induced in the i-th band rotor reference loop by the ν_k-th harmonic component of flux density. The procedure is similar to that described above. In this case, however, the harmonic rotor conductor density distributions, derived in Appendix 8.2, are expressed in terms of rotor, rather than stator co-ordinates. The relationship between the two co-ordinate frames is determined by the speed of the rotor relative to the stator. Writing the actual rotor angular velocity as ω_r, and the synchronous speed of the ν_k-th harmonic field as ω_{sk}, the ν_k-th harmonic slip is defined by

$$s_k = (\omega_{sk} - \omega_r)/\omega_{sk} \quad . \tag{3.35}$$

The synchronous speed of a $2\nu_k$-pole field is ω/ν_k, and the linear velocity of the rotor is therefore

$$\begin{aligned} v &= \omega_r d/2 = (1-s_k)\,\omega_{sk} d/2 \\ &= (1-s_k)\,\omega/k \quad . \end{aligned} \tag{3.36}$$

Assuming that the axes of the rotor and stator reference frames coincide at t=0, Fig.3.5 shows that

$$y = y' + vt \ ,$$

i.e.,

$$y = y' + (1-s_k)\,\omega t/k \ , \tag{3.37}$$

on substitution from eqn.3.36. The x co-ordinate is the same in both reference frames.

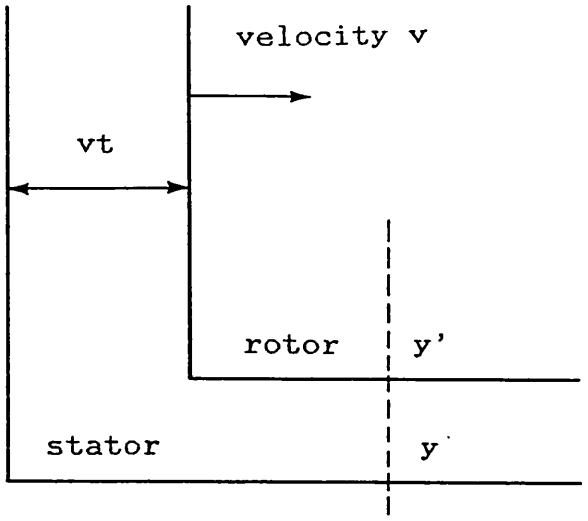


Fig.3.5: Stator and rotor co-ordinate frames

The v_k-th harmonic component of airgap flux density produced by the m-th stator winding current may be separated from eqn.3.20 :

$$b^k_{sm}(x,y,t) = Re\left\{\sqrt{2}\ \bar{B}^k_{sm}(x)\ e^{j(\omega t - ky)}\right\}. \qquad (3.38)$$

In terms of rotor co-ordinates, eqn.3.38 becomes

$$b^k_{sm}(x,y',t) = Re\left\{\sqrt{2}\ \bar{B}^k_{sm}(x)\ e^{j(s_k\omega t - ky')}\right\}. \qquad (3.39)$$

The electric field strength at any point on the rotor is therefore

$$e^k_{sm}(x,y',t) = Re\left\{\sqrt{2}\ \bar{E}^k_{sm}(x)\ e^{j(s_k\omega t - ky')}\right\}, \qquad (3.40)$$

where

$$\bar{E}^k_{sm}(x) = -\frac{s_k\omega}{k}\ \bar{B}^k_{sm}(x)\ . \qquad (3.41)$$

The EMF induced in a particular rotor loop in the i-th band of the machine is obtained by integrating the product of electric field strength and conductor density distribution over the airgap surface of that band. Appendix 8.2 shows that the complex conductor density distribution of the n-th rotor loop is dependent on axial position, as a consequence of rotor skew. It is given by

$$c_{rn}(x,y') = \sum_{v_k} \bar{C}^k_{rn} \; e^{-jk(y' + x\tan\gamma)} \quad . \tag{3.42}$$

The circumferential position of the centre of the n-th loop at the middle of the machine is

$$y'_0 = \lambda_r/2 + (n-1)\lambda_r \quad .$$

Substituting into eqn.8.10, it is possible to write

$$\bar{C}^k_{rn} = \bar{A}^k_r \; e^{j(n-1)\lambda_r} , \tag{3.43}$$

where

$$\bar{A}^k_r = - \frac{2j}{\pi d} K^k_{br} \sin\left(\frac{k\lambda_r}{2}\right) \exp\left(\frac{jk\lambda_r}{2}\right) \quad . \tag{3.44}$$

The induced EMF is therefore

$$u^k_{rin,sm}(t) = \int_{x=x_i-a_i/2}^{x_i+a_i/2} \int_{y=-\pi d/2}^{\pi d/2} e^k_{sm}(x,y',t) \; c_{rn}(x,y') \; dx \; dy' \tag{3.45}$$

Substituting from eqns.3.40 and 3.42:

$$u^k_{rin,sm}(t) = \iint \mathrm{Re}\left\{ \sum_{v_l} \sqrt{2} \; \bar{E}^k_{sm}(x) \; \bar{C}^l_{rn} \; e^{js_k\omega t} \; e^{-j(k+l)y'} \; e^{-j\,lx\tan\gamma} \right\} dx \; dy' \quad . \tag{3.46}$$

As before, the integral with respect to y' vanishes unless l=-k, in which case

$$u^k_{rin,sm}(t) = \int_{x=x_i-a_i/2}^{x_i+a_i/2} Re\left\{\sqrt{2}\ \bar{E}^k_{sm}(x)\ \bar{C}^{k*}_{rn}\ \pi d\ e^{js_k\omega t}\right.$$

$$\left. e^{jkx\tan\gamma}\right\} dx \ . \qquad (3.47)$$

Performing the integration with respect to x, and substituting from eqns.3.21, 3.18 and 3.41:

$$u^k_{rin,sm}(t) = - Re\left\{\sqrt{2}\ \frac{j\omega\mu_0 a_i \pi d}{k^2\ g_i}\ s_k\ K^k_i\ \bar{C}^k_{sm}\ \bar{C}^{k*}_{rn}\right.$$

$$\left. e^{jkx_i\tan\gamma}\ \bar{I}_{sm}\ e^{js_k\omega t}\right\}, \qquad (3.48)$$

in which the v_k-th harmonic skew factor for the i-th band is defined as

$$K^k_i = \frac{\sin\{\frac{ka_i}{2}\tan\gamma\}}{\frac{ka_i}{2}\tan\gamma} \ . \qquad (3.51)$$

Eqn.3.50 may be written in the standard form

$$u^k_{rin,sm}(t) = Re\left\{\sqrt{2}\ \bar{U}^k_{rin,sm}\ e^{js_k\omega t}\right\}, \qquad (3.52)$$

where

$$\bar{U}^k_{rin,sm} = - \bar{Z}^k_{rin,sm}\ \bar{I}_{sm} \ , \qquad (3.53)$$

giving the rotor-stator coupling impedance

$$\bar{Z}^k_{rin,sm} = \frac{j\omega\mu_0 a_i \pi d s_k}{k^2 g_i}\ K^k_i\ \bar{C}^k_{sm}\ \bar{C}^{k*}_{rn}\ e^{jkx_i\tan\gamma} \ . \qquad (3.54)$$

Substituting from eqn.3.43 :

$$\bar{Z}^k_{rin,sm} = \frac{j\omega\mu_0 a_i \pi ds_k}{k^2 g_i} K^k_i \bar{C}^k_{sm} \bar{A}^{k*}_r e^{jkx_i \tan\gamma} e^{-jk(n-1)\lambda_r} . \quad (3.55)$$

Eqn.3.55 shows that, in a particular band of the machine, the rotating flux waves produced by the m-th stator winding current induce EMFs in the rotor loops which are equal in magnitude, but differ in phase due to the term $\exp\{-jk(n-1)\lambda_r\}$. As anticipated in Section 3.1, it is possible to model the rotor by considering the EMFs induced in a series of reference loops. The phase term $\exp\{jkx_i \tan\gamma\}$ in eqn.3.55 shows that one such loop is required for each band of the machine. As the circumferential position of these loops is completely arbitrary, it is convenient to situate them such that n=1. With this simplification, the subscript n in the impedance notation may be omitted, giving

$$\bar{Z}^k_{ri,sm} = \frac{j\omega\mu_0 a_i \pi ds_k}{k^2 g_i} K^k_i \bar{C}^k_{sm} \bar{A}^{k*}_r e^{jkx_i \tan\gamma} . \quad (3.56)$$

3.3.2 Rotor coupling impedances

Each harmonic component of EMF described by eqn.3.52 causes current of angular frequency $s_k\omega$ to flow in the n-th rotor loop in the i-th band of the machine. The symmetry of the cage means that the N_r loop currents set up in this way are of equal magnitude with a phase progression of $k\lambda_r$. Defining the ν_k-th harmonic i-th band reference loop current to be

$$i^k_{ri}(t) = \mathrm{Re}\left\{ \sqrt{2}\, \bar{I}^k_{ri}\, e^{js_k\omega t} \right\}, \quad (3.57)$$

gives the corresponding n-th loop current :

$$i^k_{rin}(t) = \mathrm{Re}\left\{ \sqrt{2}\, \bar{I}^k_{ri}\, e^{js_k\omega t}\, e^{-jk(n-1)\lambda_r} \right\} . \quad (3.58)$$

Each such current distribution establishes an infinite series of rotating MMF waves, given by the product of the loop current (eqn.3.58) and the conductor density distribution (eqn.3.43) :

$$j^k_{rin}(x,y',t) = c_{rn}(x,y')\; i^k_{rin}(t)$$

$$= \mathrm{Re}\left\{ \sum_{\upsilon_l} \sqrt{2}\; \bar{C}^l_{rn}\; e^{-jl(y'+x\tan\gamma)}\; e^{js_k\omega t}\, \bar{I}^k_{ri} \right.$$

$$\left. e^{jk(n-1)\lambda_r} \right\} \quad . \qquad (3.59)$$

Substituting from eqn.3.43 and simplifying,

$$j^k_{rin}(x,y',t) = \mathrm{Re}\left\{ \sum_{\upsilon_l} \sqrt{2}\; \bar{A}^l_r\; \bar{I}^k_{ri}\; e^{js_k\omega t}\; e^{-jl(y'+x\tan\gamma)} \right.$$

$$\left. e^{j(n-1)\lambda_r(1-k)} \right\} \quad . \qquad (3.60)$$

The total rotor-driven wave is the sum of the contributions from all N_r current-carrying loops in the i-th band :

$$j^k_{ri}\;(x,y',t) = \sum_{n=1}^{N_r} j^k_{rin}(x,y',t) \qquad (3.61)$$

$$= \mathrm{Re}\left\{ \sum_{\upsilon_l} \sqrt{2}\; \bar{A}^l_r\; \bar{I}^k_{ri}\; e^{js_k\omega t}\; e^{-jl(y'+x\tan\gamma)} \right.$$

$$\left. \sum_{n=1}^{N_r} e^{j(n-1)\lambda_r(1-k)} \right\} \quad . \qquad (3.62)$$

The sum to N terms of a geometric progression defined by the general term $u_r = x^{r-1}$ is $S_N = (1-x^N)/(1-x)$. The second summation in eqn.3.62 therefore becomes

$$\left.\begin{aligned} \sum_{n=1}^{N_r} e^{j(n-1)\lambda_r(1-k)} &= 0 \quad \text{for} \quad v_l - v_k \neq v_q N_r \\ &= N_r \quad \text{for} \quad v_l - v_k = v_q N_r \end{aligned}\right\}, \qquad (3.62)$$

where v_q is any integer. Defining the wavenumber q as

$$q = \frac{2 v_q N_r}{d} , \qquad (3.63)$$

gives

$$v_l - v_k = (1-k)\, d/2 = v_q N_r = dq/2 , \qquad (3.64)$$

implying that

$$l = k + q . \qquad (3.65)$$

For all possible integer values of v_q, eqn.3.61 becomes

$$j_{ri}^{k}(x,y',t) = \mathrm{Re}\left\{ \sum_{v_q} \sqrt{2}\, \bar{A}_r^{k+q}\, \bar{I}_{ri}^{k}\, e^{j s_k \omega t}\, e^{-j(k+q)(y'+x\tan\gamma)} \right\} . \qquad (3.66)$$

It can be seen from eqn.3.66 that rotor-slot harmonics on the $2v_k$ -pole wave are produced when $q \neq 0$. These harmonic fields induce non-supply frequency EMFs in the stator windings, which can, under certain circumstances, result in additional stator current distributions of other than mains frequency. This effect is known as 'secondary armature reaction', and is at its strongest in delta-connected windings with several parallel paths [20]. An increase in the number and magnitude of parasitic torques can sometimes result, a problem aggravated by unsuitable choices of rotor/stator slot combinations. As far as this analysis is concerned, the effect of rotor-slot harmonics on the stator is assumed to be small enough to be neglected.

Substituting q=0 into eqn.3.66,

$$j^k_{ri}(x,y',t) = \mathrm{Re}\left\{ \sqrt{2}\ \bar{J}^k_{ri}\ e^{js_k\omega t}\ e^{-jk(y'+x\tan\gamma)} \right\} , \tag{3.67}$$

where

$$\bar{J}^k_{ri} = \bar{I}^k_{ri}\ \bar{A}^k_r\ N_r \ . \tag{3.68}$$

In the stator reference frame, eqn.3.67 becomes

$$j^k_{ri}(x,y,t) = \mathrm{Re}\left\{ \sqrt{2}\ \bar{J}^k_{ri}\ e^{j\omega t}\ e^{-jk(y+x\tan\gamma)} \right\} \ . \tag{3.69}$$

The corresponding flux density is therefore

$$b^k_{ri}(x,y,t) = \mathrm{Re}\left\{ \sqrt{2}\ \bar{B}^k_{ri}\ e^{j\omega t}\ e^{-jk(y+x\tan\gamma)} \right\} , \tag{3.70}$$

where

$$\bar{B}^k_{ri} = \frac{j\mu_0}{kg_i}\ \bar{J}^k_{ri} \ . \tag{3.71}$$

Assuming that the axially-directed component of airgap flux is negligible, as discussed in Section 3.1, the flux density wave described by eqn.3.71 induces EMFs only in those parts of the n-th stator windings which occupy the i-th band of the machine. The electric field strength at any point in the i-th band is therefore

$$e^k_{ri}(x,y,t) = \mathrm{Re}\left\{ \sqrt{2}\ \bar{E}^k_{ri}\ e^{j\omega t}\ e^{-jk(y+x\tan\gamma)} \right\} , \tag{3.72}$$

in which

$$E^{-k}_{ri} = -\frac{\omega}{k}\ B^{-k}_{ri} \ . \tag{3.73}$$

The EMF induced in the i-th band of the n-th winding is

$$u^k_{sn,ri}(t) = \int_{x=x_i-a_i/2}^{x_i+a_i/2} \int_{y=-\pi d/2}^{\pi d/2} e^k_{ri}(x,y,t)\, c_{sn}(y)\, dx\, dy \,. \tag{3.74}$$

Substituting from eqns.3.13 and 3.73,

$$u^k_{sn,ri}(t) = \sum_{\nu_l} \iint \mathrm{Re}\left\{ \sqrt{2}\, \bar{E}^k_{ri}\, \bar{C}^l_{sn}\, e^{-jkx\tan\gamma}\, e^{j(k+l)y} \right\} dx\, dy \,. \tag{3.75}$$

As usual, the integral with respect to y is zero unless l=-k, in which case

$$u^k_{sn,ri}(t) = \mathrm{Re}\left\{ \sqrt{2} a_i \pi d\, \bar{E}^k_{ri}\, \bar{C}^{k*}_{sn}\, K^k_i\, e^{-jkx_i\tan\gamma}\, e^{j\omega t} \right\}, \tag{3.76}$$

where K^k_i is defined by eqn.3.51. Eqn.3.76 may be rewritten as

$$u^k_{sn,ri}(t) = \mathrm{Re}\left\{ \sqrt{2}\, \bar{U}^k_{sn,ri}\, e^{j\omega t} \right\}, \tag{3.77}$$

where

$$\bar{U}^k_{sn,ri} = -\, \bar{Z}^k_{sn,ri}\, \bar{I}^k_{ri} \,. \tag{3.78}$$

Substitution from eqns.3.68, 3.71 and 3.73 gives the ν_k-th harmonic stator-rotor coupling impedance :

$$\bar{Z}^k_{sn,ri} = \frac{j\omega\mu_0 a_i \pi d}{k^2 g_i}\, N_r\, K^k_i\, \bar{A}^k_r\, \bar{C}^{k*}_{sn}\, e^{-jkx_i\tan\gamma} \,. \tag{3.79}$$

Although the effect of rotor-slot harmonics on the stator was ignored in the derivation of eqn.3.79, their effect on the rotor is incorporated by including all possible values of ν_q in eqn.3.66 in the calculation of the rotor-rotor coupling impedances. As a result, the slot-harmonic fields produced by the ν_k-th harmonic rotor current distribution link only the rotor cage, and not the stator

windings. They can therefore be regarded as contributing to the rotor leakage flux, being accounted for as the rotor differential leakage for the v_k-th harmonic. It is a feature of this and previous analyses [17,21] that such leakage is included implicitly, and does not have to be added in as a separate component.

The flux density waves associated with the MMF distributions of eqn.3.66 may be written as

$$b^k_{ri}(x,y',t) = \mathrm{Re}\left\{\sum_{v_q} \sqrt{2}\ \bar{B}^{k+q}_{ri}\ e^{js_k\omega t}\ e^{-j(k+q)(y'+x\tan\gamma)}\right\}, \qquad (3.80)$$

where

$$\bar{B}^{k+q}_{ri} = \frac{j\mu_0}{(k+q)g_i}\ \bar{I}^k_{ri}\ \bar{A}^{k+q}_r\ N_r\ . \qquad (3.81)$$

The corresponding electric field strength is

$$e^k_{ri}(x,y',t) = \mathrm{Re}\left\{\sum_{v_q} \sqrt{2}\ \bar{E}^{k+q}_{ri}\ e^{js_k\omega t}\ e^{-j(k+q)(y'+x\tan\gamma)}\right\}, \qquad (3.82)$$

where

$$\bar{E}^{k+q}_{ri} = -\frac{\omega s_k}{k+q}\ \bar{B}^{k+q}_{ri}\ . \qquad (3.83)$$

Again, assuming that the axial component of airgap flux is zero, the EMF induced in the n-th rotor loop is

$$u^k_{rin,ri}(t) = \int_{x=x_i-a_i/2}^{x_i+a_i/2} \int_{y=-\pi d/2}^{\pi d/2} e^k_{ri}(x,y',t)\ c_{rn}(x,y')\ dx\ dy'\ . \qquad (3.84)$$

Substituting from eqns.3.43 and 3.82 and performing the integrations :

$$u^k_{rin}(t) = \mathrm{Re}\left\{ \sum_{v_q} \sqrt{2}\, a_i \pi d\, \bar{E}^{k+q}_{ri}\, \bar{A}_r^{-k-q}\, e^{js_k\omega t} \right.$$

$$\left. e^{-j(k+q)(n-1)\lambda_r} \right\} . \qquad (3.85)$$

For the reference loop, n=1 and eqn.3.85 can be expressed as

$$u^k_{ri,ri}(t) = \mathrm{Re}\left\{ \sqrt{2}\, \bar{U}^k_{ri,ri}\, e^{js_k\omega t} \right\} , \qquad (3.86)$$

where

$$\bar{U}^k_{ri,ri} = - \bar{Z}^k_{ri,ri}\, \bar{I}^k_{ri} . \qquad (3.87)$$

On substitution from eqns.3.81, 3.83 and 3.85, the rotor-rotor coupling impedance may be written as

$$\bar{Z}^k_{ri,ri} = \frac{j\omega\mu_0 a_i \pi d}{g_i}\, s_k\, N_r \sum_{v_q} \frac{|\bar{A}^{k+q}_r|^2}{(k+q)^2} . \qquad (3.88)$$

It can be shown [21], from the theory of residuals [22], that the series in eqn.3.88, after substitution from eqn.3.44 and 8.7, sums to

$$\sum_{v_q} \frac{|\bar{A}^{k+q}|^2}{(k+q)^2} = \frac{1}{N_r^2} - \frac{2b_r}{3\pi d N_r} \sin^2\left(\frac{k\lambda_r}{2}\right) . \qquad (3.89)$$

Substitution into eqn.3.88 gives, finally,

$$\bar{Z}^k_{ri,ri} = \frac{j\omega\mu_0 a_i \pi d}{N_r g_i}\, s_k \left[1 - \frac{2N_r b_r}{3\pi d} \sin^2\left(\frac{k\lambda_r}{2}\right) \right] . \qquad (3.90)$$

As in the calculation of the stator-stator impedances, extra 'leakage impedance' terms must be added to the expression obtained above, since it was derived solely from airgap-flux considerations. In any one band, adjacent rotor loops are also coupled by virtue of non-zero bar resistances and slot-leakage fields. Similar effects produced by the inter-rings result in coupling between equally-numbered loops in adjacent bands.

These leakage components may be determined with reference to Fig.3.6, in which the ν_k-th harmonic loop currents are defined by eqn.3.58. $\bar{Z}^k_{er}$ represents the resistance and leakage reactance of the segment of end-ring which links adjacent bars :

$$\bar{Z}^k_{er} = (R_{er} + js_k X_{er})/N_r \ . \qquad (3.91)$$

R_{er} is the resistance of an end-ring, as presented to a circulating current. The leakage reactance X_{er} is difficult to calculate accurately, and in this analysis is neglected entirely. The inter-ring impedances are given by

$$\bar{Z}^k_{ai} = (R_{ai} + js_k X_{ai})/N_r \ , \qquad (3.92)$$

for i=1 to N_b-1. R_{ai} is the resistance of the i-th inter-ring and X_{ai} the leakage reactance. The impedance of the length of bar which occupies the i-th band similarly consists of resistance and slot-leakage reactance :

$$\bar{Z}^k_{bi} = R^k_{bi} + js_k X^k_{bi} \ . \qquad (3.93)$$

the subscript k is included throughout eqn.3.93, since, in general, the bar resistance and reactance are functions of frequency, because of skin effect. A simple multiplicative

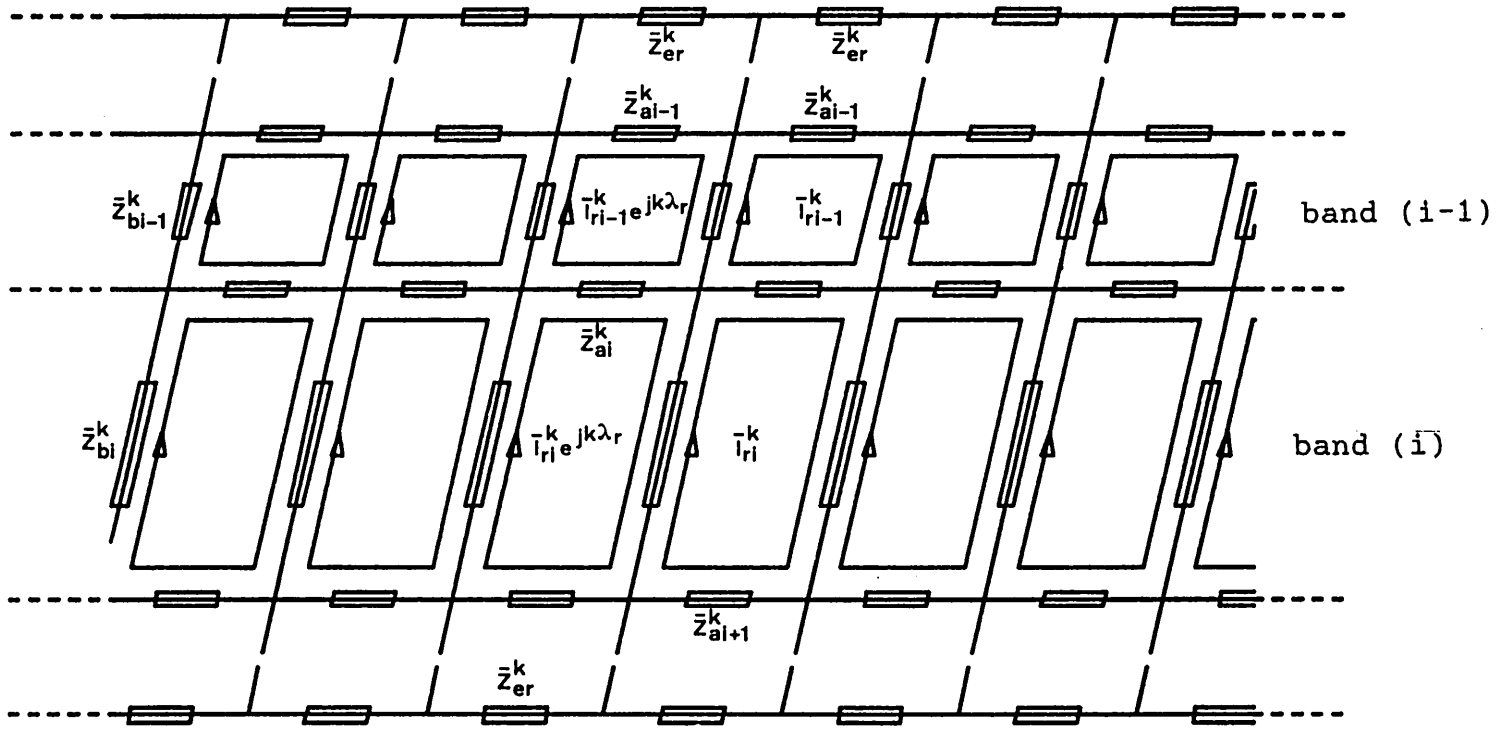


Fig.3.6: Rotor-loop model : leakage impedance calculation

factor is employed to take this into account [13]. The rotor bars extend beyond the ends of the core, where the current is assumed to be more uniformly distributed and no correction factor is thought necessary. This means that the total bar impedance cannot simply be scaled to obtain $\bar{Z}^k_{bi}$; the position of the i-th band must also be considered.

Kirchoff's voltage law may be applied around the i-th band reference loop to give

$$0 = \bar{Z}^k_{bi} \, (\bar{I}^k_{ri} - \bar{I}^k_{ri} e^{jk\lambda_r}) + \bar{Z}^k_{ai-1} \, (\bar{I}^k_{ri} - \bar{I}^k_{ri-1}) + \bar{Z}^k_{bi} \, (\bar{I}^k_{ri} - \bar{I}^k_{ri} e^{-jk\lambda_r}) + \bar{Z}^k_{ai+1} \, (\bar{I}^k_{ri} - \bar{I}^k_{ri+1}) \, . \tag{3.94}$$

Writing eqn.3.94 as

$$0 = \bar{Z}^{kL}_{ri,ri} \, \bar{I}^k_{ri} + \bar{Z}^{kL}_{ri,ri-1} \, \bar{I}^k_{ri-1} + \bar{Z}^{kL}_{ri,ri+1} \, \bar{I}^k_{ri+1} \, , \tag{3.95}$$

gives the 'self-leakage impedance' :

$$\bar{Z}^{kL}_{ri,ri} = 4 \, \bar{Z}^k_{bi} \, \sin^2(k\lambda_r/2) + \bar{Z}^k_{ai-1} + \bar{Z}^k_{ai+1} \, . \tag{3.96}$$

Eqn.3.96 is valid only when the i-th band is bordered on both sides by inter-rings ($1 < i < N_b$). At the ends of the machine :

$$\bar{Z}^{kL}_{r1,r1} = 4 \, \bar{Z}^k_{b1} \, \sin^2(k\lambda_r/2) + \bar{Z}^k_{er} + \bar{Z}^k_{a1} \, . \tag{3.97}$$

$$\bar{Z}^{kL}_{rN_b,rN_b} = 4 \, \bar{Z}^k_{b1} \, \sin^2(k\lambda_r/2) + \bar{Z}^k_{er} + \bar{Z}^k_{aN_b-1} \, . \tag{3.97}$$

Coupling between adjacent bands is provided by the mutual impedance terms in eqn.3.95 :

$$\left.\begin{aligned} \bar{Z}^{kL}_{ri,ri-1} &= -\bar{Z}^{k}_{ai-1} \qquad \text{for} \quad i = 2 \text{ to } N_b \\ \bar{Z}^{kL}_{ri,ri+1} &= -\bar{Z}^{k}_{ai} \qquad \text{for} \quad i = 1 \text{ to } N_b - 1 \end{aligned}\right\} . \quad (3.98)$$

The addition of these leakage components to the airgap impedance of eqn.3.90 gives the total v_k-th harmonic rotor-rotor coupling impedance :

$$\left.\begin{aligned} \bar{Z}^{k}_{ri,rj} &= 0 \qquad\qquad\qquad\qquad \text{for } j < i-1 \text{ or } j > i+1 \\ \bar{Z}^{k}_{ri,rj} &= \bar{Z}^{k}_{rj,ri} = \bar{Z}^{kL}_{ri,rj} \qquad \text{for } j = i-1 \text{ or } j = i+1 \\ \bar{Z}^{k}_{ri,ri} &= \frac{j\omega\mu_0 a_i \pi d}{N_r g_i} s_k \left[1 - \frac{2N_r b_r}{3\pi d} \sin^2\left(\frac{k\lambda_r}{2}\right)\right] + \bar{Z}^{kL}_{ri,ri} \end{aligned}\right\} . \quad (3.99)$$

Each impedance term in eqn.3.10 is expressed by one of eqns.3.34, 3.56, 3.79 or 3.99, recalling that the admittance $\bar{W}^{k}_{ri,rj}$ is the i,j-th element of the inverted v_k-th harmonic rotor-rotor impedance matrix. At this stage it is encouraging to note that in the absence of inter-rings, N_b=1 and the expression for the effective stator coupling impedance reduces to that derived previously [10].

3.4 Steady-State Performance

Enough theory has so far been presented to permit the winding and cage currents to be determined for a given terminal excitation. In this section, expressions are derived for the additional quantities (input power, losses, torque, etc.) normally used to describe the steady-state performance of an induction machine.

The total complex power consumed at the terminals is given by

$$\bar{S}_{in} = \sum_{n=1}^{N_s} \bar{V}_{sn} \bar{I}^*_{sn}$$

$$= P_{in} + jQ_{in} \ . \qquad (3.100)$$

The overall power factor is therefore

$$\lambda = \sqrt{\left(\frac{\{P_{in}\}^2}{\{P_{in}\}^2 + \{Q_{in}\}^2} \right)} \ . \qquad (3.101)$$

As discussed in Section 2.1, the ν_k-th harmonic airgap power factor is also of interest, and may be obtained from eqn.3.100 by substituting for $\bar{V}_{sm}$ from eqn.3.1 to give

$$\bar{S}_{in} = \sum_{m=1}^{N_s} \sum_{n=1}^{N_s} \bar{Z}_{m,n} \bar{I}_{sn} \bar{I}^*_{sm} \ . \qquad (3.102)$$

From eqn.3.11, the overall impedance $\bar{Z}_{m,n}$ may be written as

$$\bar{Z}_{m,n} = \bar{Z}^L_{sm,sn} + \bar{Z}^A_{sm,sn} \ , \qquad (3.103)$$

where $\bar{Z}^{L}_{sm,sn}$ is defined by eqns.3.34. The 'airgap' impedance is

$$\bar{Z}^{A}_{sm,sn} = \sum_{\upsilon_k} \bar{Z}^{kA}_{sm,sn} \ , \tag{3.104}$$

where, on substitution from eqn.3.33,

$$\bar{Z}^{kA}_{sm,sn} = j\omega\mu_0 \sum_{i=1}^{N_b} \frac{a_i}{g_i} \frac{\bar{C}^{k}_{sm}\ \bar{C}^{k*}_{sn}}{k^2} \pi d$$

$$- \sum_{i=1}^{N_b} \sum_{j=1}^{N_b} \bar{Z}^{k}_{sm,ri}\ \bar{W}^{k}_{ri,rj}\ \bar{Z}^{k}_{rj,sn} \ . \tag{3.105}$$

Substituting for $\bar{Z}_{m,n}$ in eqn.3.102 :

$$\bar{S}_{in} = \sum_{m=1}^{N_s} \sum_{n=1}^{N_s} \bar{Z}^{L}_{sm,sn}\ \bar{I}_{sn}\ \bar{I}^{*}_{sm} + \bar{Z}^{A}_{sm,sn}\ \bar{I}_{sn}\ \bar{I}^{*}_{sm} \ . \tag{3.106}$$

The total complex power flowing in at the machine terminals may therefore be divided into two components:

$$\bar{S}_{in} = \bar{S}_s + \bar{S}_a \ , \tag{3.107}$$

in which $\bar{S}_s$ is the complex power consumed in the stator itself, and $\bar{S}_a$ is that which crosses the airgap. From eqn.3.106,

$$\bar{S}_s = \sum_{m=1}^{N_s} \sum_{n=1}^{N_s} \bar{Z}^{L}_{sm,sn}\ \bar{I}_{sn}\ \bar{I}^{*}_{sm}$$

$$= P_s + jQ_s \ . \tag{3.108}$$

and

$$\bar{S}_a = \sum_{m=1}^{N_s} \sum_{n=1}^{N_s} \bar{Z}^A_{sm,sn}\ \bar{I}_{sn}\ \bar{I}^*_{sm}$$

$$= P_a + jQ_a \ . \qquad (3.109)$$

From eqn.3.104, $\bar{S}_a$ is the sum of complex powers flowing into the airgap on all possible pole numbers, i.e.,

$$\bar{S}_a = \sum_{\nu_k} \bar{S}^k_a \ , \qquad (3.110)$$

where

$$\bar{S}^k_a = \sum_{m=1}^{N_s} \sum_{n=1}^{N_s} \bar{Z}^{kA}_{sm,sn}\ \bar{I}_{sn}\ \bar{I}^*_{sm}$$

$$= P^k_a + jQ^k_a \ . \qquad (3.111)$$

Eqn.3.111 may be used to define the ν_k-th harmonic airgap power factor :

$$\lambda_k = \sqrt{\left(\frac{\{P^k_a\}^2}{\{P^k_a\}^2 + \{Q^k_a\}^2} \right)} \ . \qquad (3.112)$$

At present, the only sources of active power loss included in the model are the stator windings and rotor cage. The copper loss in the stator windings is given by

$$P_s = \sum_{n=1}^{N_s} \left| \bar{I}_{sn} \right|^2 R_{sn} \qquad (3.113)$$

while that in the rotor cage is obtained by summing the individual components dissipated in the bars, the end-rings, and the inter-rings.

With reference to Fig.3.2, the ν_k-th harmonic loss in the rotor bars is

$$P_{bar}^k = \sum_{i=1}^{N_b} N_r \left| \bar{I}_{ri}^k - \bar{I}_{ri}^k e^{jk\lambda_r} \right|^2 Re\{\bar{Z}_{bi}^k\}$$

$$= 4\, N_r \sin^2(k\lambda_r/2) \sum_{i=1}^{N_b} \left| \bar{I}_{ri}^k \right|^2 Re\{\bar{Z}_{bi}^k\} \; . \qquad (3.114)$$

In the end-rings, it is given by

$$P_{er}^k = N_r \left| \bar{I}_{r1}^k \right|^2 Re\{\bar{Z}_{er}^k\} + N_r \left| \bar{I}_{rN_b}^k \right|^2 Re\{\bar{Z}_{er}^k\} \; , \qquad (3.115)$$

and in the inter-rings, by

$$P_{ir}^k = \sum_{i=1}^{N_b-1} N_r \left| \bar{I}_{ri}^k - \bar{I}_{ri+1}^k \right|^2 Re\{\bar{Z}_{ai}^k\} \; . \qquad (3.116)$$

The bar and end-ring losses may be combined to give

$$P_{bar}^k + P_{er}^k = N_r \left| \bar{I}_{r1}^k \right|^2 \left[4 \sin^2(k\lambda_r/2)\, Re\{\bar{Z}_{b1}^k\} + Re\{\bar{Z}_{er}^k\} \right]$$

$$+ N_r \sum_{i=2}^{N_b-1} \left| \bar{I}_{ri}^k \right|^2 Re\{\bar{Z}_{bi}^k\}$$

$$+ N_r \left| \bar{I}_{rN_b}^k \right|^2 \left[4 \sin^2(k\lambda_r/2)\, Re\{\bar{Z}_{bN_b}^k\} + Re\{\bar{Z}_{er}^k\} \right] \qquad (3.117)$$

Substitution from eqns.3.98-3.100 makes it possible to re-write eqns.3.116 and 3.117 in terms of rotor-rotor coupling

impedances :

$$P_{ir}^{k} = N_r \sum_{i=1}^{N_b-1} \left| \bar{I}_{ri}^{k} - \bar{I}_{ri+1}^{k} \right|^2 \mathrm{Re}\{\bar{Z}_{ri,ri+1}^{k}\} \quad , \quad (3.118)$$

and

$$P_{bar}^{k} + P_{er}^{k} = N_r \, \mathrm{Re} \left\{ \left| \bar{I}_{r1}^{k} \right|^2 \left[\bar{Z}_{r1,r1}^{k} + \bar{Z}_{r1,r2}^{k} \right] \right.$$

$$+ \sum_{i=2}^{N_b-1} \left| \bar{I}_{ri}^{k} \right|^2 \left[\bar{Z}_{ri,ri-1}^{k} + \bar{Z}_{ri,ri}^{k} + \bar{Z}_{ri,ri+1}^{k} \right]$$

$$\left. + \left| \bar{I}_{rN_b}^{k} \right|^2 \left[\bar{Z}_{rN_b,rN_b}^{k} + \bar{Z}_{rN_b,rN_b-1}^{k} \right] \right\} . \quad (3.119)$$

For two complex numbers $\bar{z}_1$ and $\bar{z}_2$:

$$\left| \bar{z}_1 - \bar{z}_2 \right|^2 = \bar{z}_1^{*} \, (\bar{z}_1 - \bar{z}_2) + \bar{z}_2^{*} \, (\bar{z}_1 - \bar{z}_2)$$

Having made such a substitution for $\left| \bar{I}_{ri}^{k} - \bar{I}_{ri+1}^{k} \right|^2$ in eqn. 3.119, the bar, end- and inter-ring losses may be summed to give

$$P_r^{k} = P_{bar}^{k} + P_{er}^{k} + P_{ir}^{k}$$

$$= N_r \, \mathrm{Re} \{ \bar{I}_{r1}^{k*} [\bar{Z}_{r1,r1}^{k} \bar{I}_{r1}^{k} + \bar{Z}_{r1,r2}^{k} \bar{I}_{r2}^{k}]$$

$$+ \bar{I}_{r2}^{k*} [\bar{Z}_{r2,r1}^{k} \bar{I}_{r1}^{k} + \bar{Z}_{r2,r2}^{k} \bar{I}_{r2}^{k} + \bar{Z}_{r2,r3}^{k} \bar{I}_{r3}^{k}]$$

$$\vdots$$

$$+ \bar{I}_{rN_b}^{k*} [\bar{Z}_{rN_b,rN_b-1}^{k} \bar{I}_{rN_b-1}^{k} + \bar{Z}_{rN_b,rN_b}^{k} \bar{I}_{rN_b}^{k}] \} . \quad (3.120)$$

Since $\bar{Z}_{ri,rj}^{k} = 0$ when $j<i-1$ and $j>i+1$, the ν_k-th harmonic rotor copper loss may be expressed in the compact form :

$$P_r^k = N_r \, \mathrm{Re} \left\{ \sum_{i=1}^{N_b} \bar{I}_{ri}^{k*} \sum_{j=1}^{N_b} \bar{Z}_{ri,rj}^{k} \, \bar{I}_{rj}^{k} \right\} , \qquad (3.121)$$

and the total copper loss in the machine is then

$$P_{loss} = P_s + \sum_{\nu_k} P_r^k \quad . \qquad (3.122)$$

The output power is obtained, in the usual manner, from

$$P_{out} = P_{in} - P_{loss} \qquad (3.123)$$

while the overall efficiency is given by

$$\eta = 1 - P_{loss} / P_{in} \, . \qquad (3.124)$$

The ν_k-th harmonic rotor efficiency may be defined in a similar way:

$$\eta_k = 1 - P_r^k / P_a^k \, , \qquad (3.125)$$

although it is possible to relate the airgap input power to the rotor loss directly, giving a much simpler expression. From eqn.3.112,

$$P_k^a = \mathrm{Re} \, \{\bar{S}_a^k\} \, . \qquad (3.126)$$

where, from eqns.3.105, 3.10 and 3.2,

$$\bar{S}_a^k = \sum_{m=1}^{N_s} \sum_{n=1}^{N_s} \bar{Z}_{sm,sn}^{kA} \, \bar{I}_{sn} \, \bar{I}_{sm}^{*}$$

$$= \sum_{m=1}^{N_s} \sum_{n=1}^{N_s} \bar{Z}_{sm,sn}^{k} \, \bar{I}_{sn} \, \bar{I}_{sm}^{*}$$

$$+ \sum_{m=1}^{N_s} \sum_{i=1}^{N_b} \bar{Z}^k_{sm,ri}\ \bar{I}_{ri}\ \bar{I}^*_{sm} \ . \qquad (3.127)$$

On substitution from eqn.3.33, it can be seen that the first term in eqn.3.127 is wholly imaginary, since it may be written as

$$\sum_{m=1}^{N_s} \sum_{n=1}^{N_s} \bar{Z}^k_{sm,sn}\ \bar{I}_{sn}\ \bar{I}^*_{sm} = \frac{j\omega\mu_0 \pi d}{k^2} \sum_{i=1}^{N_b} \frac{a_i}{g_i} \left|\bar{J}^k_s\right|^2 \qquad (3.128)$$

where $\bar{J}^k_s$, the ν_k-th harmonic stator-driven airgap MMF, is defined by

$$\bar{J}^k_s = \sum_{n=1}^{N_s} \bar{C}^k_{sn}\ \bar{I}_{sn} \ . \qquad (3.129)$$

The second term in eqn.3.127 may be expressed, after substitution from eqn 3.56, as

$$\sum_{m=1}^{N_s} \sum_{i=1}^{N_b} \bar{Z}^k_{sm,ri}\ \bar{I}_{ri}\ \bar{I}^*_{sm}$$

$$= \frac{j\omega\mu_0 \pi d}{k^2}\ N_r\ \bar{A}^k_r\ \bar{J}^{k*}_s \sum_{i=1}^{N_b} \frac{a_i\ K^k_i\ \bar{I}^k_{ri}}{g_i}\ e^{jkx_i \tan\gamma} \ . \qquad (3.130)$$

The relationship between the stator MMF and the rotor loop currents may be deduced from eqn.3.4:

$$\sum_{n=1}^{N_s} \bar{Z}^k_{ri,sn}\ \bar{I}_{sn} = - \sum_{j=1}^{N_b} \bar{Z}^k_{ri,rj}\ \bar{I}^k_{rj} \ . \qquad (3.131)$$

Substituting from eqn.3.56,

$$\bar{J}_s^k = - \sum_{j=1}^{N_b} \bar{Z}_{ri,rj}^k \, \bar{I}_{rj}^k \, / \, \bar{M}_i^k \, , \qquad (3.132)$$

where $\bar{M}_i^k$ is defined by

$$\bar{M}_i^k = - \frac{j\omega\mu_0 a_i \pi d}{k^2 g_i} \, s_k \, K_i^k \, \bar{A}_r^{k*} \, e^{-jkx_i \tan\gamma} \, . \qquad (3.133)$$

Eqn.3.130 may therefore be written as

$$\sum_{m=1}^{N_s} \sum_{i=1}^{N_b} \bar{Z}_{sm,ri}^k \, \bar{I}_{ri} \, \bar{I}_{sm}^*$$

$$= \frac{N_r}{s_k} \sum_{i=1}^{N_b} \bar{I}_{ri}^k \sum_{j=1}^{N_b} \bar{Z}_{ri,rj}^{k*} \, \bar{I}_{rj}^{k*} \, . \qquad (3.134)$$

The v_k-th harmonic airgap input power then becomes

$$P_a^k = \mathrm{Re} \left\{ \frac{N_r}{s_k} \sum_{i=1}^{N_b} \bar{I}_{ri}^k \sum_{j=1}^{N_b} \bar{Z}_{ri,rj}^{k*} \, \bar{I}_{rj}^{k*} \right\}$$

$$= \frac{N_r}{s_k} \, \mathrm{Re} \left\{ \sum_{i=1}^{N_b} \bar{I}_{ri}^{k*} \sum_{j=1}^{N_b} \bar{Z}_{ri,rj}^k \, \bar{I}_{rj}^k \right\} \, . \qquad (3.135)$$

Substitution for P_a and P_r into eqn.3.126 gives the familiar relationship between rotor efficiency and slip :

$$\eta_k = 1 - s_k \, . \qquad (3.136)$$

Torque is obtained by integrating the product of stator-driven MMF and rotor-driven flux density over the entire

airgap surface of the machine:

$$T\ (t) = d/2 \int_{x=-w/2}^{w/2} \int_{y=-\pi d/2}^{\pi d/2} j_s(y,t)\ b_{ri}(x,y,t)\ dx\ dy\ , \tag{3.137}$$

where

$$j_s(y,t) = \mathrm{Re}\left\{ \sum_{\nu_k} \sqrt{2}\ \bar{J}_s^k\ e^{j(\omega t - ky)} \right\}\ , \tag{3.138}$$

and

$$b_{ri}(x,y,t) = \mathrm{Re}\left\{ \sum_{\nu_k} \sqrt{2}\ \bar{B}_{ri}^k\ e^{j\omega t}\ e^{-jk(y+x\tan\gamma)} \right\}. \tag{3.139}$$

For two complex numbers $\bar{z}_1$ and $\bar{z}_2$, it can be shown that

$$2\ \mathrm{Re}\{\bar{z}_1\}\ \mathrm{Re}\{\bar{z}_2\} = \mathrm{Re}\{\bar{z}_1\bar{z}_2\} + \mathrm{Re}\{\bar{z}_1\bar{z}_2^*\}\ .$$

Using this identity,

$$j_s(y,t)\ b_{ri}(x,y,t) =$$

$$\mathrm{Re}\left\{ \sum_{\nu_k} \sum_{\nu_l} \bar{J}_s^k\ \bar{B}_{ri}^l\ e^{j2\omega t}\ e^{-j(k+l)y}\ e^{-jlx\tan\gamma} \right\}$$

$$+\ \mathrm{Re}\left\{ \sum_{\nu_k} \sum_{\nu_l} \bar{J}_s^k\ \bar{B}_{ri}^{l*}\ e^{-j(k-l)y}\ e^{jlx\tan\gamma} \right\}. \tag{3.140}$$

After the integrations have been performed, eqn.3.137 becomes

$$T(t) = T_s + \mathrm{Re}\{ \bar{T}_p e^{j2\omega t} \} , \qquad (3.141)$$

where the steady torque T_s, produced by the interaction of airgap MMF and flux density waves of the same harmonic order and direction of rotation, is given by

$$T_s = \frac{\pi d^2}{2} \mathrm{Re}\left\{ \sum_{\nu_k} \bar{J}_s^k \sum_{i=1}^{N_b} a_i K_i^k \bar{B}_{ri}^{k*} e^{jkx_i \tan\gamma} \right\} . \qquad (3.142)$$

The second term in eqn.3.141 represents the twice-supply frequency pulsating torque, caused by the interaction of harmonic MMF and flux waves of the same pole number and opposite directions of rotation. It is given by

$$\bar{T}_p = \frac{\pi d^2}{2} \sum_{\nu_k} \bar{J}_s^k \sum_{i=1}^{N_b} a_i K_i^k \bar{B}_{ri}^{-k} e^{jkx_i \tan\gamma} . \qquad (3.143)$$

The ν_k-th harmonic component of steady torque may be separated from eqn.3.142 to give

$$T_s^k = \frac{\pi d^2}{2} \mathrm{Re}\left\{ \bar{J}_s^k \sum_{i=1}^{N_b} a_i K_i^k \bar{B}_{ri}^{k*} e^{jkx_i \tan\gamma} \right\} . \qquad (3.144)$$

Substituting for $\bar{B}_{ri}^k$ from eqns.3.71 and 3.68, and for $\bar{J}_s^k$ from eqn.3.132,

$$T_s^k = \frac{N_r \nu_k}{s_k} \mathrm{Re}\left\{ \sum_{i=1}^{N_b} \bar{I}^{k*}_{ri} \sum_{j=1}^{N_b} \bar{Z}^k_{ri,rj} \bar{I}^k_{rj} \right\} . \qquad (3.145)$$

Finally, reference to eqn.3.121 yields the well-known relationship between harmonic torque and rotor copper loss:

$$T_s^k = \frac{N_r \nu_k}{\omega s_k} P_r^k . \qquad (3.146)$$

An attempt is made to include the finite permeability of the iron in the model by increasing the airgap length to allow for the additional MMF dropped in the iron portions of the magnetic circuit. However, as discussed in Section 3.1, it is necessary to ignore harmonic effects in the iron, and to consider only the principal harmonic component of flux.

The magnetic circuit of the machine can be divided into five parts, magnetically connected in series:

(1) stator core;

(2) stator teeth;

(3) rotor core;

(4) rotor teeth;

(5) airgap.

As a first estimate, the flux levels in each of these portions can be calculated from the airgap flux density, using the expressions derived in Appendix 8.3. The MMFs required in the iron are obtained from the appropriate magnetisation curves. The overall MMF is the sum of the individual components, and the ratio of total to airgap MMF is known as the saturation factor. The modified gap length, obtained by multiplying the original gap length by this quantity, is subsequently used to obtain improved values of coupling impedances.

The skewed nature of the rotor cage and the presence of inter-rings introduce axial variations in flux levels, both in the airgap, and in the iron. The accurate determination of a saturation factor becomes extremely difficult under these circumstances, since it is the resultant of the stator- and rotor-driven flux density waves which determine the flux in the iron. The problem is avoided by performing the magnetic circuit calculations at the synchronous speed of the principal harmonic, since, at this speed, the cor-

responding component of rotor current is zero. A different saturation factor is evaluated for each band of the machine, and the effective gap lengths thus modified are then assumed to remain constant over the entire speed range.

Once the flux densities in the various parts of the magnetic circuit are known, the fundamental-frequency iron losses in the stator core and teeth can be deduced from the manufacturer's curves. The corresponding losses in the rotor are ignored; at rated speed they are very small since the slip frequency is low. Iron losses calculated in this way are included in the analysis by adding them to the input power and to the stator and rotor copper losses. With this procedure, a change in terminal power factor is obtained, but the input current remains unaltered.

3.5 Search Coil EMFs

Experimental verification of the inter-ring model is provided in part by a search-coil investigation of airgap flux density. Several sets of single-turn search coils were affixed to the airgap surface of the stator, and the magnitude and phase of the EMFs induced in them by the travelling flux waves were measured and compared with values predicted by the theory. Details of the method adopted and the results obtained are given in Section 5.2.3.

In this section, an expression is derived for the EMF induced in a rectangular search coil of axial length a_c and circumferential width b_c, positioned with its centre at stator co-ordinates $x=x_c$ and $y=y_c$. The coil is allowed to overlap band boundaries (inter-rings or end-rings), but to take this into account it is necessary to divide the area of the coil into several sub-areas, each of which is situated wholly within one band. If the search coil spans N' bands, from the j-th onwards, then the sub-region which occupies the i-th band of the machine is assumed to be centred at $x=x_{ci}$, and to be of width a_{ci}. The total EMF induced in the coil is then the sum of the individual contributions from each sub-area:

$$u_c(t) = \sum_{i=j}^{j+N'-1} u_{ci}(t) \quad . \tag{3.147}$$

For the most common case where the coil is contained entirely within the j-th band, $N'=1$ and $u_c(t)=u_{cj}(t)$.

The EMF induced in the i-th band sub-region is calculated from the rate of change of flux linkage. The total stator-driven airgap flux density is obtained from

eqns.3.20 and 3.70 as

$$b_s(x,y,t) = \mathrm{Re}\left\{ \sum_{\nu_k} \sqrt{2}\ \bar{B}_s^k(x)\ e^{j(\omega t - ky)} \right\} , \qquad (3.148)$$

where, in the i-th band,

$$\bar{B}_s^k(x) = \frac{j\mu_0}{k g_i}\ \bar{J}_s^k \quad . \qquad (3.149)$$

The non-supply frequency EMFs induced in the search coil by the rotor slot-harmonic fields are ignored, and so the i-th band rotor-driven airgap flux density wave can be written, from eqns 3.70 and 3.71, as

$$b_{ri}(x,y,t) = \mathrm{Re}\left\{ \sum_{\nu_k} \sqrt{2}\ \bar{B}_{ri}^k\ e^{j\omega t}\ e^{-jk(y+x\tan\gamma)} \right\} , \qquad (3.150)$$

where

$$\bar{B}_{ri}^k = \frac{j\mu_0}{k g_i}\ \bar{J}_{ri}^k \quad . \qquad (3.151)$$

The resultant of the stator- and rotor-driven airgap flux densities, when integrated over the area of the sub-region occupying the i-th band, gives the required flux:

$$\varphi_{ci}(t) = \int_{x_{ci}-a_{ci}/2}^{x_{ci}+a_{ci}/2} \int_{y_c-b_c/2}^{y_c+b_c/2} b_s(y,t) + b_{ri}(x,y,t)\ dx\ dy \qquad (3.152)$$

Substituting from eqns.3.149-3.151, and performing the integrations,

$$\varphi_{ci}(t) = \mathrm{Re}\left\{ \sum_{\nu_k} \sqrt{2}\ \bar{\Phi}_{ci}^k\ e^{j\omega t} \right\} , \qquad (3.153)$$

where

$$\bar{\Phi}^{k}_{ci} = \frac{j\ \mu_0 a_{ci} b_c}{k\ g_i}\ K^{k}_{y}\ e^{-jky_c}\ [\bar{J}^{k}_{s} + \bar{J}^{k}_{ri}\ K^{k}_{xi}\ e^{-jkx_{ci}\tan\gamma}]\ . \tag{3.154}$$

K^{k}_{y} is the v_k-th harmonic pitch factor for the i-th sub-region of the search coil, defined by

$$K^{k}_{y} = \frac{\sin(\frac{kb_c}{2})}{\frac{kb_c}{2}}\ , \tag{3.155}$$

and K^{k}_{xi} is the corresponding skew factor:

$$K^{k}_{xi} = \frac{\sin\ (\frac{ka_{ci}}{2}\ \tan\gamma)}{\frac{ka_{ci}}{2}\ \tan\gamma}\ . \tag{3.156}$$

The EMF induced in the sub-area occupying the i-th band now takes the standard form

$$u_{ci}(t) = \mathrm{Re}\ \{\ \sqrt{2}\ \bar{U}_{ci}\ e^{j\omega t}\ \}\ , \tag{3.157}$$

where $\bar{U}_{ci}$ is expressed, from Faraday's law, by

$$\bar{U}_{ci} = -\ j\omega \sum_{v_k} \bar{\Phi}^{k}_{ci}\ , \tag{3.158}$$

for a single-turn coil.

The RMS phasor of the search-coil EMF is obtained by substituting from eqns.3.154 and 3.157 into 3.147, giving

$$\bar{U}_c = \omega\mu_o b_c \sum_{v_k} \sum_{i=j}^{j+N'-1} \frac{a_{ci}}{kg_i}\ K^{k}_{y}\ e^{-jky_c}\ [\bar{J}^{k}_{s} + \bar{J}^{k}_{ri}\ K^{k}_{xi}\ e^{-jkx_{ci}\tan\gamma}]\ . \tag{3.159}$$

3.6 Computer implementation

The coupling-impedance technique described above has been presented in a rigorous form suitable for direct computer implementation. It was therefore relatively straightforward to write a FORTRAN 77 program to provide steady-state performance predictions. As mentioned in Section 3.1, any number and configuration of stator windings is permitted. This means that it is possible to use the same code to analyse single-, two-, or three-phase machines, under balanced or unbalanced conditions. The supply voltages and stator winding details (the latter entered on a coil-by-coil basis) are contained within a separate file, permitting a comparison of performance predictions for the same basic machine with a number of different windings.

The computer used was a standard LSI-11/23, equipped with 256K memory and a KT-7 memory management unit [34]. Extensive use of virtual memory techniques was necessary to accommodate the 'harmonic' arrays. In all the expressions derived in previous sections, the harmonic summations have been shown as extending from minus to plus infinity. In practice, it is necessary to limit the number of harmonics included in the solution. In all the predictions presented here, stator-driven MMFs up to and including the forwards-rotating slot harmonics [18] were included.

The computer took approximately twenty minutes to produce sufficient data points to plot complete torque-speed characteristics, although the amount of processor time could be reduced if symmetrical inter-ring positions were assumed.

4. INVESTIGATION OF POWER-FACTOR IMPROVEMENT

4.1 Objective

Having developed an analytical technique capable of modelling machines with inter-rings, an investigation into the use of subharmonic fields for the purpose of power-factor improvement was undertaken. The objective was to modify the stator windings of a standard three-phase induction motor to produce a reduction in reactive power consumption and a consequent increase in power factor at rated speed.

The work carried out in the investigation was divided into two parts. The first involved the selection of a suitable design from the Bull Electric range of induction motors, while the second included an experimental investigation and verification of the effects of the subharmonic field on the performance of the chosen machine, with particular reference to the decrease in VAr demand and the accompanying reduction in output power.

The first of these is detailed below; the second is described in Section 5.3.

4.2 Selection of Prototype Machine

The process of selecting a motor suitable for the study of subharmonic-field effects began with a survey of all single-winding, single-cage designs in the Bull range. In order to calculate the airgap power factor, efficiency and ratio of input VArs to output watts for a particular machine, it is necessary to consider only the complex harmonic power entering the airgap from the stator :

$$\bar{S}_a^k = \sum_{m=1}^{N_s} \sum_{n=1}^{N_s} \bar{Z}_{sm,sn}^{kA} \, \bar{I}_{sn} \, \bar{I}_{sm}^{*} \quad . \tag{3.111}$$

From the definitions of airgap impedance $\bar{Z}_{sm,sn}^{kA}$ (eqn.3.105) and stator-driven airgap MMF $\bar{J}_s^k$ (eqn.3.132), the ν_k-th harmonic component of active power crossing the airgap to the rotor may be written as

$$P_a^k = \mathrm{Re}\,\{\bar{S}_a^k\} = \left|\bar{J}_s^k\right|^2 \mathrm{Re}\,\{\bar{F}^k\} \quad , \tag{4.1}$$

in which

$$\bar{F}^k = \frac{j\omega\mu_0 \pi d}{k^2} \sum_{i=1}^{N_b} \frac{a_i}{g_i} + \bar{F}_r^k \quad , \tag{4.2}$$

and

$$\bar{F}_r^k = \left(\frac{\omega\mu_0 \pi d}{k^2}\right)^2 s_k \, N_r \left|\bar{A}_r^k\right|^2 \sum_{i=1}^{N_b} \sum_{j=1}^{N_b} \frac{a_i}{g_i} \frac{a_j}{g_j} \, K_i^k \, K_j^k \, e^{-jkx_i \tan\gamma} e^{jkx_j \tan\gamma} \quad . \tag{4.3}$$

The corresponding component of reactive power can be similarly expressed:

$$Q_a^k = \text{Im}\ \{\bar{S}_a^k\} = \left|\bar{J}_s^k\right|^2\ \text{Im}\ \{\bar{F}^k\}\ , \qquad (4.4)$$

The ν_k-th harmonic airgap power factor is then given by eqn.3.112, the corresponding efficiency by eqn.3.125, and the ratio of input VArs to output watts by

$$\frac{Q_a^k}{P_{out}^k} = \frac{\text{Im}\ \{\bar{F}^k\}}{(1 - s_k)\ \text{Re}\ \{\bar{F}^k\}}\ . \qquad (4.5)$$

Using these expressions, the principal and subharmonic airgap power factor, efficiency and ratio of input VArs to output watts were calculated at rated speed for each machine. In this way it was possible to identify those designs which satisfied the conditions for effective rotor power-factor improvement developed in Section 2.2. Because of the large number of designs involved, the following simplifying assumptions were made:

(i) Negligible MMF was used to drive flux around the iron portions of the magnetic circuit. The saturation factor was then unity, and the iron loss zero.

(ii) The inter-rings were of negligible width, allowing the airgap length to remain constant.

Brief design details of the machines surveyed are given in Table 4.1a, and the results of the survey in 4.1b. In general, the choice of a suitable subharmonic pole number is governed by the extent of the trade-off between VAr reduction and machine de-rating. However, in order to minimise efficiency penalties, it was assumed throughout the work that the subharmonic pole number was two less than the

principal.

It can be seen from Table 4.1b that over half the designs investigated satisfied the required conditions for effective rotor power-factor improvement; the appropriate design numbers are marked with an asterisk (*). It is interesting to note that, for a given principal pole number and airgap diameter, the designs which demonstrated the greatest difference between principal and subharmonic power factors were generally those with the shortest core lengths. As mentioned in Section 3.3.2, the rotor bars extend beyond the ends of the core, and the designs are such that those with the shortest cores have the greatest proportion of bar length overhanging the core ends. For example, 75mm core-length motors incorporate bars of length 150mm, whereas bars 400mm long are used in machines with core lengths of 275mm. If the resistance of a bar is assumed to be proportional to its length, then reference to eqns. 2.10 and 2.11 indicates that, neglecting inter-ring effects, short-core designs are likely to have lower goodness factors and poorer power factors than their longer-length counterparts.

It can also be deduced from Table 4.1 that the use of subharmonic fields is likely to be more beneficial in machines with high principal pole numbers. In particular, the 12-pole design (number 28) showed a significant difference between principal and subharmonic input VArs to output watts ratios. Output power on the subharmonic wave is produced at a higher efficiency at rated speed, resulting in less derating for a given improvement in power factor.

Design number 6 is perhaps more representative of constant-speed, low-resistance machines, since it possesses copper bars and end-rings. It is usual for Bull's designs to incorporate cages of higher resistance by specifying copper

Table 4.1a: Brief details of surveyed machines

design number	rated slip (%)	rated output (kW)	core length (mm)	airgap diameter (mm)
1*	7.4	4.0	75	164
2*	8.2	5.8	100	164
3*	8.0	8.4	125	164
4*	7.2	9.9	150	164
5	6.9	12.5	175	164
6	2.6	14.5	200	164
7	6.5	13.9	200	164
8	6.2	16.1	225	164
9	5.6	14.0	250	164
10*	9.2	2.4	75	164
11*	8.7	3.8	100	164
12*	8.0	4.9	125	164
13*	8.0	7.3	150	164
14*	7.7	8.0	175	164
15*	7.5	9.1	200	164
16*	7.2	10.5	225	164
17*	6.9	12.4	250	164
18	6.7	10.7	150	196
19	7.9	20.9	175	196
20	7.1	45.4	300	196
21*	8.4	13.3	225	196
22*	8.0	18.8	275	196
23*	8.4	20.2	300	196
24*	7.8	10.3	150	196
25*	11.0	9.7	200	196
26*	9.0	12.3	250	196
27*	7.5	17.3	300	196
28*	8.1	5.4	275	196
29*	10.0	5.1	300	196
30	7.2	29.1	325	234
31*	7.8	27.7	200	234
32*	7.8	32.3	225	234
33*	7.0	35.1	250	234
34*	6.5	40.1	275	234
35	6.4	50.2	300	234
36	5.9	45.4	325	234
37*	8.0	16.2	300	234
38	5.5	37.6	350	268
39*	9.0	23.6	300	268
40*	5.9	45.4	375	268
41*	8.5	37.0	425	313

Table 4.1b: Results of Preliminary Survey

	P R I N C I P A L				S U B H A R M O N I C			
des. no.	pole no.	power factor (p.u.)	eff. (%)	Vars to watts	pole no.	power factor (p.u.)	eff. (%)	VArs to watts
1*	4	0.890	92.2	0.557	2	0.990	46.1	0.305
2*	4	0.923	91.8	0.453	2	0.989	45.9	0.332
3*	4	0.935	92.0	0.411	2	0.986	46.0	0.363
4*	4	0.936	92.8	0.404	2	0.984	46.4	0.392
5	4	0.931	93.1	0.422	2	0.972	46.5	0.524
6	4	0.866	97.4	0.594	2	0.881	48.7	1.105
7	4	0.932	93.5	0.415	2	0.967	46.7	0.563
8	4	0.926	93.8	0.434	2	0.962	46.9	0.608
9	4	0.923	94.4	0.442	2	0.958	47.2	0.638
10*	6	0.765	90.8	0.927	4	0.965	60.5	0.449
11*	6	0.802	91.3	0.816	4	0.965	60.9	0.447
12*	6	0.816	92.0	0.771	4	0.963	61.3	0.455
13*	6	0.838	92.0	0.707	4	0.960	61.3	0.473
14*	6	0.830	92.3	0.729	4	0.940	61.5	0.590
15*	6	0.838	92.5	0.704	4	0.935	61.7	0.613
16*	6	0.830	92.8	0.726	4	0.929	61.9	0.644
17*	6	0.832	93.1	0.717	4	0.925	62.1	0.660
18	4	0.943	93.3	0.380	2	0.985	46.6	0.378
19	4	0.951	92.1	0.351	2	0.990	46.1	0.312
20	4	0.955	92.9	0.336	2	0.981	46.5	0.431
21*	6	0.885	91.6	0.573	4	0.968	61.1	0.424
22*	6	0.876	92.0	0.600	4	0.965	61.3	0.446
23*	6	0.888	91.6	0.565	4	0.963	61.1	0.456
24*	8	0.733	92.2	1.008	6	0.942	69.2	0.517
25*	8	0.823	89.0	0.774	6	0.944	66.8	0.525
26*	8	0.794	91.0	0.841	6	0.939	68.3	0.535
27*	8	0.780	92.5	0.867	6	0.933	69.4	0.557
28*	12	0.528	91.9	1.748	10	0.843	76.6	0.833
29*	16	0.438	90.0	2.280	14	0.717	78.7	1.233
30	4	0.950	92.8	0.356	2	0.984	46.4	0.393
31*	6	0.920	92.2	0.464	4	0.966	61.5	0.439
32*	6	0.910	92.2	0.494	4	0.959	61.5	0.482
33*	6	0.907	93.0	0.498	4	0.956	62.0	0.493
34*	6	0.897	93.5	0.527	4	0.951	62.3	0.522
35	6	0.901	93.6	0.513	4	0.948	62.4	0.537
36	6	0.899	94.1	0.517	4	0.946	62.7	0.548
37*	8	0.806	92.0	0.797	6	0.936	69.0	0.545
38	4	0.957	94.5	0.321	2	0.981	47.2	0.418
39*	8	0.838	91.0	0.715	6	0.935	68.3	0.556
40*	8	0.816	94.1	0.754	6	0.924	70.6	0.585
41*	8	0.840	91.5	0.705	6	0.935	68.6	0.551

or brass bars, together with brass, or even steel, end-rings. For the low-resistance machine, it is noticeable that the subharmonic input VArs to output watts ratio is significantly higher than that of the principal harmonic.

The designs which demonstrated the greatest VAr-reduction capability were further investigated over a wider speed range. Figs.4.1-4.3 show a selection of the variations in principal and subharmonic airgap power factors and input VArs to output watts ratios for principal slips between 0 and 1.

Throughout earlier discussions, it has tacitly been assumed that only a single harmonic field is present in the airgap of the machine. In practice, both principal and subharmonic components are present simultaneously, with the bulk of the electromechanical energy conversion taking place on the principal pole-number wave. In Section 2.1 it was suggested that losses be kept constant while attempts were made to improve power factor, in order to avoid misleading results. The constraint of constant losses provides a convenient criterion for determining the relative proportions of the two harmonic fields.

Employing the notation of Section 2.2, the contribution to the total rotor copper loss from the subharmonic field may be written as

$$P_r^{k1} = (1 - r)\, P_r \ . \qquad (4.6)$$

The variable r represents the proportion of loss dissipated by the subharmonic component of rotor current :

$$P_r^{k2} = r\, P_r \ . \qquad (4.7)$$

Note that

$$P_r^{k1} + P_r^{k2} = P_r \quad \text{and} \quad 0 \leq r \leq 1 \ .$$

If r=0, the principal harmonic only is present, whilst if r=1, the sole source of rotor loss is the subharmonic field.

If both harmonics are included, the overall airgap efficiency is given by

$$\eta_a = 1 - P_r \ / \ P_a \ , \tag{4.8}$$

where P_a is the total active power crossing the airgap:

$$P_a = P_a^{k1} + P_a^{k2} \ . \tag{4.9}$$

The individual harmonic efficiencies are

$$\eta_{k1} = 1 - P_r^{k1} \ / \ P_a^{k1} \ ,$$

and (4.10)

$$\eta_{k2} = 1 - P_r^{k2} \ / \ P_a^{k2} \ .$$

Rearranging eqns.4.10 and substituting from 4.6 and 4.7,

$$P_a^{k1} = \frac{1 - r}{1 - \eta_{k1}} P_r \ ; \quad P_a^{k2} = \frac{r}{1 - \eta_{k2}} P_r \ . \tag{4.11}$$

In Section 3.4 it was shown that

$$\eta_{k1} = 1 - s_{k1} \ ; \quad \eta_{k2} = 1 - s_{k2} \ . \tag{4.12}$$

where s_{k1} and s_{k2} are the fractional rotor slips experienced by the principal and subharmonic fields respectively. Substituting eqns.4.12 into 4.11 and then into 4.8 enables the overall rotor efficiency to be expressed as a function of r :

$$\eta_a = 1 - \frac{s_{k1} \ s_{k2}}{r \ s_{k1} + (1 - r) \ s_{k2}} \ . \tag{4.13}$$

The overall airgap power factor is given by

$$\lambda_a = \sqrt{\left(\frac{\{P_a\}^2}{\{P_a\}^2 + \{Q_a\}^2}\right)} , \qquad (4.14)$$

in which Q_a is the total reactive power entering the airgap from the stator :

$$Q_a = Q_a^{k1} + Q_a^{k2} . \qquad (4.15)$$

The individual harmonic airgap power factors are

$$\left.\begin{aligned} \lambda_{k1} &= \sqrt{\left(\frac{\{P_a^{k1}\}^2}{\{P_a^{k1}\}^2 + \{Q_a^{k1}\}^2}\right)} , \\ \text{and} \qquad & \qquad (4.16) \\ \lambda_{k2} &= \sqrt{\left(\frac{\{P_a^{k2}\}^2}{\{P_a^{k2}\}^2 + \{Q_a^{k2}\}^2}\right)} . \end{aligned}\right\}$$

Rearranging eqns.4.16 and substituting for P_{k1} and P_{k2} from eqns.4.11 gives

$$Q_a^{k1} = \Delta_{k1} \Lambda_{k1} P_r , \qquad (4.17)$$

and

$$Q_a^{k2} = \Delta_{k2} \Lambda_{k2} P_r , \qquad (4.18)$$

where

$$\Delta_{k1} = (1 - r) / s_{k1} \quad ; \quad \Delta_{k2} = r / s_{k2} , \qquad (4.19)$$

and

$$\Lambda_{k1} = \sqrt{\left(\frac{1 - \{\lambda_{k1}\}^2}{\{\lambda_{k1}\}^2}\right)} \; ; \quad \Lambda_{k2} = \sqrt{\left(\frac{1 - \{\lambda_{k2}\}^2}{\{\lambda_{k2}\}^2}\right)} \; . \qquad (4.20)$$

Substituting eqns.4.17 and 4.18 into 4.15 and then into 4.14 enables the overall airgap power factor to be written as

$$\lambda_a = \sqrt{\left(\frac{[\Delta_{k1} + \Delta_{k2}]^2}{[\Delta_{k1} + \Delta_{k2}]^2 + [\Delta_{k1}\,\Lambda_{k1} + \Delta_{k2}\,\Lambda_{k2}]^2}\right)} \; . \qquad (4.21)$$

The above procedure may be repeated for the ratio of total airgap input VArs to output watts T_a to give

$$T_a = \frac{\Delta_{k1}\,\Lambda_{k1} + \Delta_{k2}\,\Lambda_{k2}}{[\Delta_{k1}\,\Lambda_{k1} \,/\, T_a^{k1}] + [\Delta_{k2}\,\Lambda_{k2} \,/\, T_a^{k2}]} \; , \qquad (4.22)$$

in which the individual harmonic ratios are defined by

$$T_a^{k1} = Q_a^{k1} \,/\, P_{out}^{k1} \; ; \quad T_a^{k2} = Q_a^{k2} \,/\, P_{out}^{k2} \; . \qquad (4.23)$$

For a given contribution to the total losses in the rotor cage from the subharmonic field (i.e., for a given r), the extent of the reduction in VAr demand and the cost in terms of output power can now be determined. The next step in selecting a suitable prototype design was therefore to use eqns.4.13, 4.21 and 4.22 to examine the variations with r of airgap power factor, efficiency and input VArs to output watts ratio, again at rated speed. Figs.4.4-4.6 illustrate the results for design numbers 1,6 and 28.

As the proportion of losses supplied by the subharmonic field is increased, the airgap power factor is seen to improve, while the efficiency is reduced. The critical quantity, the ratio of airgap input VArs to output watts, is

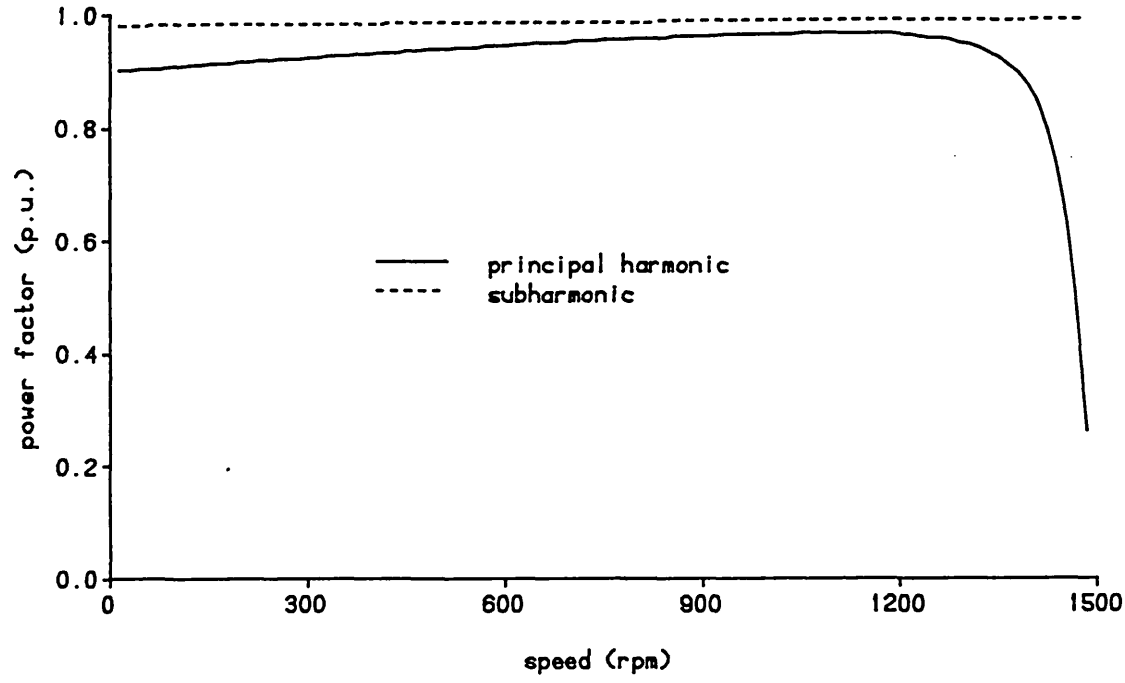


Fig.4.1a: Airgap power factor (design 1)

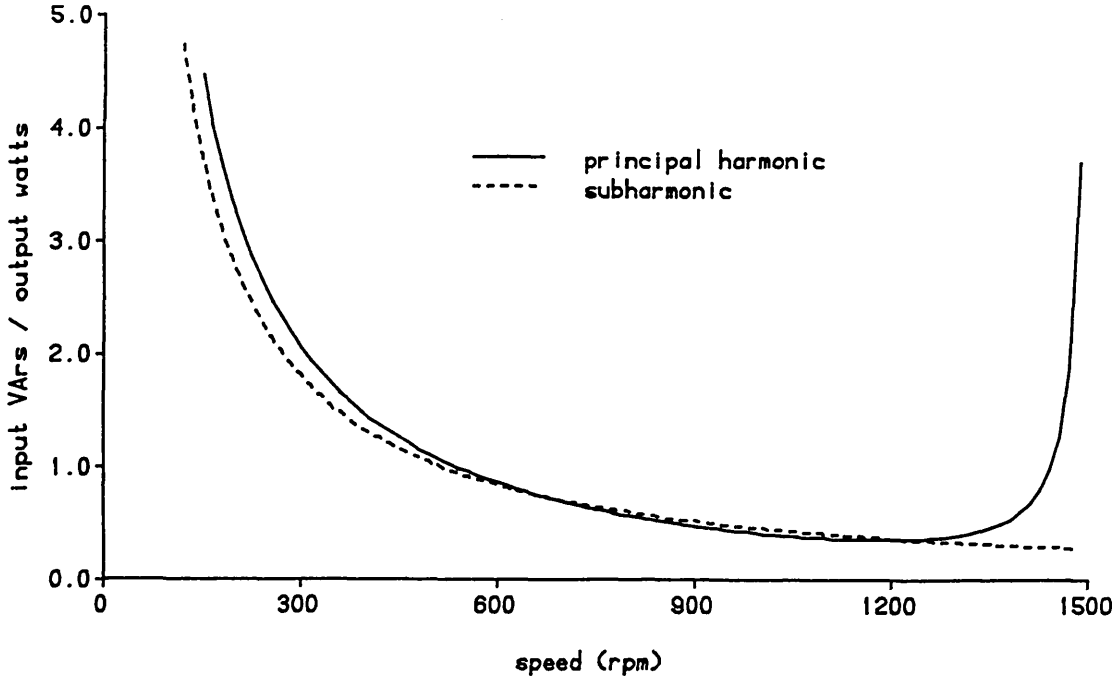


Fig.4.1b: Airgap input VArs to output watts ratio (design 1)

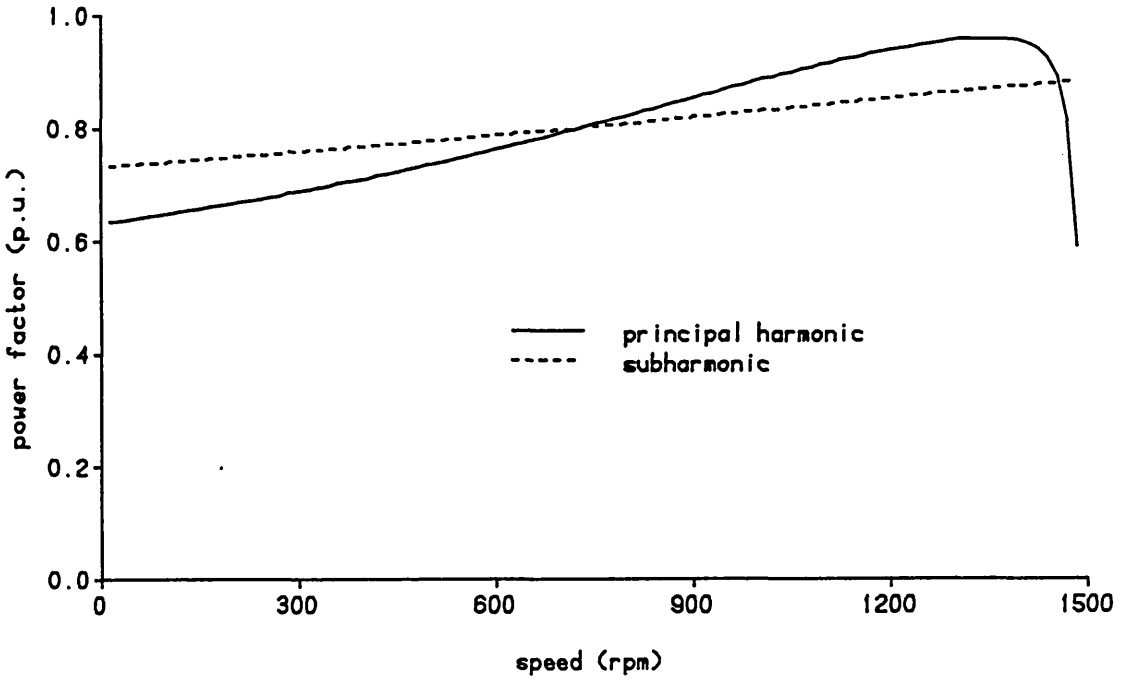


Fig.4.2a: Airgap power factor (design 6)

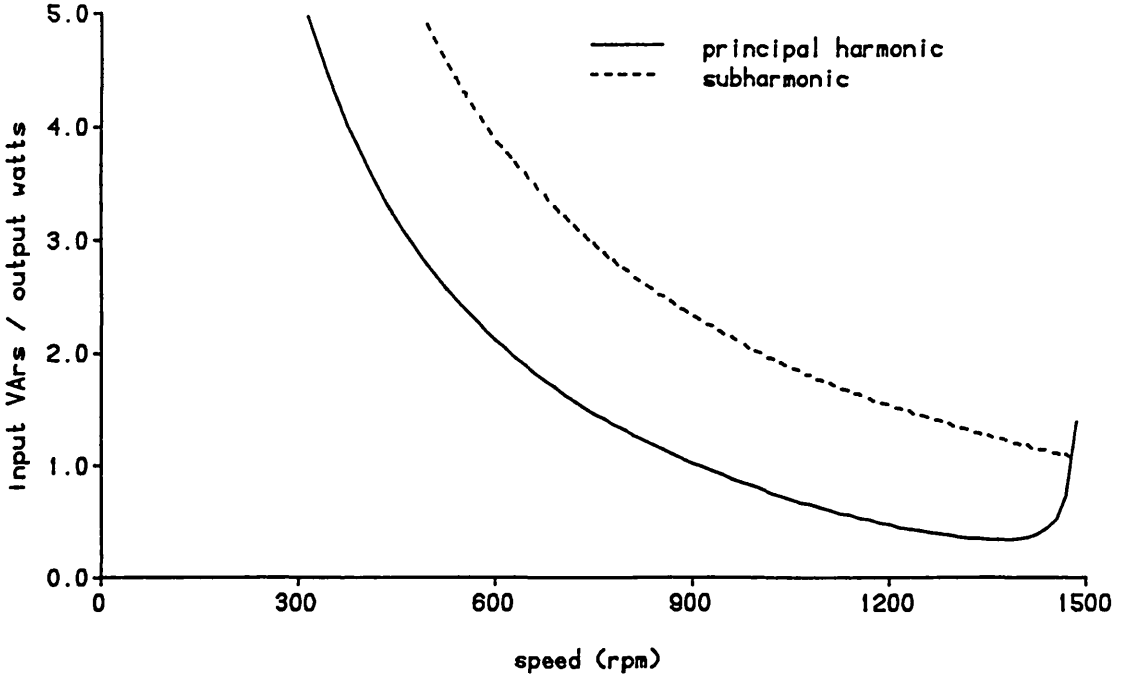


Fig.4.2b: Airgap input VArs to output watts ratio (design 6)

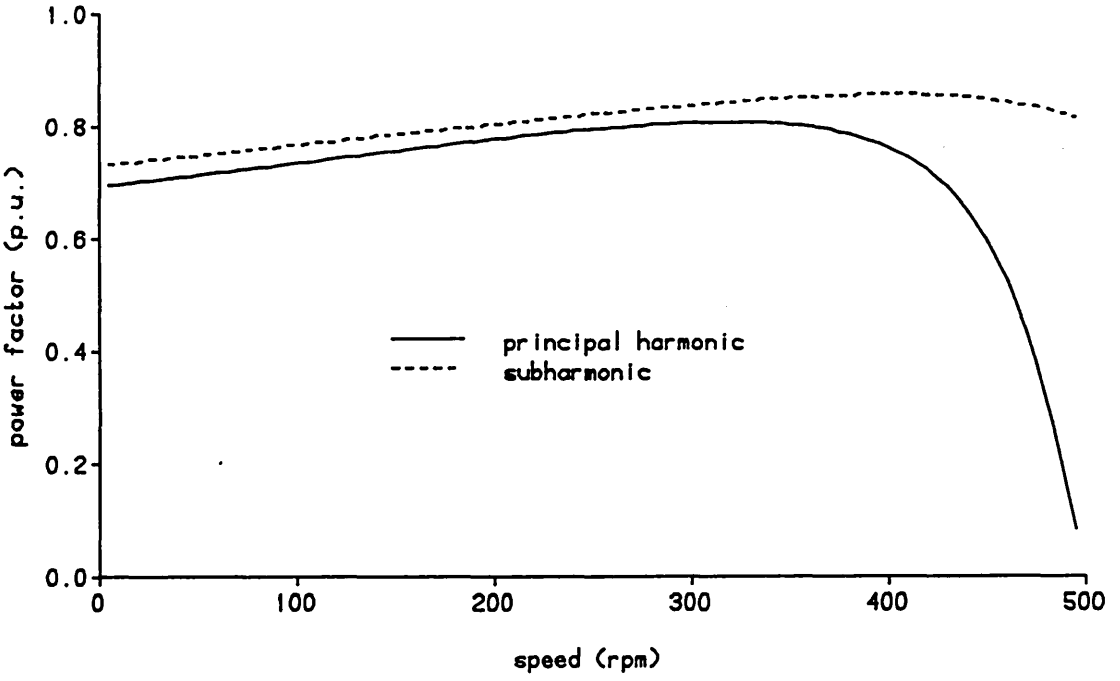


Fig.4.3a: Airgap power factor (design 28)

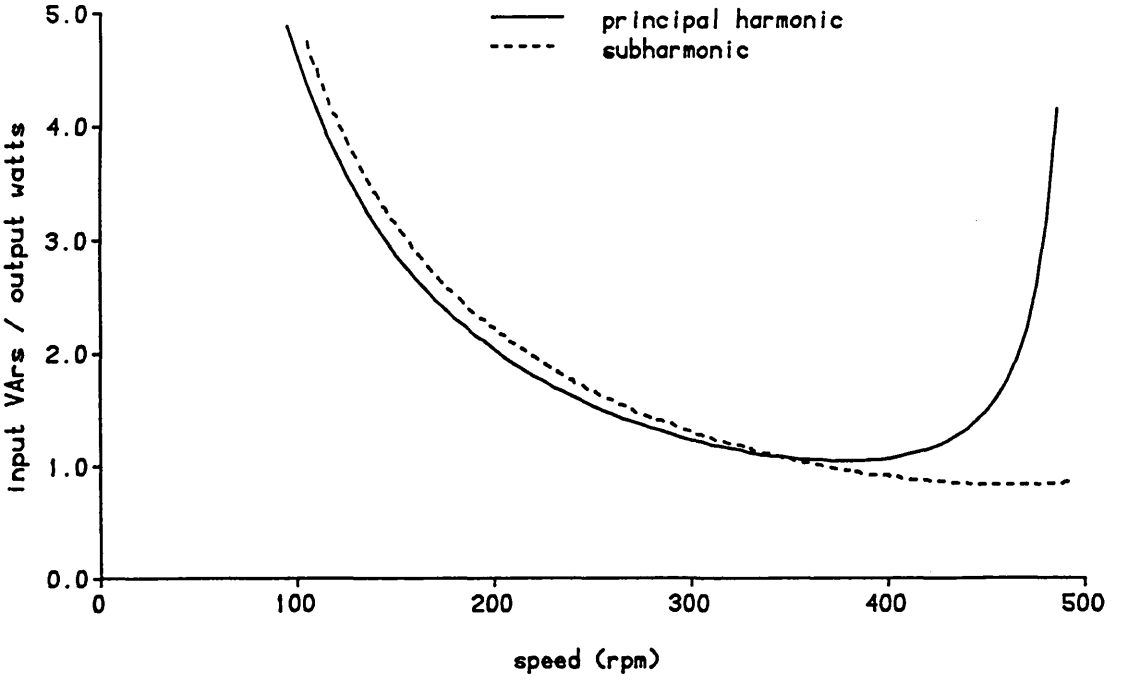


Fig.4.3b: Airgap input VArs to output watts ratio (design 28)

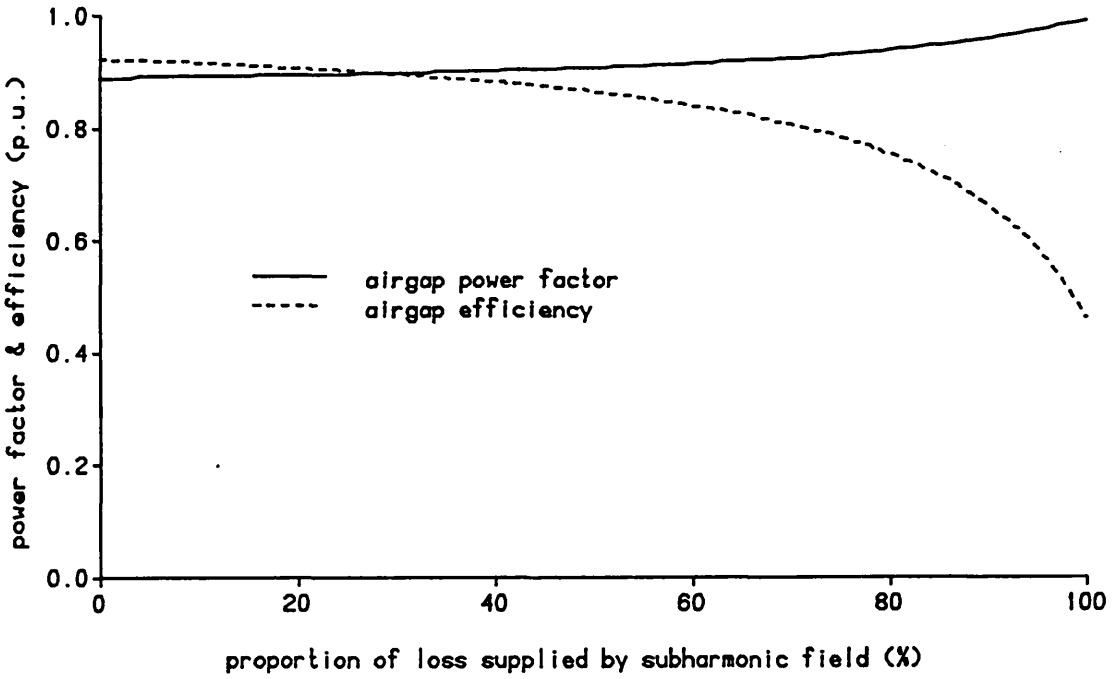


Fig.4.4a: Power factor and efficiency : variation with r (design 1)

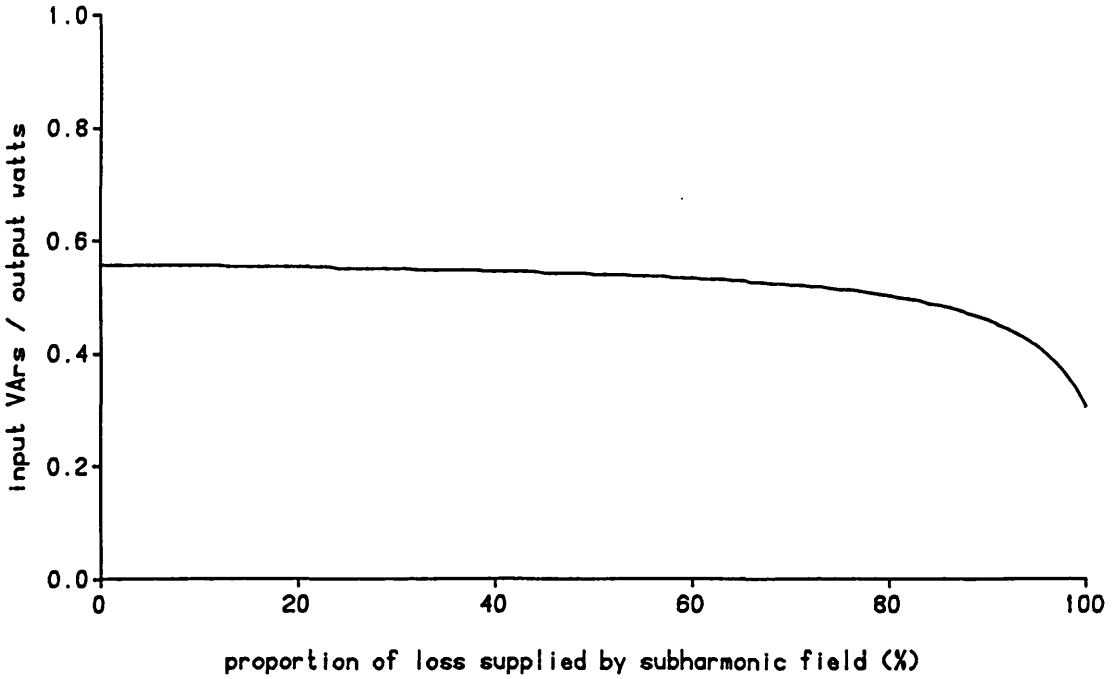


Fig.4.4b: Input VArs to output watts : variation with r (design 1)

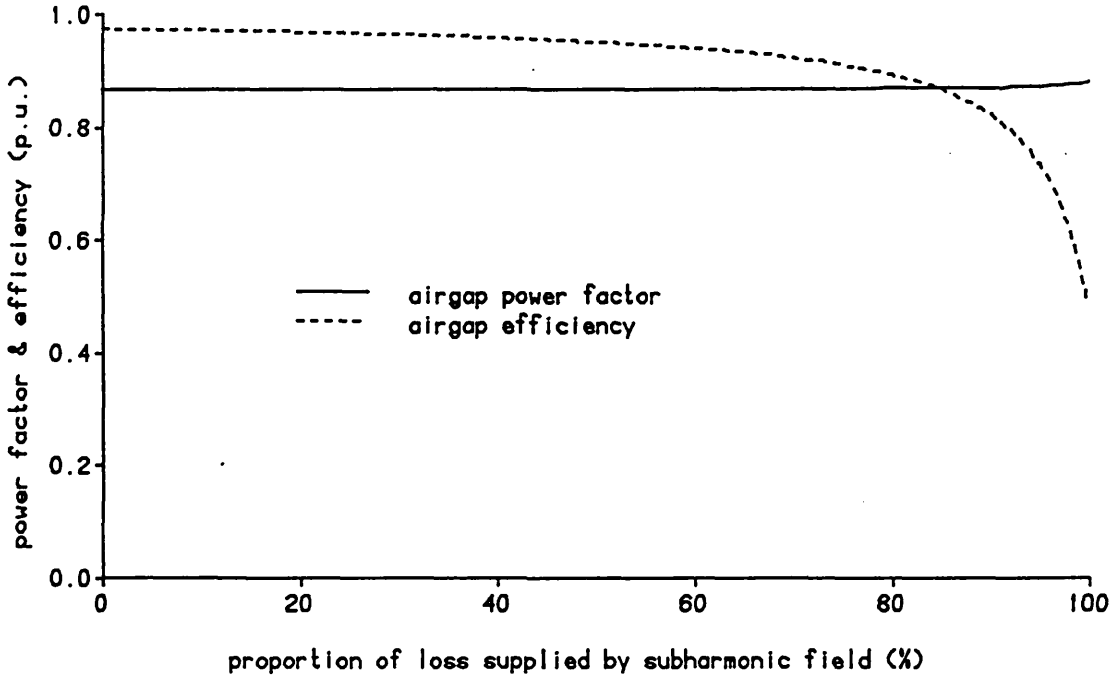


Fig.4.5a: Power factor and efficiency : variation with r (design 6)

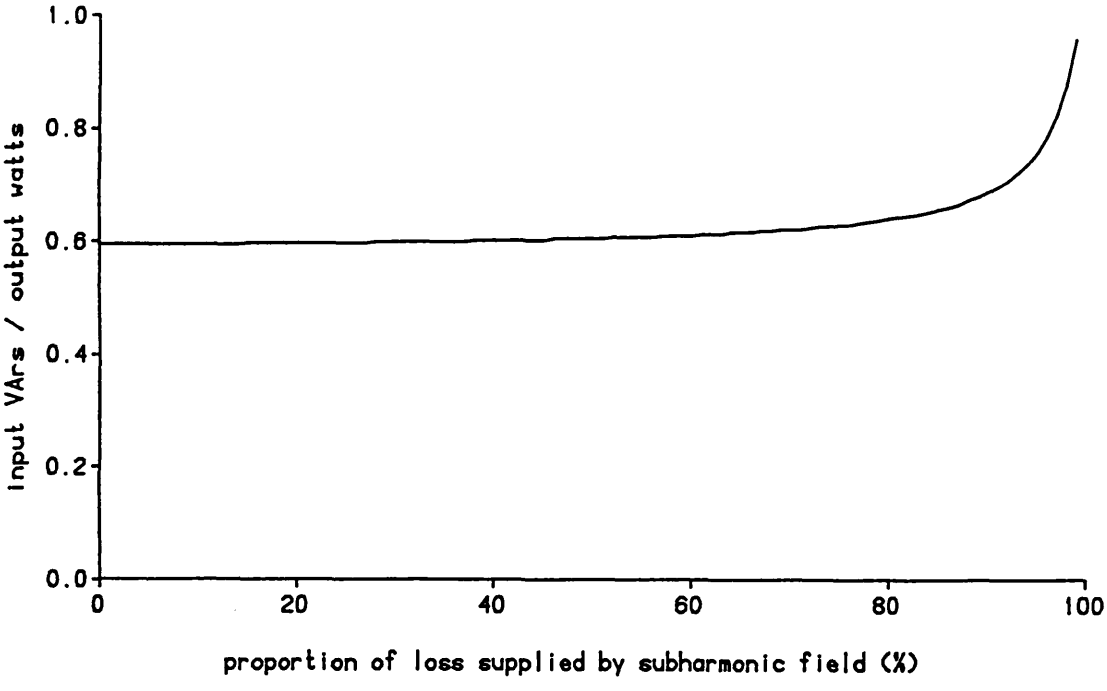


Fig.4.5b: Input VArs to output watts : variation with r (design 6)

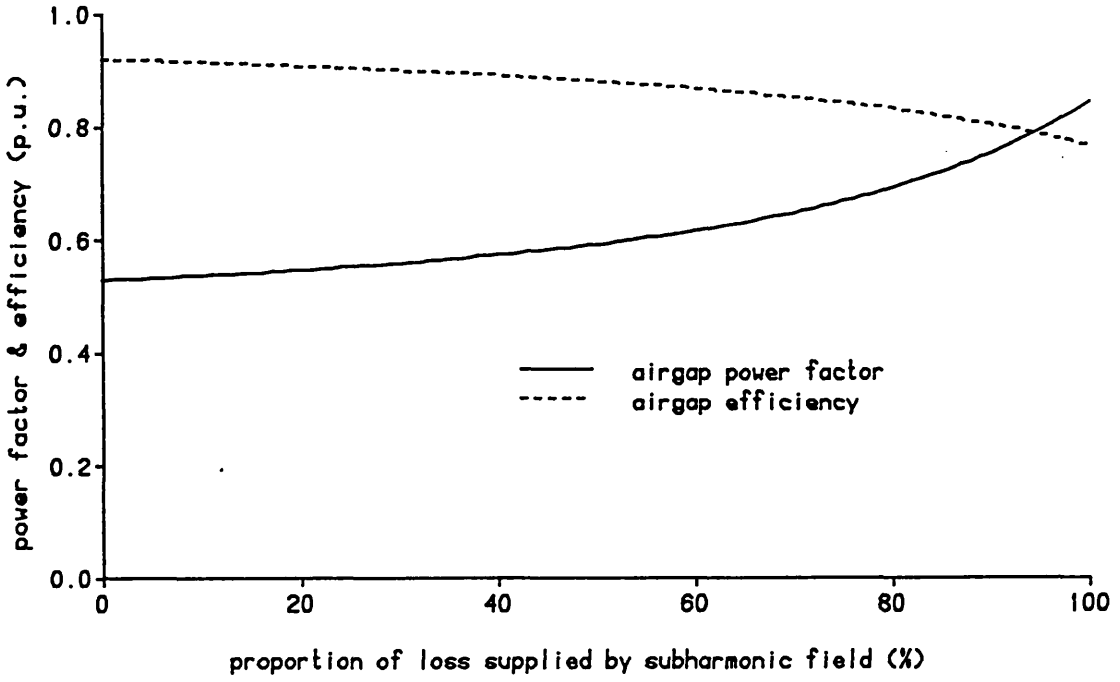


Fig.4.6a: Power factor and efficiency : variation with r (design 28)

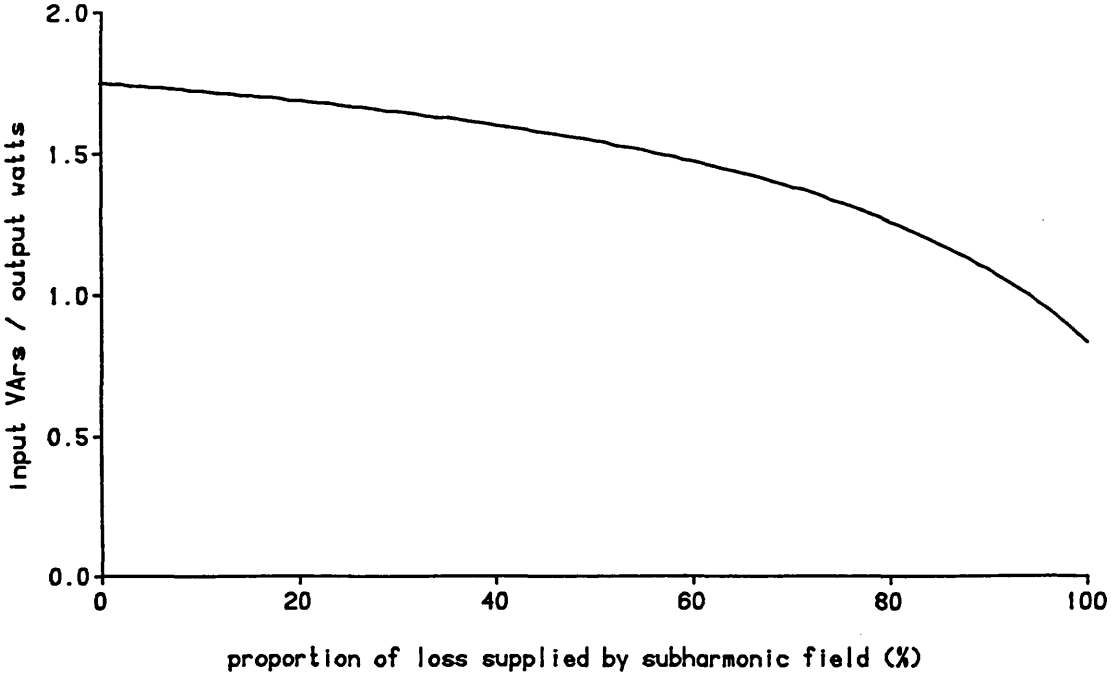


Fig.4.6b: Input VArs to output watts : variation with r (design 28)

also reduced, as required. The beneficial effect of the sub-harmonic field would appear to become progressively greater as the principal pole number increases.

Several different factors were considered in the final choice of a suitable design for the prototype machine. It was important to select a motor for which a measurable reduction in airgap input VArs was predicted, bearing in mind the difficulties involved in detecting small changes experimentally. It was intended that the test motor would be coupled to a DC load machine for the majority of the tests; the size of the load machines available at the time meant that the rated output of the prototype machine had to be kept below 10kW. Manufacturing constraints had also to be considered. Four- and six-pole machines are sold in large quantities by Bull, and for this reason they were keen to supply one such for the experimental investigation. It was finally decided to adopt design number 1. Although this motor exhibited only a marginal potential improvement in power factor for practical values of r, as can be seen from Fig. 4.4a, the choice was convenient since the stator of the machine had previously been used for test purposes by Bull themselves, and it was necessary only for them to manufacture a new rotor. Details of the chosen design are given in Table 4.2.

Table 4.2: Design details of original protoype machine

principal pole number	4
rated slip	7.4 %
rated output	4.0 kW
supply frequency	50 Hz
rated line voltage	415 V
connection	star
core length	75.0 mm
mean airgap diameter	164.4 mm
airgap length	0.65 mm
number of stator slots	48
stator slot opening	2.5 mm
number of turns per coil	30
winding type (single-layer)	concentric
copper resistivity (hot)	$2.39 \times 10^{-8} \Omega m$
end-turn leakage reactance per phase	2.17
stator back-iron (yoke) depth	21.0 mm
stator mean tooth width	4.8 mm
number of rotor slots	59
rotor slot opening	2.3 mm
bar width	2.0 mm
bar depth	16.0 mm
bar resistivity (hot)	$2.39 \times 10^{-8} \Omega m$
bar length	150.0 mm
end-ring width	20.0 mm
end-ring depth	8.5 mm
end-ring resistivity (hot)	$7.50 \times 10^{-8} \Omega m$
inter-ring resistivity (hot)	$2.39 \times 10^{-8} \Omega m$
rotor back-iron (yoke) depth	25.4 mm
rotor mean tooth width	5.4 mm

4.3 Design of Subharmonic Winding

Having selected a suitable design for the protoype machine, some consideration was given to the way in which the additional harmonic field was to be realised. Although it was perhaps possible to obtain the desired effect by some kind of grading of conductors in the existing stator arrangement, it was nevertheless decided to add seperate 2-pole windings to produce the subharmonic field. This was the simplest approach, offering a greater degree of flexibility, both at the design stage, and during the experimental part of the investigation. For example, the numbers of turns per coil in the main (principal pole-number) and subharmonic windings could be adjusted to maintain constant rotor copper losses, varying the contribution from the subharmonic field as required. In addition, it was possible to excite each three-phase set of windings separately prior to the main tests. This provided a convenient check on some of the parameters which were difficult to evaluate accurately (rotor bar resistivity, stator end-winding leakage, etc.). The first stage in the design process was the derivation of suitable expressions relating the principal and subharmonic rotor losses to the number of turns in each winding.

So far the analysis has been quite general, and is capable of accommodating any arrangement of stator conductors. In a balanced three-phase machine, however, the same distribtution of conductors is employed for each winding. Simplified expressions for the principal and subharmonic components of stator-driven MMF can be derived as a result. All three phases comprise identical series-connected sets of M coils, the n-th of which has N_n turns

and a pitch of α_n. The circumferential position of the n-th coil in the m-th phase (y_n in eqn.3.14) may be written as

$$y_n = \beta_m + \delta_n \ . \qquad (4.24)$$

β_m is the y co-ordinate of the axis of the m-th phase, and δ_n is the position of the n-th coil relative to this axis. The v_k-th harmonic conductor density distribution for the m-th winding may now be expressed, from eqn.3.14, as

$$\bar{C}^k_{sm} = \bar{A}^k_s \ e^{jk\beta_m} \ , \qquad (4.25)$$

where

$$\bar{A}^k_s = - \frac{2j}{\pi d} K^k_{bs} \sum_{n=1}^{M} N_n \sin(k\alpha_n/2) \ e^{jk\delta_n} \ . \qquad (4.26)$$

When the stator carries two distinct sets of windings, a seperate expression for $\bar{A}^k_s$ is needed in each case. For the main set

$$\bar{A}^{k1}_{s1} = - \frac{2j}{\pi d} K^{k1}_{bs} N_1 \sum_{n=1}^{M_1} \sin(k_1\alpha_{n1}/2) \ e^{jk\delta_{n1}} \ , \qquad (4.27)$$

and, for the subharmonic set,

$$\bar{A}^{k2}_{s2} = - \frac{2j}{\pi d} K^{k2}_{bs} N_2 \sum_{n=1}^{M_2} \sin(k_2\alpha_{n2}/2) \ e^{jk\delta_{n2}} \ . \qquad (4.28)$$

N_1 and N_2 are the numbers of turns per coil in each of the main and subharmonic phases respectively. It is implied that all coils in each set of windings possess the same number of turns; this is common industrial practice. In eqn.4.25, the winding numbers m=1,2 and 3 relate to the main red, yellow

and blue phases respectively, while numbers 4,5 and 6 refer to the corresponding windings in the subharmonic arrangement.

In order to obtain a forwards-rotating field with the desired number of poles, the axes of the three phase bands are displaced in space by $2\pi/3$ electrical degrees, i.e., $k\beta_m=2\pi/3$. For the principal harmonic wave produced by the main windings $k=k_1$ and, from eqn.4.25,

$$\bar{C}_{s1}^{k1} = \bar{A}_{s1}^{k1} \; ; \; \bar{C}_{s2}^{k1} = \bar{a}\,\bar{A}_{s1}^{k1} \; ; \; \bar{C}_{s3}^{k1} = \bar{a}^{*}\,\bar{A}_{s1}^{k1} \; , \qquad (4.29)$$

in which $\bar{a}=e^{j2\pi/3}$. Here it is assumed that the axis of the main red phase (m=1) coincides with the origin of stator co-ordinates. If the same is true of winding number 4, then, for $k=k_2$,

$$\bar{C}_{s4}^{k2} = \bar{A}_{s2}^{k2} \; ; \; \bar{C}_{s5}^{k2} = \bar{a}\,\bar{A}_{s2}^{k2} \; ; \; \bar{C}_{s6}^{k2} = \bar{a}^{*}\,\bar{A}_{s2}^{k2} \; . \qquad (4.30)$$

When each winding is supplied with the appropriate time-phased current, the desired forwards-rotating principal and subharmonic airgap fields are produced. If

$$\begin{aligned} &\bar{I}_{s1} = \bar{I}_1 \; ; \; \bar{I}_{s2} = \bar{a}^{*}\,\bar{I}_1 \; ; \; \bar{I}_{s3} = \bar{a}\,\bar{I}_1 \; ; \\ &\bar{I}_{s4} = \bar{I}_2 \; ; \; \bar{I}_{s5} = \bar{a}^{*}\,\bar{I}_2 \; ; \; \bar{I}_{s6} = \bar{a}\,\bar{I}_2 \; . \end{aligned} \qquad (4.31)$$

where $\bar{I}_1$ and $\bar{I}_2$ are the main and subharmonic stator currents, respecively, then the airgap MMFs are

$$\bar{J}_s^{k1} = \sum_{n=1}^{3} \bar{C}_{sn}^{k1}\,\bar{I}_{sn} \; ; \; \bar{J}_s^{k2} = \sum_{n=4}^{6} \bar{C}_{sn}^{k2}\,\bar{I}_{sn} \; . \qquad (4.32)$$

Substituting from eqns.4.29 and 4.30,

$$\bar{J}_s^{k1} = 3\ \bar{A}_{s1}^{k1}\ \bar{I}_{s1} \quad ; \quad \bar{J}_s^{k2} = 3\ \bar{A}_{s2}^{k2}\ \bar{I}_{s2} \ . \tag{4.33}$$

The harmonic components of active power crossing the airgap may now be written, from eqns.4.1 and 4.21, as

$$\begin{aligned} P_a^{k1} &= 9\ \left|\bar{A}_{s1}^{k1}\right|^2 \left|\bar{I}_1\right|^2\ \mathrm{Re}\ \{\bar{F}^{k1}\}\ ; \\ P_a^{k2} &= 9\ \left|\bar{A}_{s2}^{k2}\right|^2 \left|\bar{I}_2\right|^2\ \mathrm{Re}\ \{\bar{F}^{k2}\}\ . \end{aligned} \tag{4.34}$$

The dependence of the harmonic losses on the number of turns per coil may be highlighted by expressing the conductor densities thus

$$\bar{A}_{s1}^{k1} = N_1\ \bar{D}_{s1}^{k1} \quad ; \quad \bar{A}_{s2}^{k2} = N_2\ \bar{D}_{s2}^{k2} \ . \tag{4.35}$$

From eqns.4.27 and 4.28,

$$\bar{D}_{s1}^{k1} = -\frac{2j}{\pi d}\ K_{bs}^{k1} \sum_{n=1}^{M_1} \sin(k_1 \alpha_{n1}/2)\ e^{jk\delta_{n1}} \quad ,$$

and (4.36)

$$\bar{D}_{s2}^{k2} = -\frac{2j}{\pi d}\ K_{bs}^{k2} \sum_{n=1}^{M_2} \sin(k_2 \alpha_{n2}/2)\ e^{jk\delta_{n2}} \quad .$$

With reference to eqns.3.121 and 3.135, the individual harmonic losses in the rotor cage are

$$P_r^{k1} = s_{k1}\ P_a^{k1} \quad ; \quad P_r^{k2} = s_{k2}\ P_a^{k2} \ . \tag{4.37}$$

Substitution of eqns.4.36 into 4.35 and then into 4.34

therefore yields

$$P_r^{k1} = 9\ N_1^{\ 2}\ s_{k1} \left|\bar{D}_{s1}^{k1}\right|^2 \left|\bar{I}_1\right|^2\ \mathrm{Re}\ \{\bar{F}^{k1}\}\ ,$$

and (4.38)

$$P_r^{k2} = 9\ N_2^{\ 2}\ s_{k2} \left|\bar{D}_{s2}^{k2}\right|^2 \left|\bar{I}_2\right|^2\ \mathrm{Re}\ \{\bar{F}^{k2}\}\ .$$

The total copper loss in the cage is the sum of these components :

$$P_r = P_r^{k1} + P_r^{k2} \qquad (4.39)$$

It is also possible to derive simplified expressions for the winding currents $\bar{I}_1$ and $\bar{I}_2$. Suppose that the main and subharmonic sets of windings are excited from constant-voltage sources $\bar{V}_1$ and $\bar{V}_2$ respectively. Considering the red phases only, application of the basic impedance relation 3.1 yields

$$\bar{V}_1 = \sum_{n=1}^{3} \bar{Z}_{1,n}\ \bar{I}_{sn}\ ;\quad \bar{V}_2 = \sum_{n=4}^{6} \bar{Z}_{4,n}\ \bar{I}_{sn}\ . \qquad (4.40)$$

For the purpose of winding design, it is now necessary to make the assumption that the stator winding resistances and leakage reactances are small enough to be neglected at rated speed. As a result, reference to eqn.3.10 shows that

$$\bar{Z}_{m,n} = \bar{Z}_{sm,sn}^{A}\ , \qquad (4.41)$$

where $\bar{Z}_{sm,sn}^{A}$ is defined by eqn.3.105. From eqns.4.39 and 4.35:

$$\bar{Z}_{1,1} = N_1^2 \; \bar{F}^{k1} \; \left|\bar{D}_{s1}^{k1}\right|^2 \; ;$$

$$\bar{Z}_{1,2} = N_1^2 \; \bar{a} \; \bar{F}^{k1} \; \left|\bar{D}_{s1}^{k1}\right|^2 \; ; \qquad (4.42)$$

$$\bar{Z}_{1,3} = N_1^2 \; \bar{a}^* \; \bar{F}^{k1} \; \left|\bar{D}_{s1}^{k1}\right|^2 \; .$$

Substituting eqns.4.42 into 4.40,

$$\bar{V}_1 = \bar{Z}_1 \; \bar{I}_1 \; , \qquad (4.43)$$

where

$$\bar{Z}_1 = 3 \; N_1^2 \; \bar{F}^{k1} \; \left|\bar{D}_{s1}^{k1}\right|^2 \; . \qquad (4.44)$$

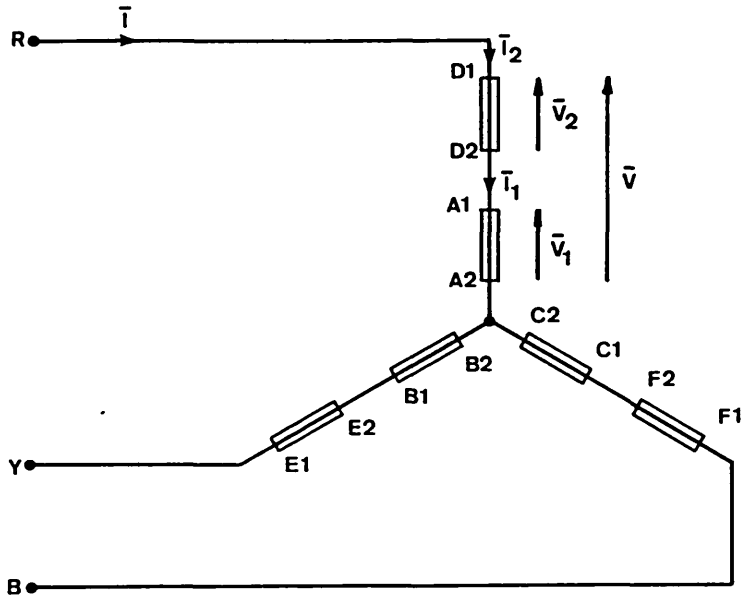
For the subharmonic set of windings,

$$\bar{V}_2 = \bar{Z}_2 \; \bar{I}_2 \; , \qquad (4.45)$$

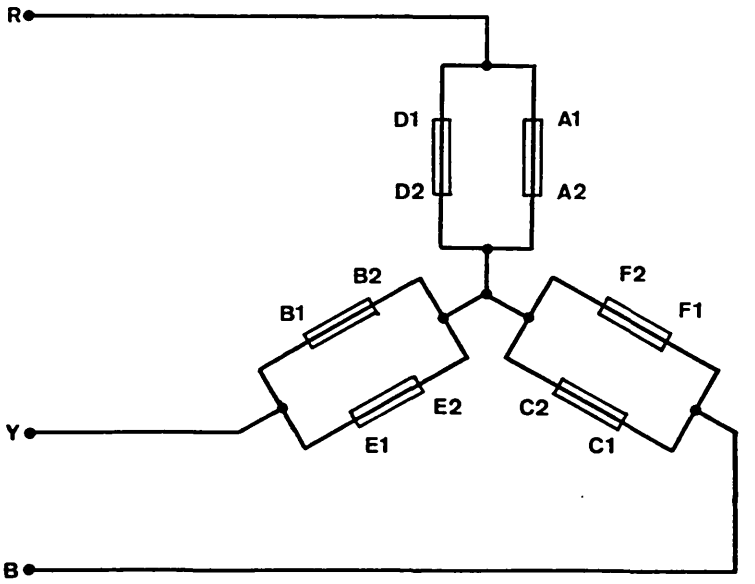
where

$$\bar{Z}_2 = 3 \; N_2^2 \; \bar{F}^{k2} \; \left|\bar{D}_{s2}^{k2}\right|^2 \; . \qquad (4.46)$$

Some thought was given to the way in which the two groups of windings were to be connected. Three possibilities existed: (i) Main and subharmonic sets in series; (ii) in parallel; or (iii) each set seperately excited. Each permutation is illustrated in Fig.4.7; the original machine was star connected. The main windings are marked A1-A2, B1-B2, C1-C2; the subharmonic phases are D1-D2, E1-E2 and F1-F2. It was decided to adopt the series connection for the prototype machine, in order to avoid the possibility of circulating currents. From Fig.4.7a, $\bar{I}=\bar{I}_1=\bar{I}_2$ and $\bar{V}=\bar{V}_1+\bar{V}_2$.

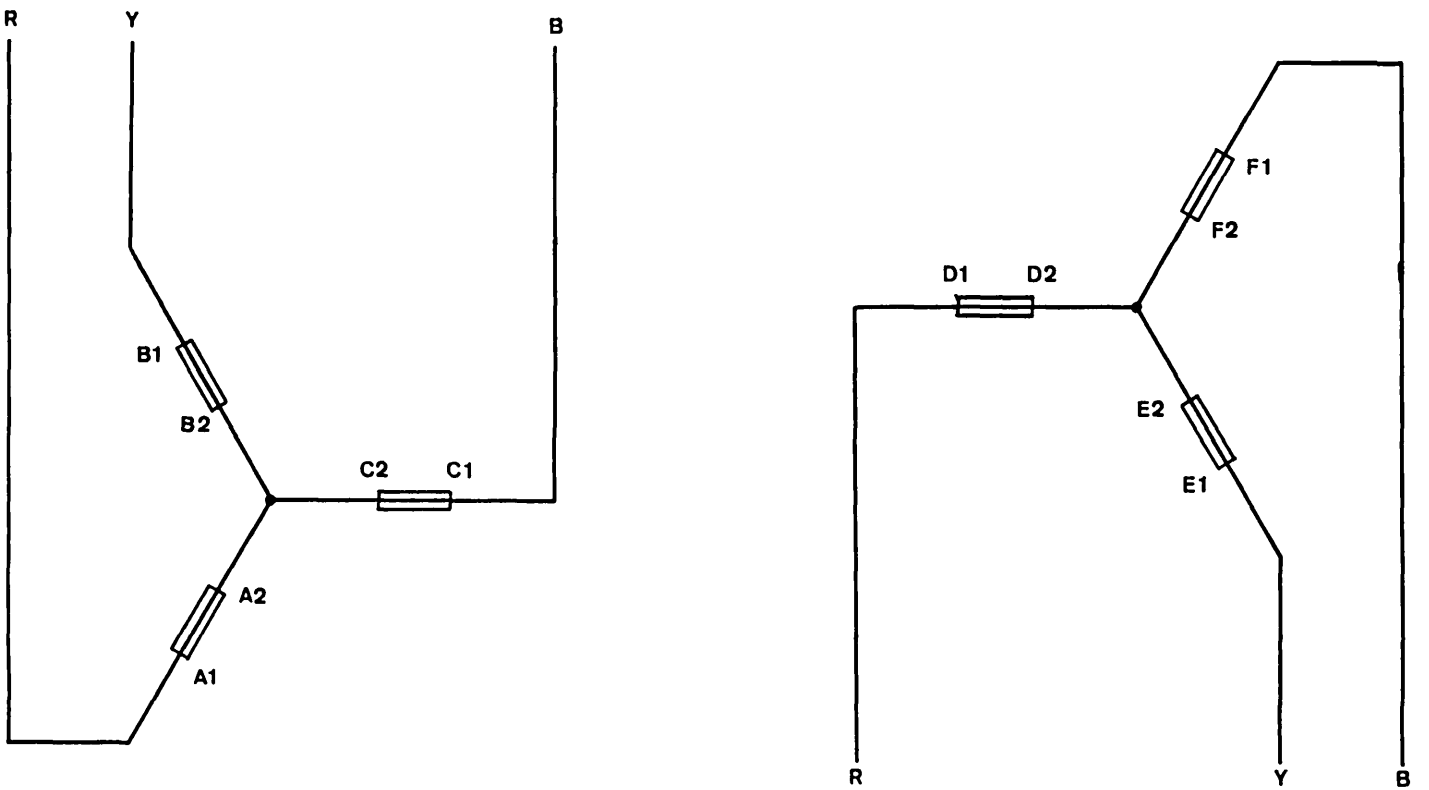


(a) Series



(b) Parallel

Fig.4.7: Main/subharmonic winding connections



(c) Seperately excited

The expressions for rotor loss (eqns.4.37) therefore become

$$P_r^{k1} = 9\, N_1^{\,2}\, s_{k1} \left|\bar{D}_{s1}^{k1}\right|^2 \left|\bar{I}\right|^2 \mathrm{Re}\,\{\bar{F}^{k1}\}\ ,$$

and (4.47)

$$P_r^{k2} = 9\, N_2^{\,2}\, s_{k2} \left|\bar{D}_{s2}^{k2}\right|^2 \left|\bar{I}\right|^2 \mathrm{Re}\,\{\bar{F}^{k2}\}\ ,$$

where

$$\bar{I} = \bar{V} \,/\, (\bar{Z}_1 + \bar{Z}_2)\ . \qquad (4.48)$$

Substitution into eqn.4.47 from 4.44, 4.46 and 4.48 illustrates the dependence of the individual harmonic losses on the principal and subharmonic numbers of turns per coil :

$$P_r^{k1} = \frac{\left|\bar{V}\right|^2 N_1^{\,2}\, s_{k1} \left|\bar{D}_{s1}^{k1}\right|^2 \mathrm{Re}\,\{\bar{F}^{k1}\}}{\left| N_1^{\,2} \left|\bar{D}_{s1}^{k1}\right|^2 \bar{F}^{k1} + N_2^{\,2} \left|\bar{D}_{s2}^{k2}\right|^2 \bar{F}^{k2} \right|^2}\ , \qquad (4.49)$$

and

$$P_r^{k2} = \frac{\left|\bar{V}\right|^2 N_2^{\,2}\, s_{k2} \left|\bar{D}_{s2}^{k2}\right|^2 \mathrm{Re}\,\{\bar{F}^{k2}\}}{\left| N_1^{\,2} \left|\bar{D}_{s1}^{k1}\right|^2 \bar{F}^{k1} + N_2^{\,2} \left|\bar{D}_{s2}^{k2}\right|^2 \bar{F}^{k2} \right|^2}\ . \qquad (4.50)$$

Enough information has now been presented to enable the complete design procedure to be formulated. It is summarised in step-by-step form below:

(i) The main analytical software described in Section 3.6 provides an estimate of the total rotor copper loss P_r. Basic design details similar to those given in Table 4.1 are used as input data, and, at this stage, only the principal harmonic is included in the computations.

(ii) For the desired percentage contribution from the

subharmonic field, the individual harmonic losses are given by eqn.4.6. The numbers of turns required in each coil in each winding are then calculated from eqns.4.46 and 4.47.

(iii) The nearest integer values of turns per coil are used to determine appropriate wire sizes, subject to standard filling-factor constraints. The method followed here is identical to that used by Bull in their winding design calculations.

(iv) The performance of the modified machine is then predicted, again using the main computer program. Two series-connected sets of windings are incorporated, using the conductor dimensions calculated above. The maximum number of harmonics is included, providing improved assessments of the effects of the subharmonic field.

(v) If required, the proportion of rotor losses supplied by the subharmonic field can be adjusted, and the steps from (ii) to (iv) repeated. Alternatively, the numbers of turns per coil can be varied slightly to achieve the desired result.

This procedure was carried out for the protoype machine. Predicted variations in the numbers of turns per coil are shown in Fig.4.8. The corresponding airgap power factor and input VArs to output watts ratio at each value of r have already been calculated, and were illustrated in Figs.4.2a and b. As can be seen from Fig.4.8, relatively large numbers of turns are required to achieve significant reductions in VAr demand. It was therefore decided to perform the experimental investigation at half rated terminal voltage, thus avoiding excessive saturation and large iron losses. At rated speed, the total rotor copper loss was calculated to be 95.3W for an applied phase voltage of 120V.

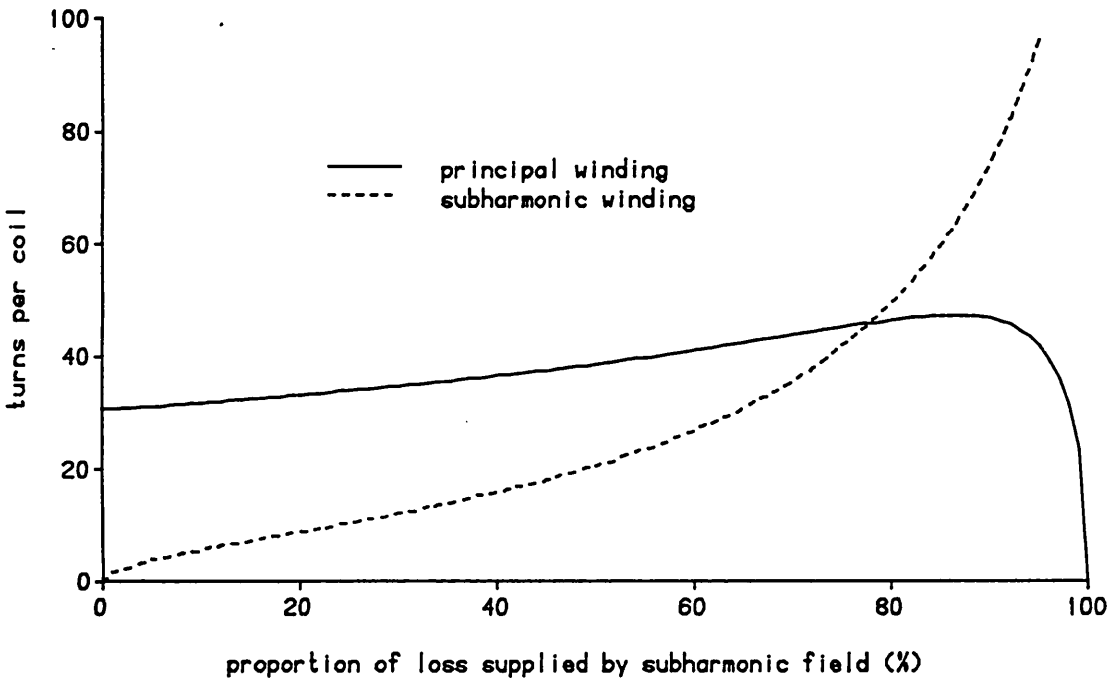


Fig.4.8: Winding design : numbers of turns per coil

It was eventually decided to supply 50% of the rotor losses from the subharmonic field. Although such a figure might well be considered prohibitively high in a commercial design due to the attendant derating, it was important to obtain a measurable effect on machine performance. Design calculations indicated that the numbers of turns per coil necessary to achieve the required division of losses were N_1=38.7 and N_2=20.7, although the actual figures specified for the modified windings were N_1=37 and N_2=20. The latter values were calculated using a design procedure which attempted to include the effects of stator winding resistances and leakage reactances to derive expressions for the **terminal** power factor, efficiency, and input VArs to output watts ratios. However, this was not very successful since the method assumed that the stator resistances and leakage reactances were proportional to the squares of the numbers of turns per coil. This assumption was subsequently found to be invalid, since the original and the rewound machine differed somewhat in the physical arrangement of the end-windings. It should be remembered that, in the original procedure derived above, the stator winding resistances and leakage reactances were neglected completely.

To satisfy Bull's usual filling factor constraints, each turn of each coil comprised two strands of 0.9mm nominal diameter insulated copper wire. The specified winding arrangement is shown in Table 4.3. Due to the uncertainties involved in estimating operating temperatures, rotor bar conductivity, stator end-winding leakage, etc., final performance prediction of the modified machine was deferred until the preliminary measurements on the original motor had been carried out; the calculations described above were made using approximate data supplied by Bull. Final predicted and experimental results are presented in Section 5.3.

Table 4.3: Modified winding configuration

slot number	1	2	3	4	5	6	7	8	9	10	11	12
winding 1 4-pole	A	A	A	A	$\bar{C}$	$\bar{C}$	$\bar{C}$	$\bar{C}$	B	B	B	B
winding 2 2-pole	D	D	D	D	D	D	D	D	$\bar{F}$	$\bar{F}$	$\bar{F}$	$\bar{F}$
slot number	13	14	15	16	17	18	19	20	21	22	23	24
winding 1 4-pole	$\bar{A}$	$\bar{A}$	$\bar{A}$	$\bar{A}$	C	C	C	C	$\bar{B}$	$\bar{B}$	$\bar{B}$	$\bar{B}$
winding 2 2-pole	$\bar{F}$	$\bar{F}$	$\bar{F}$	$\bar{F}$	E	E	E	E	E	E	E	E
slot number	25	26	27	28	29	30	31	32	33	34	35	36
winding 1 4-pole	A	A	A	A	$\bar{C}$	$\bar{C}$	$\bar{C}$	$\bar{C}$	B	B	B	B
winding 2 2-pole	$\bar{D}$	$\bar{D}$	$\bar{D}$	$\bar{D}$	$\bar{D}$	$\bar{D}$	$\bar{D}$	$\bar{D}$	F	F	F	F
slot number	37	38	39	40	41	42	43	44	45	46	47	48
winding 1 4-pole	$\bar{A}$	$\bar{A}$	$\bar{A}$	$\bar{A}$	C	C	C	C	$\bar{B}$	$\bar{B}$	$\bar{B}$	$\bar{B}$
winding 2 2-pole	F	F	F	F	$\bar{E}$	$\bar{E}$	$\bar{E}$	$\bar{E}$	$\bar{E}$	$\bar{E}$	$\bar{E}$	$\bar{E}$

Note: 4-pole (main) winding occupies bottom of slot, 2-pole (subharmonic) occupies top.

5. EXPERIMENTAL INVESTIGATION AND VERIFICATION

5.1 Scope of experimental work

As implied by the overall title above, the purpose of the practical work carried out in the project was two-fold: first, to verify experimentally the analysis of cage induction machines with inter-rings, and, secondly, to determine the degree of power-factor improvement obtained by the addition of the previously designed subharmonic winding.

The first of these objectives was fulfilled in part by a series of steady-state performance tests on the unmodified prototype machine, as manufactured by Bull. Measured values of torque, input power, supply current, etc., were compared with values predicted using the theory of Section 3. The ability of the analysis to take inter-rings into account was further confirmed by an investigation of airgap flux density. The test procedures adopted and the experimental results obtained are given in Section 5.2.

The performance tests carried out on the unmodified machine also proved useful in studying the VAr-reducing effects of the subharmonic field. By comparing measurements of power factor, efficiency, and input VArs to output watts made before and after the prototype machine had been rewound to the specification of Section 4.3, it was possible to assess the feasibility of the subharmonic-field method of power-factor improvement, thus fulfilling the second objective outlined above. This part of the work is described in Section 5.3.

5.2 Verification of Inter-ring Analysis

Prior to the main tests, the original machine was partially dismantled in order to examine the construction. An accurate check on the leading dimensions showed that the values listed in Table 4.2 were substantially correct. Using a vernier protractor, the angle of rotor skew was found to be 6.4 degrees.

As far as the construction itself was concerned, the copper braze which formed the inter-ring had not only filled the slot machined for that purpose (see Fig.3.2), but had also penetrated the core between the laminations on either side. It was impossible to ascertain the extent of the penetration, but the width of the inter-ring had effectively been increased, and its resistance distributed along the axial length of the core. An attempt was made to include these effects in the model by increasing the number of bands in the machine from two to four, as shown in Fig.5.1. As far as the distributed nature of the bar-to-bar conductor is concerned, current in the inter-ring is constrained to flow in three distinct paths, each of which is considered to be of zero width - the 'point conductor' approximation. The middle of these three paths carries more current than the other two, however, since it possesses a larger cross-sectional area. This is reflected in the model by choosing suitably scaled values for the inter-ring impedances of Fig.5.1.

Further inspection of the rotor revealed several large voids in the surface of the brazing material used for the inter-ring. As a result, the cross-sectional area was visibly reduced and the resistance increased. This was somewhat simpler to take into account, since the inter-ring

resistance, originally calculated on the basis of uniform current distribution over the slot cross section depicted in Fig.3.2, was an input variable and could be altered as desired.

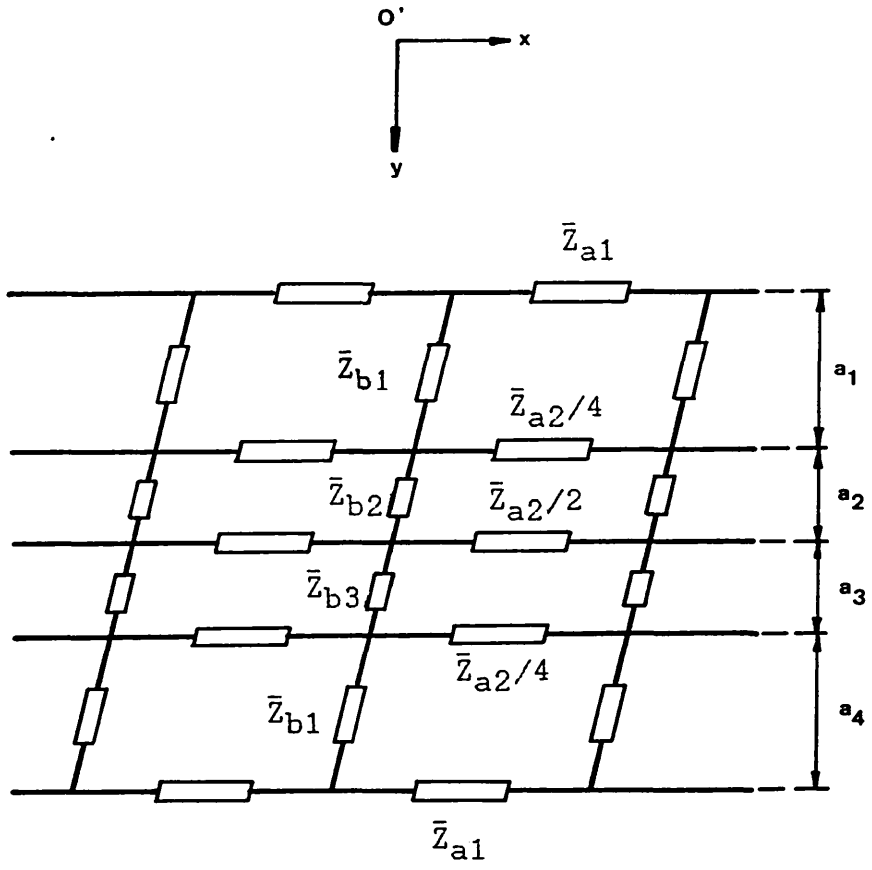


Fig.5.1: Modified loop model

5.2.1 Test Procedure

For the rotating tests, the prototype motor was coupled to a seperately-excited DC generator via a rotating torque transducer, as shown in Fig.5.2. A three-phase variac provided a variable-voltage supply for the test motor; two of the three input line voltages were monitored using digital voltmeters, and the average value recorded. A digital ammeter and a moving-coil wattmeter were switched between the three phases to obtain measurements of mean current and total input power.

The contactless torque transducer provided direct digital readouts of speed and torque, correct to a high degree of accuracy. The effects of friction and windage were taken into account in the normal way by taking the difference between the torque reading with the motor energised and that with it de-energised, at each load point. Unfortunately it was not possible to determine the frictional torque over the full speed range, since the DC generator was not capable of motoring at speeds greater than 1100 rpm without severe field-weakening making it unstable. In practice, however, the loss torque was found to remain constant at -0.22 Nm for speeds between 300 and 1100 rpm, and it was therefore considered acceptable to subtract this figure from each torque reading, irrespective of speed. The results presented in the following sections relate to the electromagnetic torque developed internally in the test motor, rather than to that available at the shaft.

Due to the speed limitation of the DC machine, it was necessary to adopt one of two different procedures to obtain stable operation at each load point. For speeds up to 1250 rpm, the load machine was started by exciting it with rated

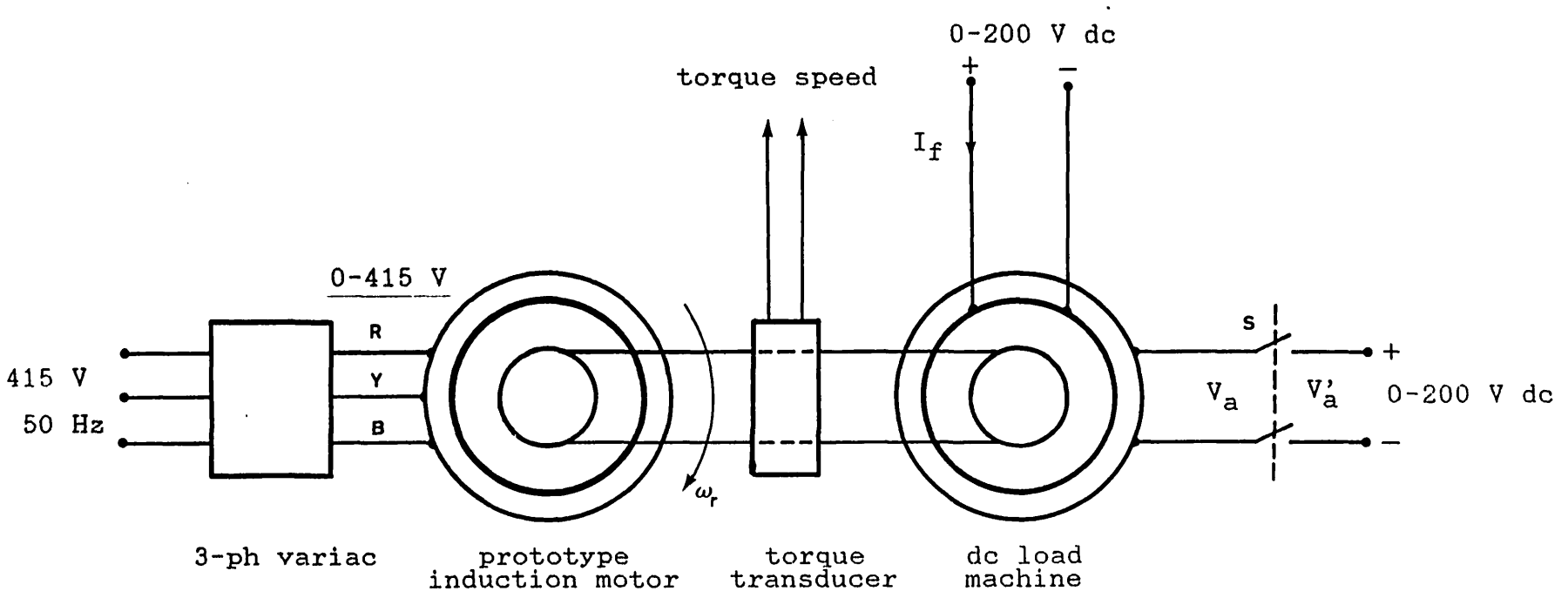


Fig.5.2: Test schematic

field current and increasing the armature voltage (V_a in Fig.5.2) from zero. At approximately the desired speed, power was supplied to the induction machine by switching on the three-phase variac and setting the required line voltage. Further speed adjustment was carried out by varying the field current as required. For speeds above 1250 rpm, the induction motor was started first using the variac from its zero setting upwards, ensuring that the armature circuit was open circuited, and the field current zero. At approximately synchronous speed, the field current was adjusted until the open-circuit armature voltage V_a became equal to the supply voltage V_a'. The switch S was then closed and the field current increased until the speed fell to the required value.

It was decided to perform all measurements at constant temperature, in order to avoid the uncertainties involved in re-calculating conductivities at each load point. An electronic temperature probe was inserted into the stator end-windings, giving a direct reading in degrees C. Preliminary tests indicated that a stable end-winding temperature of 65°C was attained at full-load speed. This figure was maintained over as wide a speed range as possible with the help of the seperately-excited cooling fan, fitted as standard by Bull. At low speeds, however, it was nonetheless necessary to perform some tests at reduced voltage, in order to avoid overheating. A Kelvin Bridge was used to measure the following stator-winding resistances:

$$\left.\begin{aligned} R_{s1} &= 1.29\Omega \\ R_{s2} &= 1.21\Omega \\ R_{s3} &= 1.26\Omega \end{aligned}\right\} \quad \text{mean} = 1.25\Omega \quad \text{at } 65^\circ C$$

All other relevant parameters (e.g., stator end-winding leakage reactance, rotor bar conductivity, etc.) were taken from data supplied by Bull, as listed in Table 4.2.

5.2.2 Performance Tests

Measured and predicted variations in torque, input power and current with speed are compared in Figs.5.3-5.5. In general, the correlation between theory and practice is fair, although predicted values of torque are a little high, and those of input power a little low.

It is the belief of the author that the calculations involving the various iron portions of the magnetic circuit form the weakest part of the analysis. The assessment of iron losses is particularly crude, relying on the assumption that only the principal harmonic component of flux is present in the teeth and back-iron, neglecting high-frequency effects entirely. As discussed in section 3.1, no iron loss-producing mechanism is included in the model itself; the phenomenon is treated purely as a parasitic effect, since no compensation of the coupling impedances is employed. In a balanced machine, this deficiency may be remedied to a certain extent by imagining equivalent core-loss resistances to be connected directly across the machine terminals, thus modifying the effective coupling impedances and dissipating the required loss. This procedure is similar to that adopted in the conventional equivalent-circuit method, and it produces the same results: an increase in input current and power, but no reduction in torque. For more accuracy, the iron-loss resistance can be connected across the magnetising branch of the phase equivalent circuit, thus decreasing the torque. In this case, however, the presence of the inter-ring complicates a comparable extension to the basic method.

The inadequate assessment of iron losses is, however, only partially responsible for the discrepancies observed in

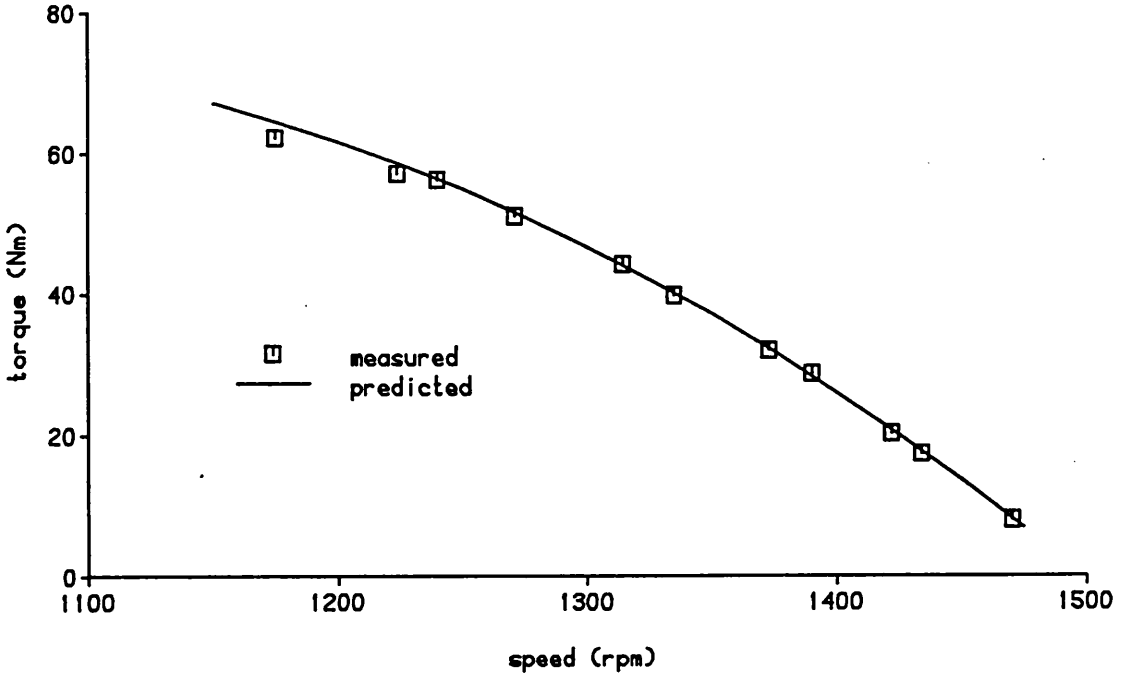


Fig.5.3a: Torque-speed characteristic : full voltage

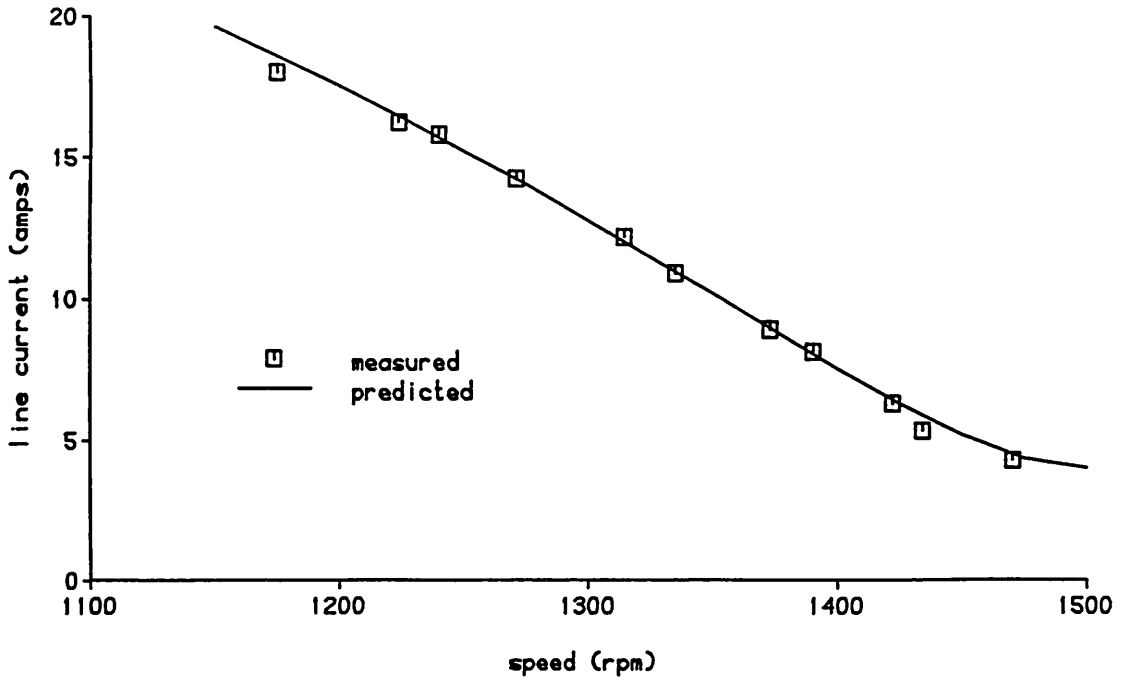


Fig.5.3b: Current-speed characteristic : full voltage

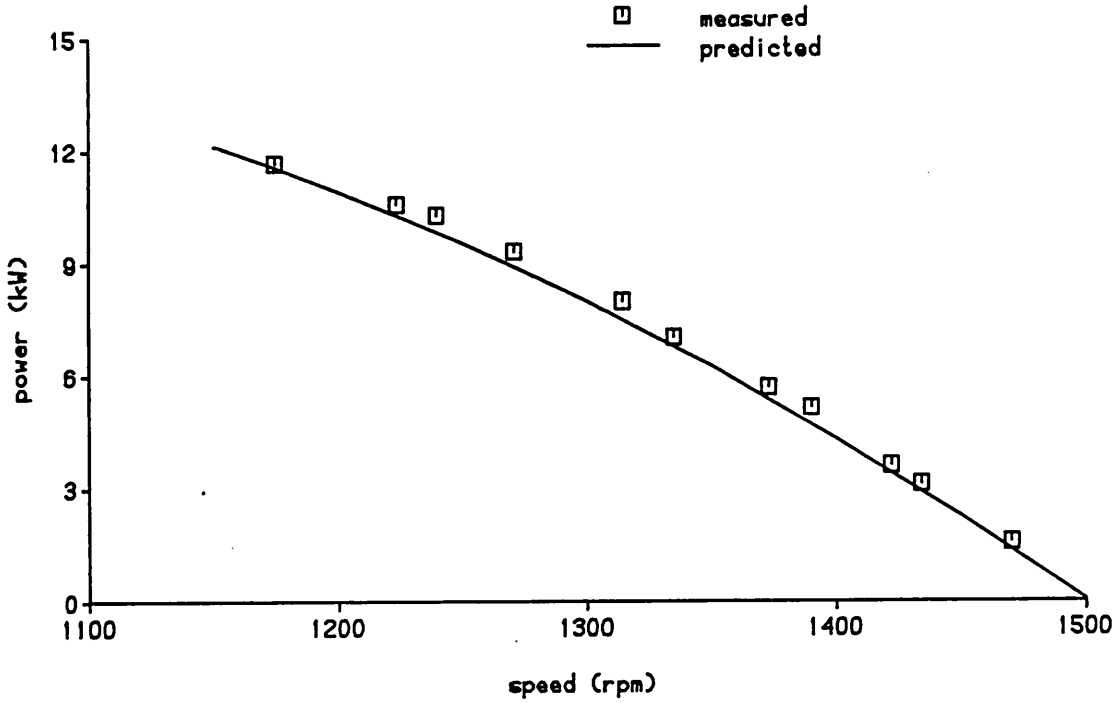


Fig.5.3c: Input power-speed characteristic : full voltage

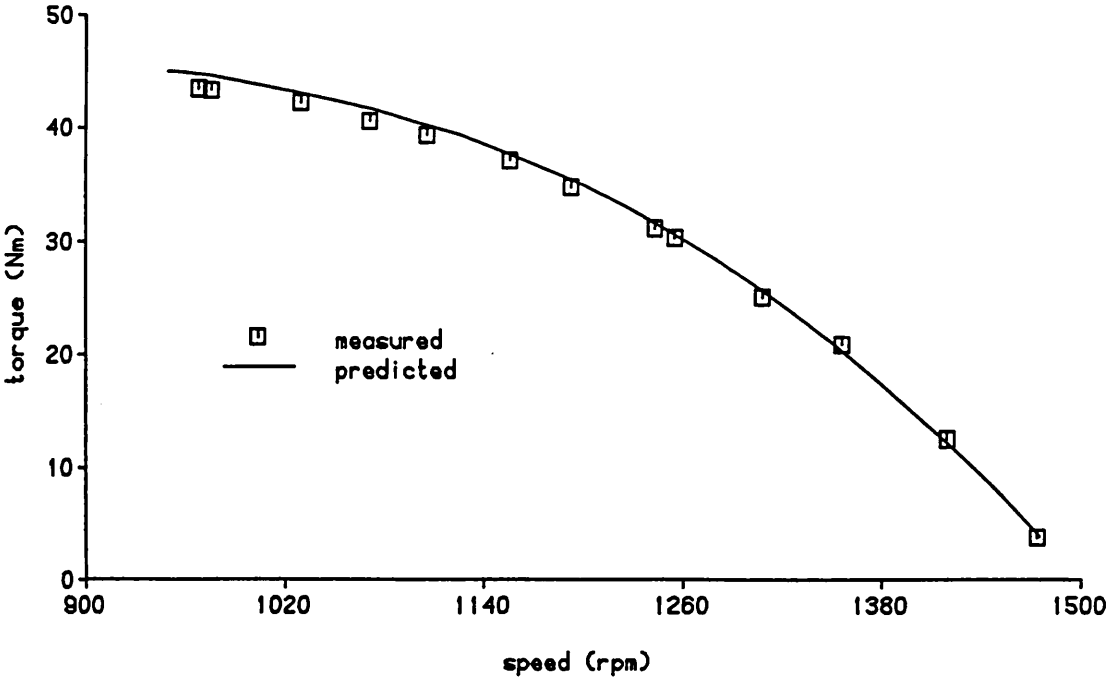


Fig.5.4a: Torque-speed characteristic : three-quarters voltage

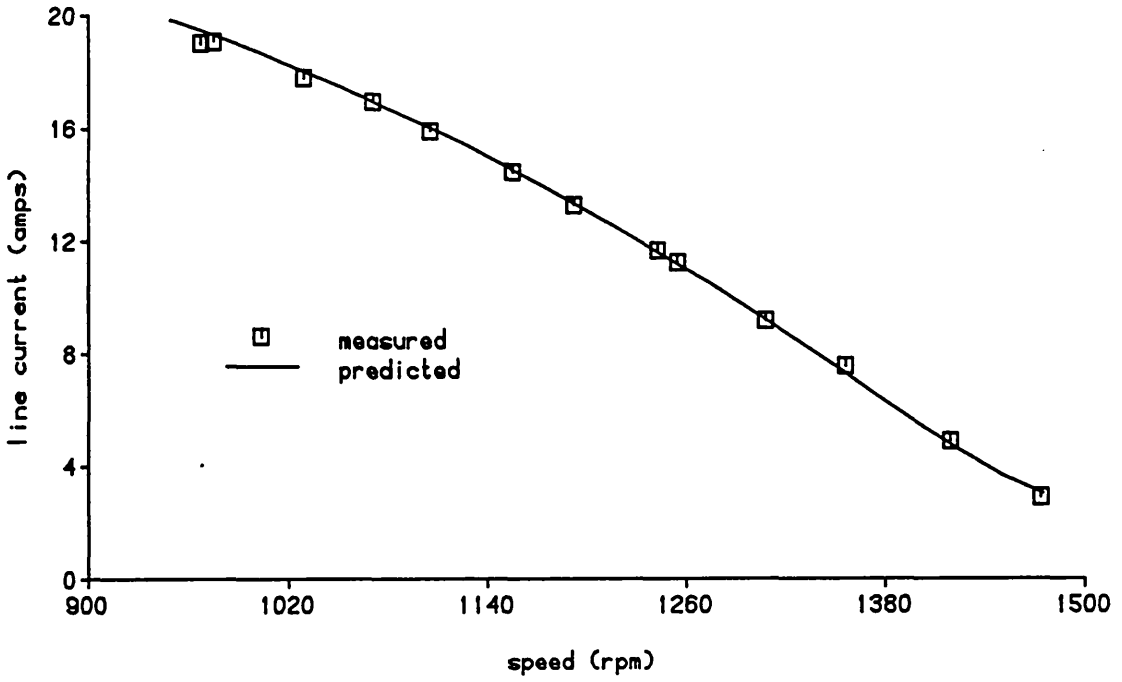


Fig.5.4b: Current-speed characteristic : three-quarters voltage

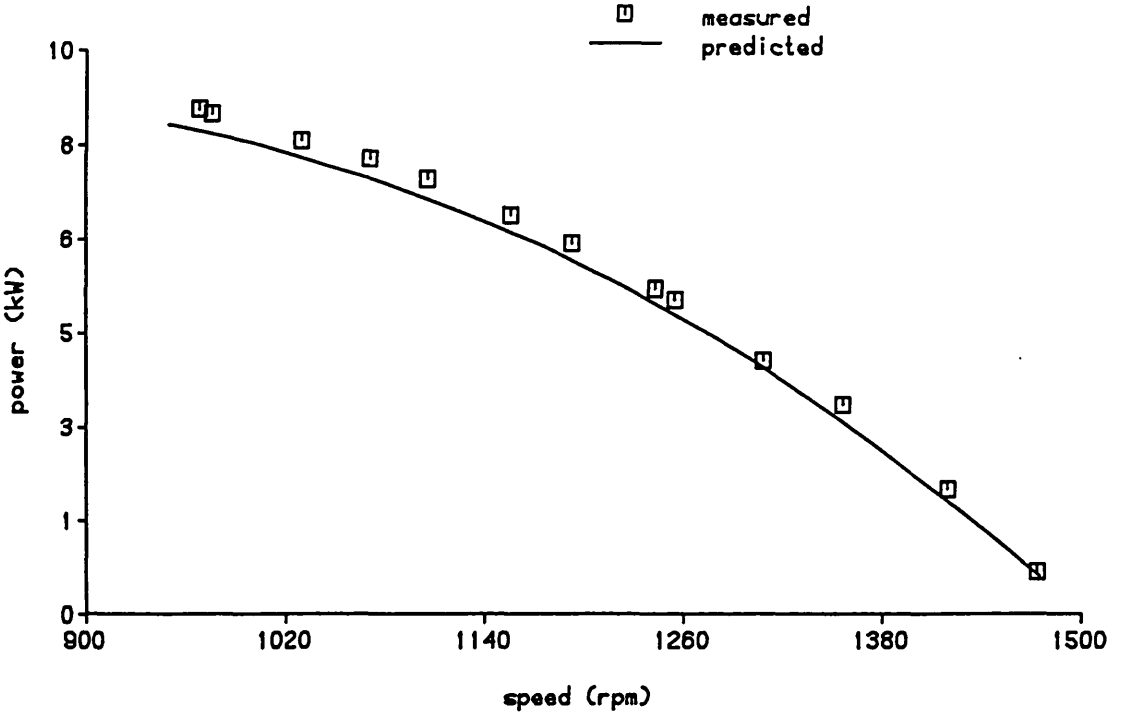


Fig.5.4c: Input power-speed characteristic : three-quarters voltage

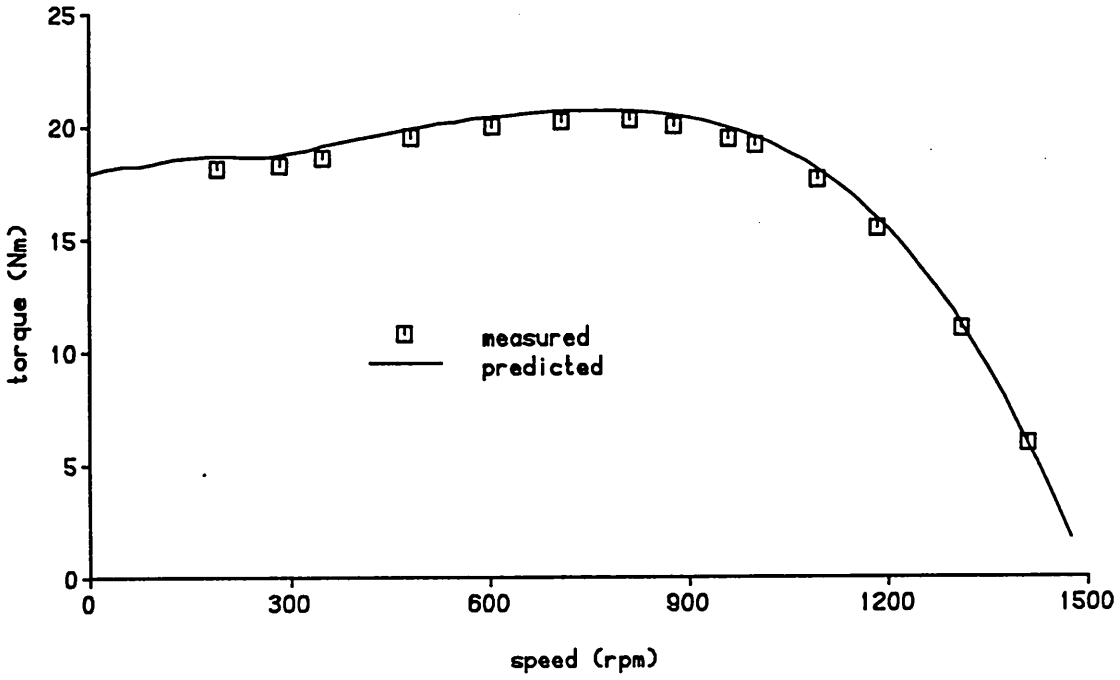


Fig.5.5a: Torque-speed characteristic : half voltage

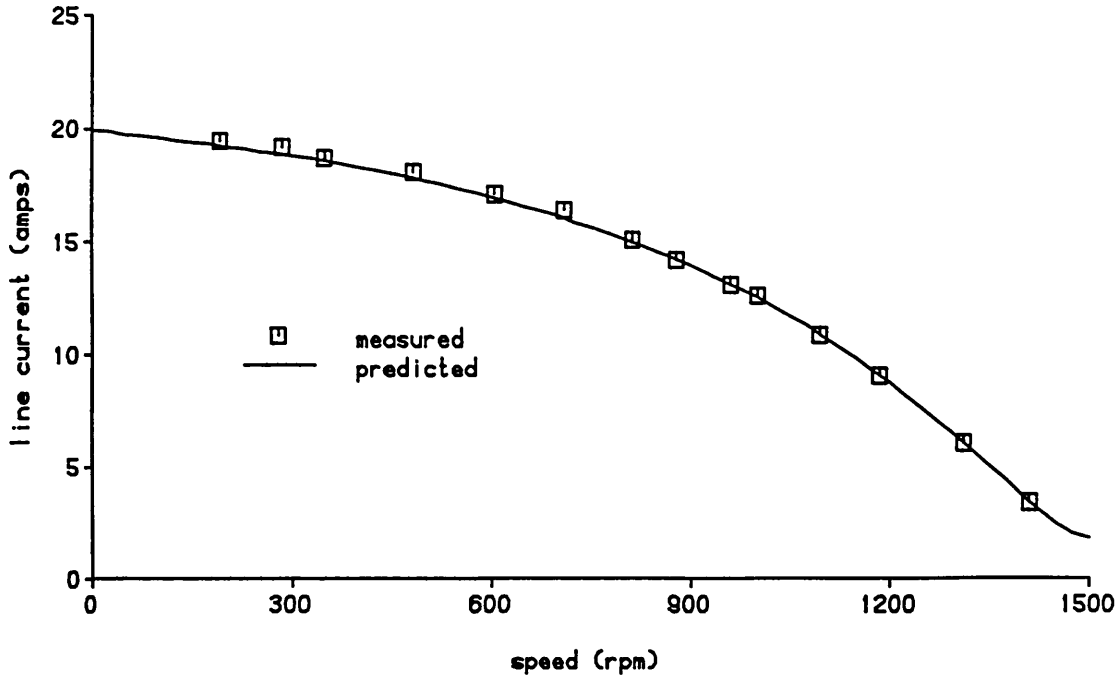


Fig.5.5b: Current-speed characteristic : half voltage

Figs.5.3-5.5. A considerable amount of uncertainty surrounds the calculation of the external leakage impedances. In short-core machines such as the one under investigation in this project, the role played by the stator end-turn leakage fields is exaggerated by the physical size of the winding overhang. The same is true of the rotor end-ring leakage reactances, since the bars extend over a considerable distance beyond the ends of the core. As a result, accurate figures for stator and rotor leakage reactances are difficult to determine. Inter-ring resistance is almost impossible to calculate with any confidence, due to the aforementioned voids in the copper braze. A value of inter-ring resistivity 50% higher than that used for the copper bars was considered suitable; the inter-ring leakage reactance was neglected entirely.

In the light of previous discussion, it is apparent that further verification of the inter-ring analysis is required. This is provided by the study of airgap flux density described in the following section.

5.2.3 Search-coil verification

Slot skew is an established method of reducing cogging effects and parasitic torques in induction motors [18,20,23]. In theory, the EMFs induced in the rotor cage by a particular harmonic component of airgap flux may be eliminated by the choosing the circumferential skew to be equal to the desired wavelength. Many machine designers specify a skew of one slot pitch to minimise the effects of those space harmonics introduced by the slotting, although it has been shown [24, 20] that such phenomena can be

reduced by winding design and by careful choice of the numbers of stator and rotor slots. In most well-designed machines, therefore, the effect of skew on the steady-state torque-speed characteristic is generally small, the only difference being a reduction in the starting and pull-out torques [25].

The same is not true, however, of the axial variation in airgap flux density produced by the change in phase difference between the stator- and rotor-driven MMF waves. Several experimental and theoretical studies [16,21,26] have shown these variations to be significant. Since it is the same shift in phase which is responsible for the circumferential bar-to-bar currents flowing along the low impedance path provided by the inter-ring, it seemed logical to expect that the inclusion of inter-rings had a measurable effect on the axial flux distribution. It was therefore decided to undertake a study of airgap flux density as further verification of the inter-ring analysis. Several sets of search coils were affixed to the airgap surface of the stator, and the magnitude and phase of the EMFs induced in them by the travelling flux waves were measured and compared with values predicted using expressions derived in Section 3.5.

The search coils themselves had to be large enough to yield measurable signals, yet small enough to obtain a reasonably accurate assessment of the axial flux distribution. Preliminary calculations indicated that 8x8 mm coils were suitable; each was constructed from a single turn of 0.25mm diameter enamelled copper wire wound around a wooden former. The trailing leads were twisted tightly together to avoid spurious pick-up, and were taken, via a multipole connector and switch, to an oscilloscope and spectrum

analyser.

In all, six sets of search coils were distributed around the inner periphery of the stator. In this way it was possible to observe the effects of the harmonics introduced by the step distributions of stator MMF. To obtain an idea of the flux variation in the region of the inter-ring itself, two of the six sets included a single coil placed directly opposite the inter-ring. Each of the remaining four sets comprised eight coils, arranged as indicated in Fig.5.6, which also shows the circumferential position of each set relative to the main stator windings.

The spectrum analyser displayed the harmonic content of the induced EMF directly, separating the line-frequency component from the slot harmonics without the need for a seperate low-pass filter. As discussed in Section 3.3.2, the slot ripple at the stator is not included in the present analysis, so only the 50Hz component of search-coil EMF was used for verification purposes. RMS readings of amplitude were taken for each coil at various speeds and excitation levels; phase measurements were similarly obtained using the applied red phase (winding number m=1) terminal voltage as reference.

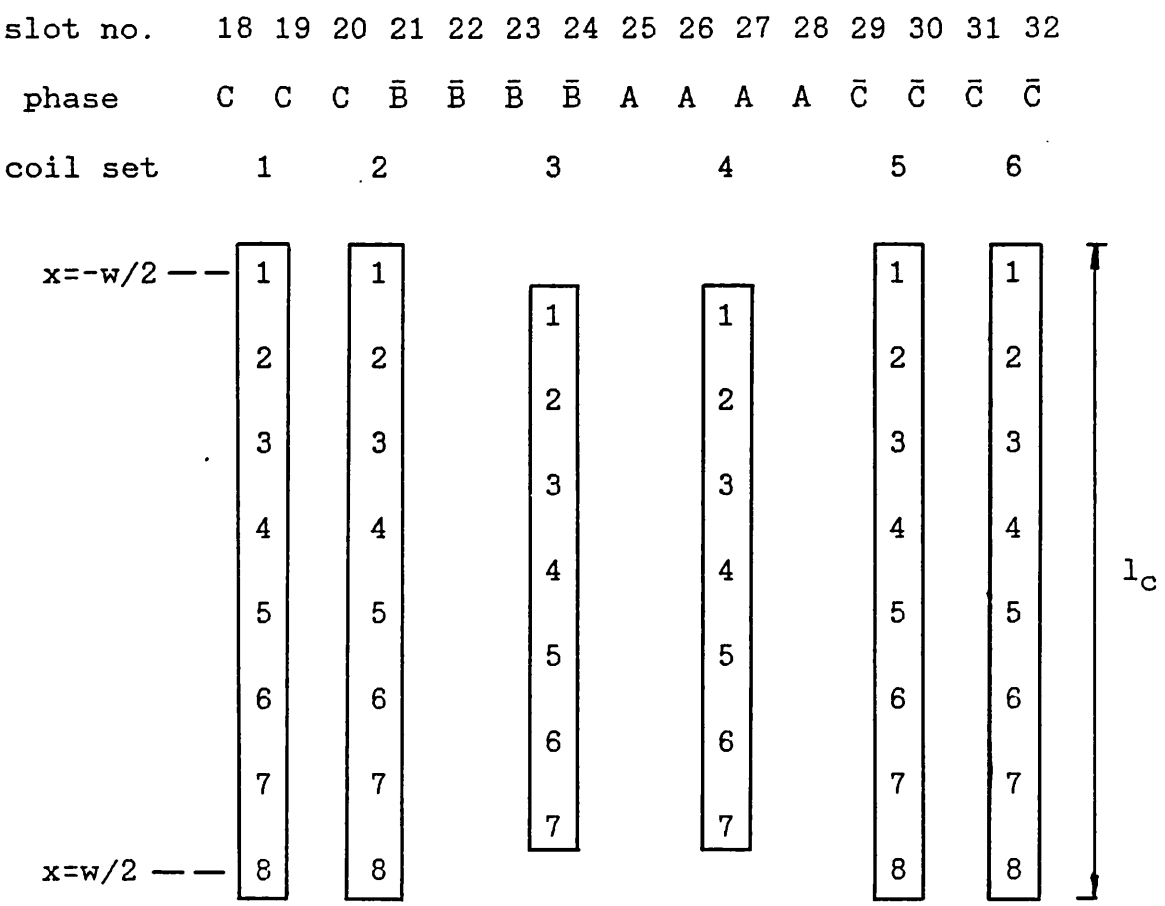
Measured and predicted distributions of induced EMF are compared in Figs.5.8-5.15. Coils 1 and 8 in sets 1,2,5 and 6 protruded beyond the ends of the stator core, rendering the prediction of induced EMF for all eight coils impractical. Complete sets of measured values are nevertheless included in order to illustrate fringing effects at the ends of the core. As before, reduced voltages were applied to maintain end-winding temperatures at 65°C for the duration of the low-speed tests.

The results obtained under no-load conditions can be

used to verify the axial distribution of stator-driven flux. Fig.5.8a demonstrates a noticeable drop in gap density in the immediate vicinity of the inter-ring. However, the increment in airgap length necessary to predict such a change was much less than might at first be imagined from a cursory examination of the inter-ring slot dimensions (see Fig.3.2). As mentioned in Section 3.2, the assumption of a piecewise-constant airgap length implies a step variation in flux density at band boundaries. Fringing in the axial direction serves to lessen the abruptness of such a change, however, thus reducing the component of flux which passes normally through the bottom of the slot forming the inter-ring. For the purposes of this study, it was considered sufficient to model the effect by drastically reducing the effective depth of the ring. The predictions presented in this and the previous section were made on the basis of the following band details (refer also to Fig.5.1):

a_1 = 33.5 mm ; x_1 = -20.75 mm ; g_1 = 0.65 mm ;
a_2 = 4.0 mm ; x_2 = -2.00 mm ; g_2 = 2.00 mm ;
a_3 = 4.0 mm ; x_3 = -2.00 mm ; g_3 = 2.00 mm ;
a_4 = 33.5 mm ; x_4 = -20.75 mm ; g_4 = 0.65 mm .

Further inspection of Fig.5.8a reveals that the predicted magnitudes of induced EMF are generally smaller than their measured counterparts. As stated in Section 3.1, harmonic effects resulting from the slotting of stator and rotor are ignored. In reality, however, a greater proportion of airgap flux passes through the tooth-tips than the assumption of smooth airgap surfaces suggests. In this investigation, each search coil spanned slightly less than a single stator tooth-tip. As a result, relatively low magnitudes of predicted EMF are not particularly surprising.



sets 3,4 (pattern A)		sets 1,2,5,6 (pattern B)	
coil number	axial position (mm)	coil number	axial position (mm)
1	-33	1	-35
2	-22	2	-25
3	-11	3	-15
4	0	4	-5
5	11	5	5
6	22	6	15
7	33	7	25
		8	35

Fig.5.6: Search coil positions

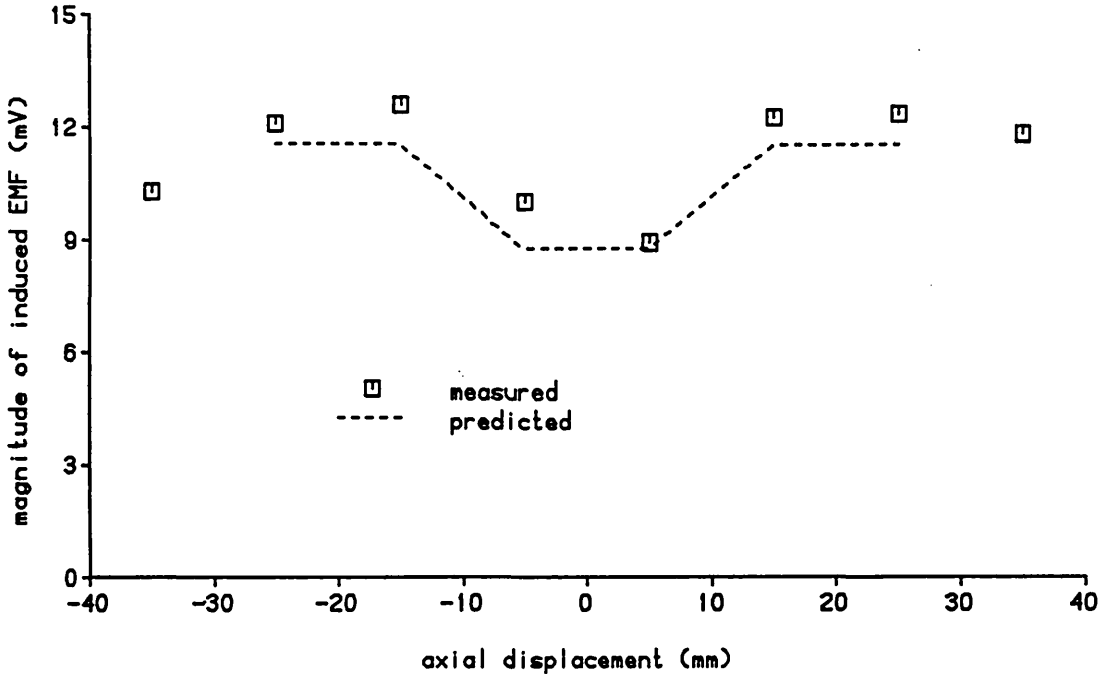


Fig.5.8a: Search coil EMF : set 1 : magnitude

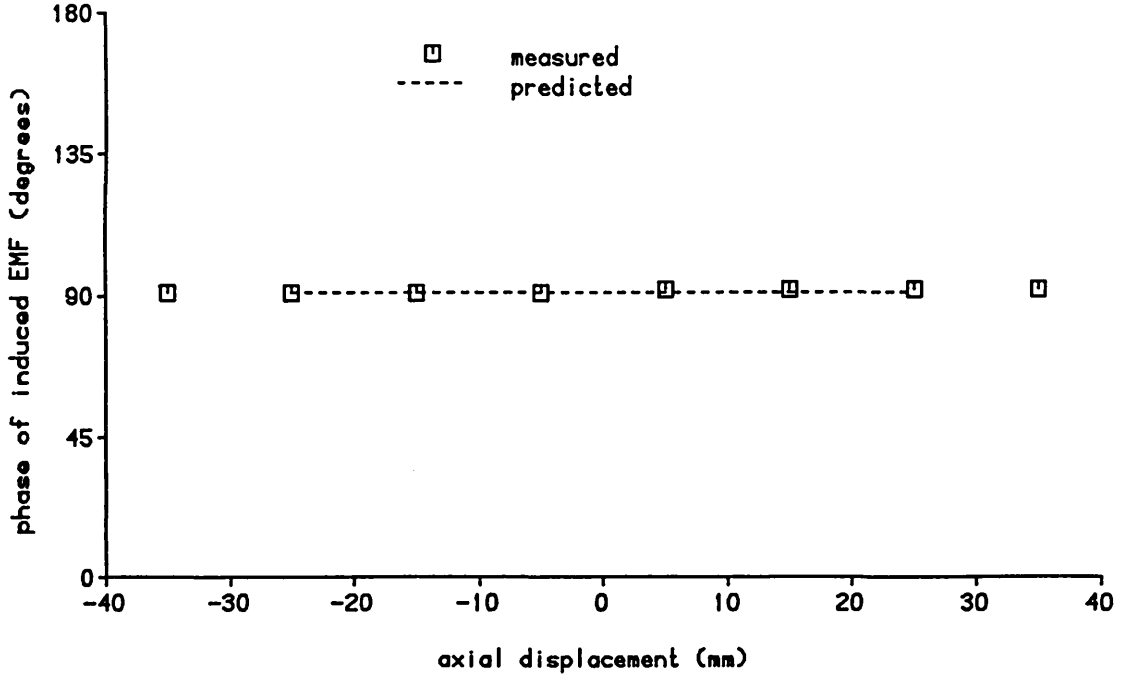


Fig.5.8b: Search coil EMF : set 1 : phase

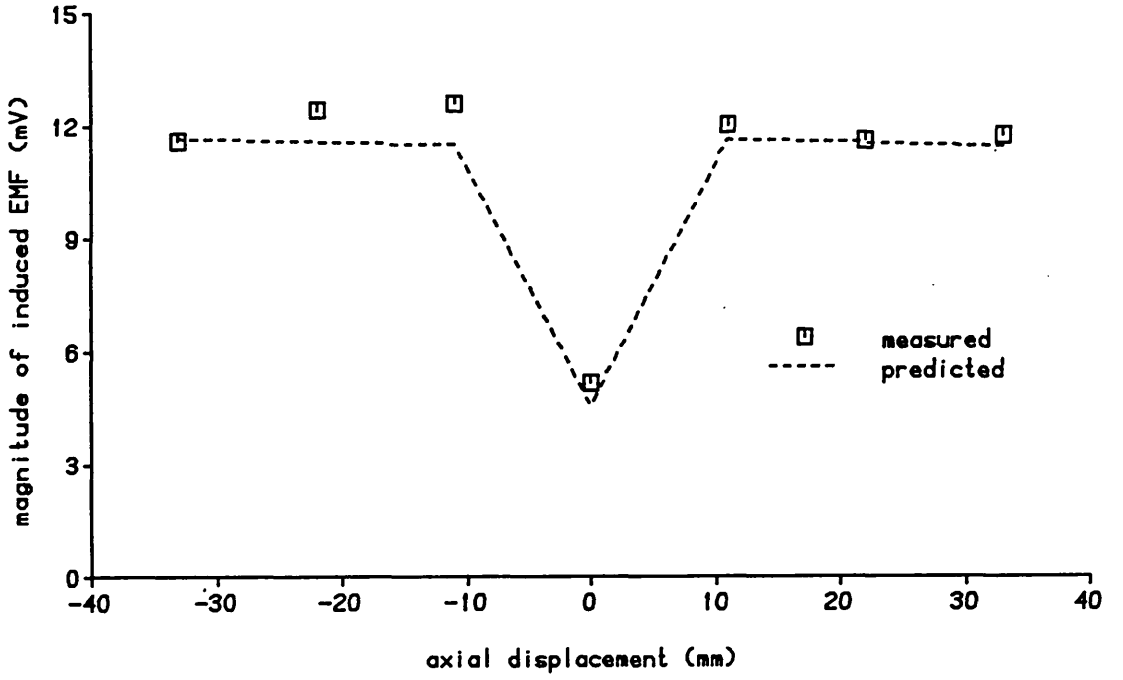


Fig.5.9a: Search coil EMF : set 3 : magnitude

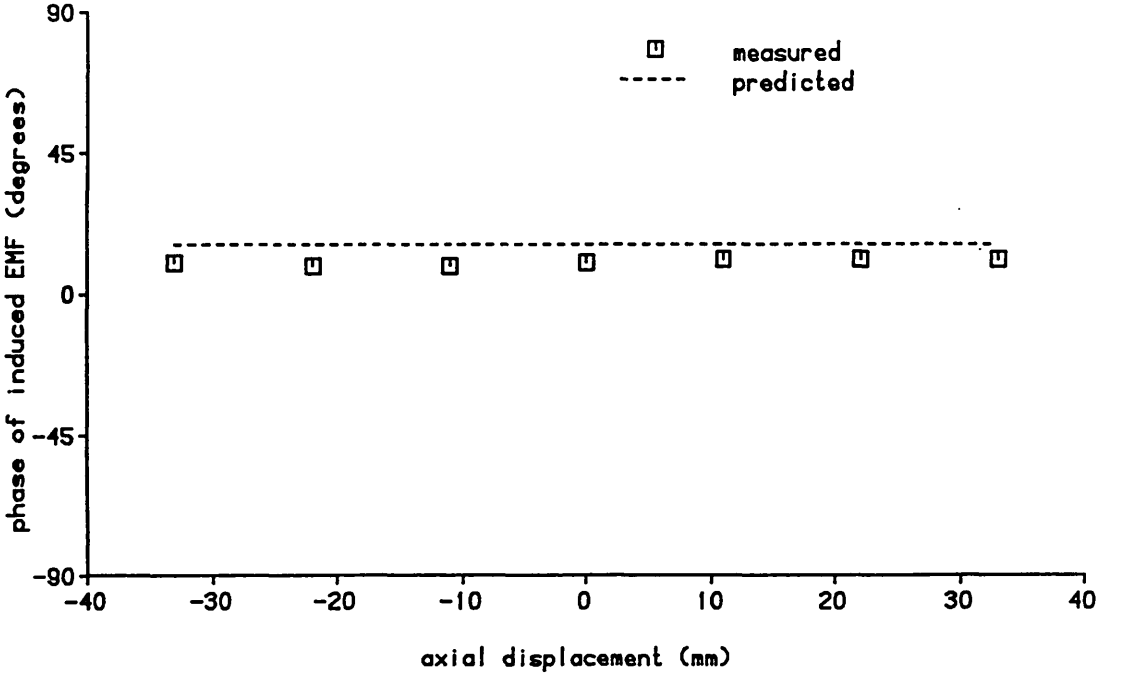


Fig.5.9b: Search coil EMF : set 3 : phase

One final feature displayed by Fig.5.8a deserves comment. After the search-coil results had been obtained, and while the machine was being removed from the test rig prior to rewinding, it was noticed that very little effort was required to move the shaft in the axial direction by some three to four millimetres. While aligning the torque transducer, it had been necessary to apply a considerable force to the end of the rotor. Presumably this had dislodged the shaft bearings from the stator end-housings, resulting in axial misalignment of the rotor and stator cores. From the diagram of Fig.5.16 it is possible to see how the distribution illustrated in Fig.5.8a could have arisen, since the flux linking coil 4 is increased, while that linking coils 1 and 5 is reduced.

Figs.5.10 and 5.11 illustrate the axial distribution of coil EMF for sets 2 and 4 at rated voltage and speed. The effect of skew is starting to become evident, since both magnitude and phase variations are essentially rotated versions of the corresponding distributions obtained at synchronous speed.

At 750 rpm, the effect of the inter-ring is more marked. Figs.5.12 and 5.13 compare the measured and predicted variations for sets 3 and 5 at half rated voltage. The correlation between theory and practice is thought to be acceptable, bearing in mind the difficulties involved in accurately positioning each coil. Verification is further provided by the third curve included in Figs.5.12 and 5.13, which represents the predicted EMF distribution for a machine from which the inter-ring has been removed, but which is otherwise identical to the test motor used for the experimental results.

As an approximation to the conditions at starting,

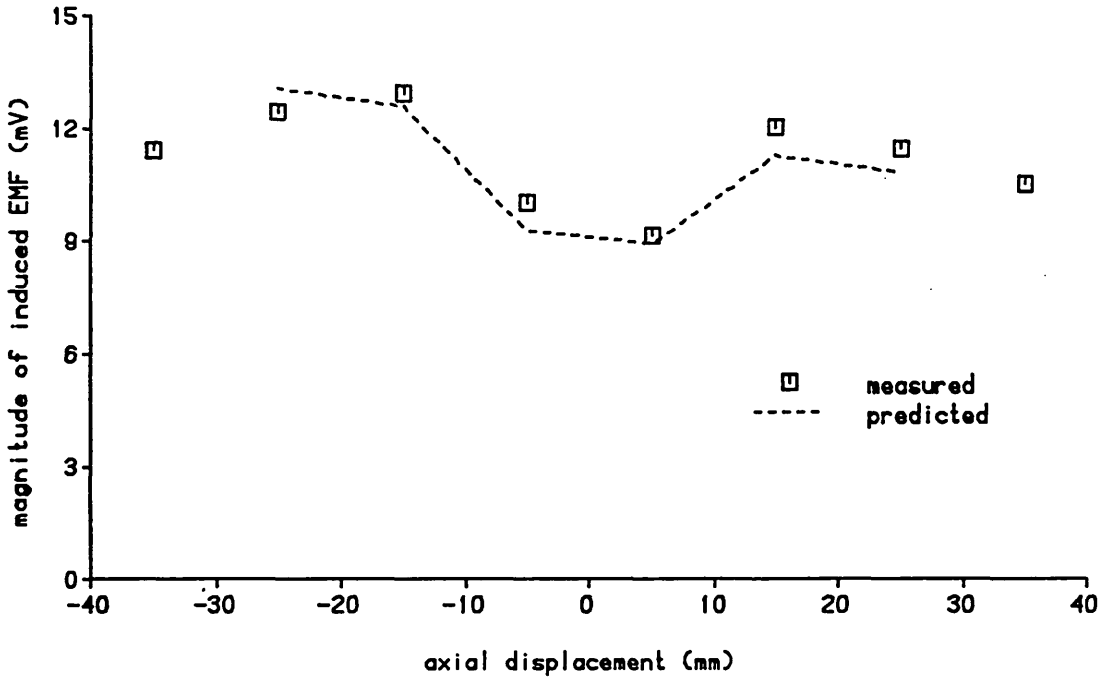


Fig.5.10a: Search coil EMF : set 2 : magnitude

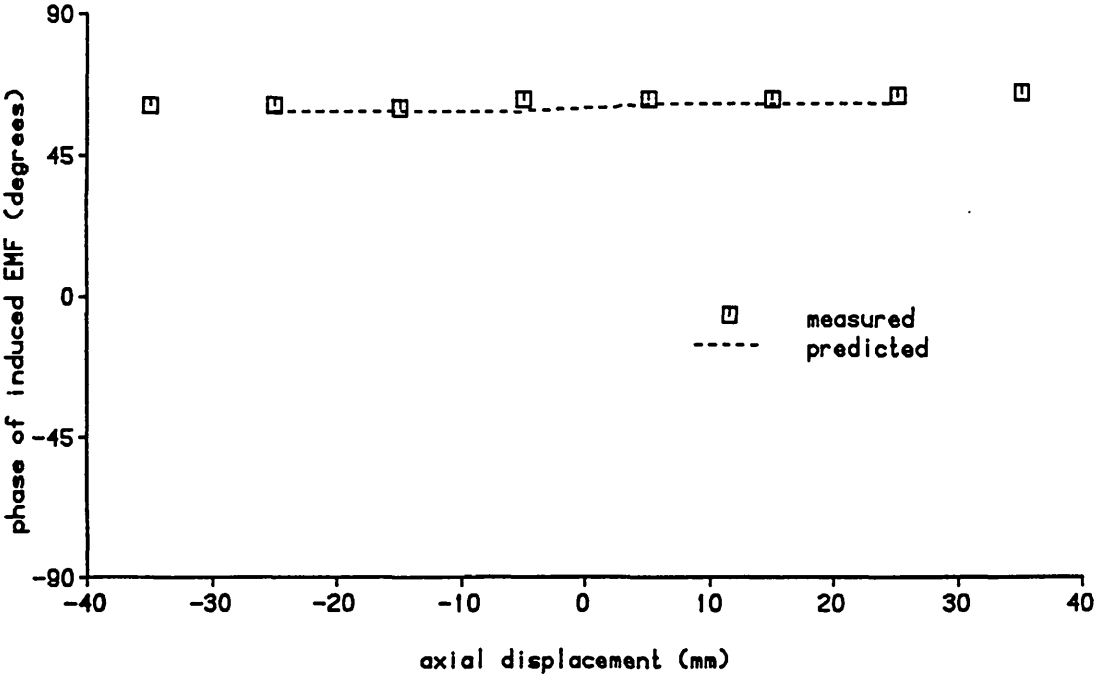


Fig.5.10b: Search coil EMF : set 2 : phase

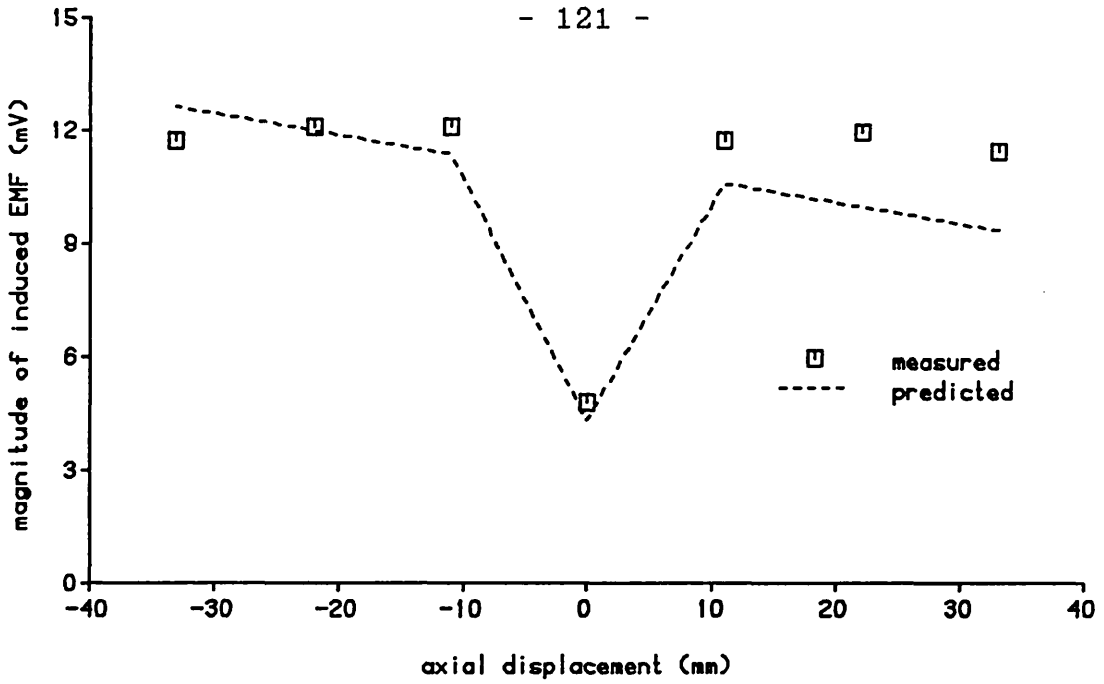


Fig.5.11a: Search coil EMF : set 4 : magnitude

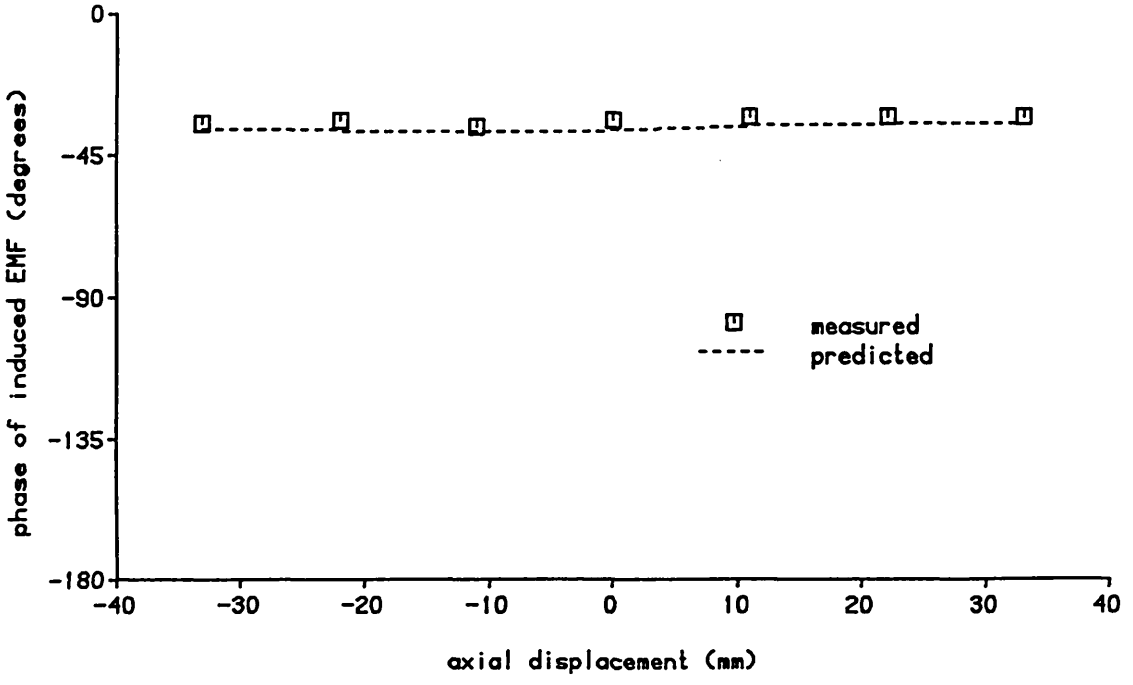


Fig.5.11b: Search coil EMF : set 4 : phase

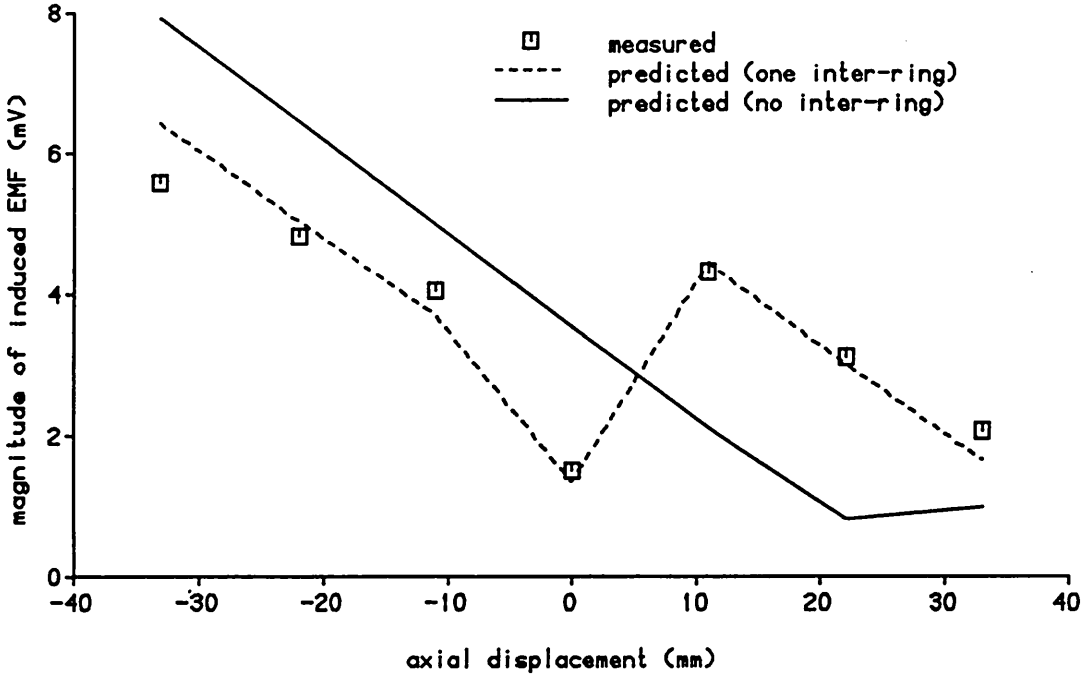


Fig.5.12a: Search coil EMF : set 3 : magnitude

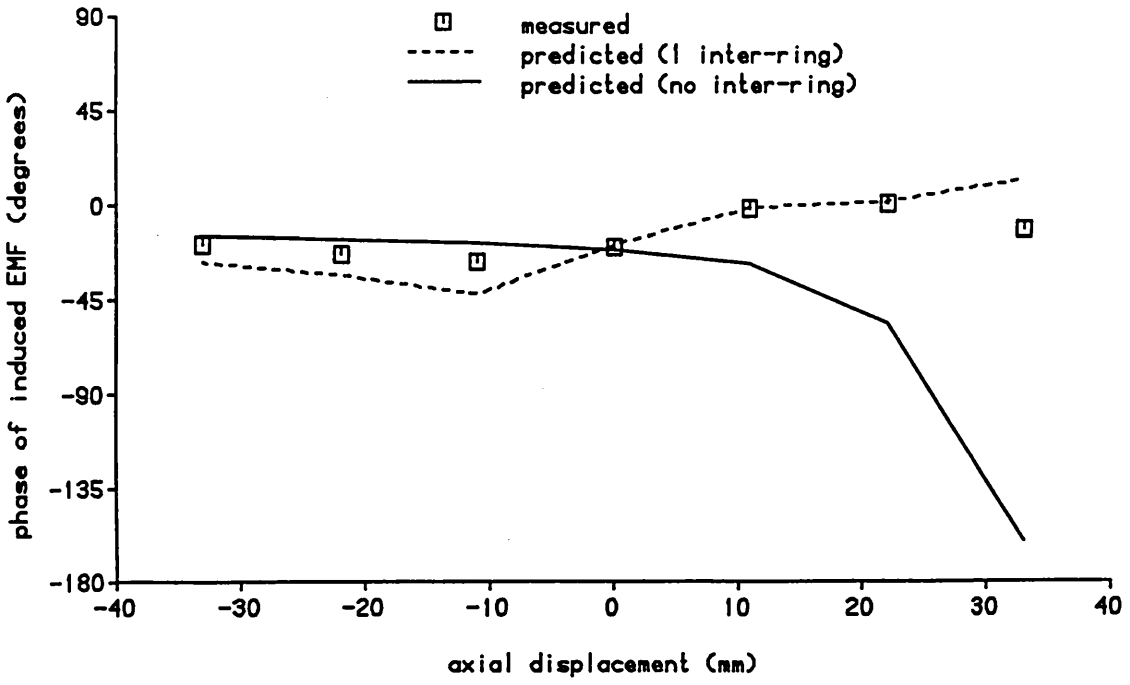


Fig.5.12b: Search coil EMF : set 3 : phase

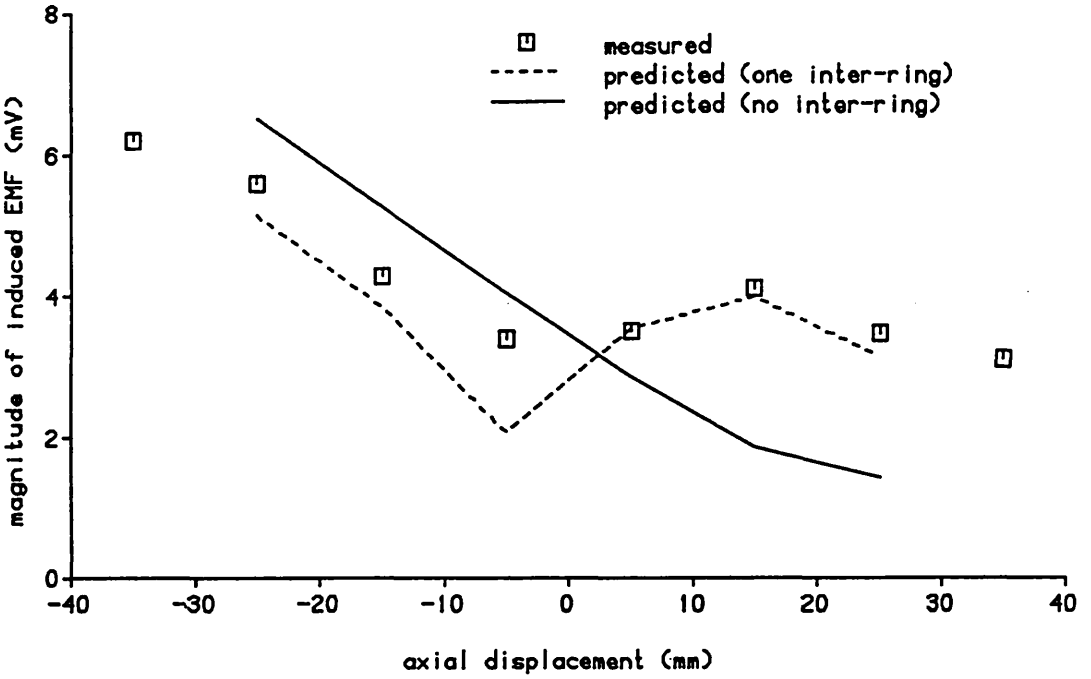


Fig.5.13a: Search coil EMF : set 5 : magnitude

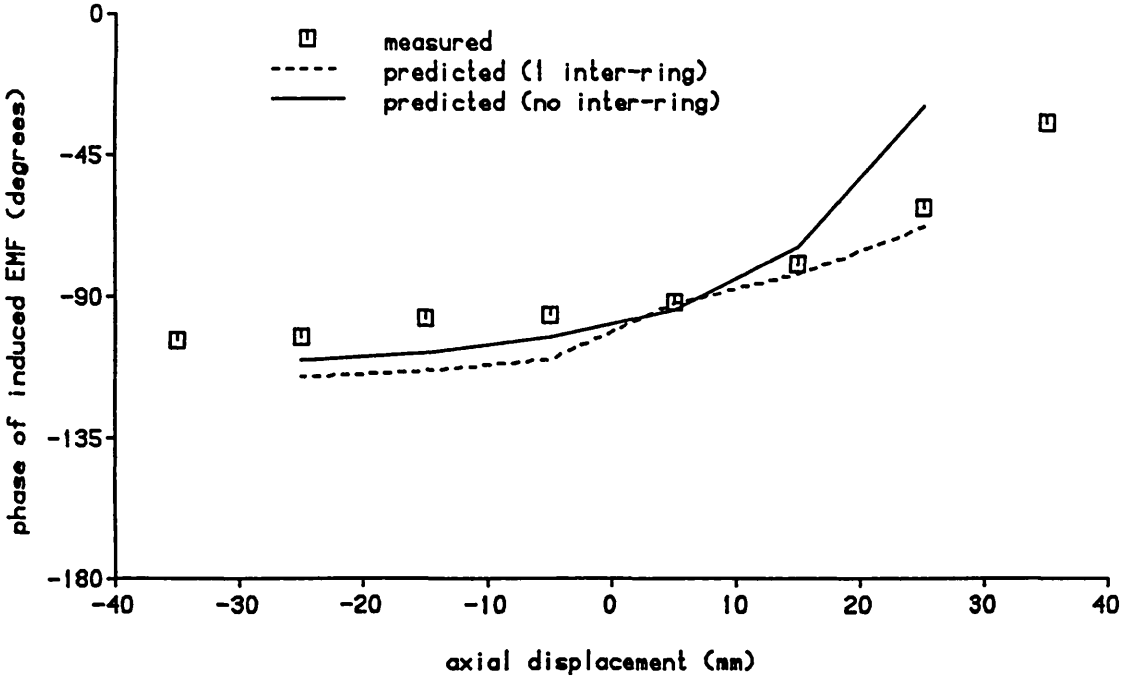


Fig.5.13b: Search coil EMF : set 5 : phase

Figs.5.14 and 5.15 illustrate axial distributions obtained at 10 rpm for sets 1 and 6, at a line voltage of 183 V. Although it was possible to measure the magnitude and phase of the coil EMFs with the machine completely at rest, it was decided to allow it to rotate slowly in order to obtain mean values as the rotor and stator teeth moved in and out of alignment. Once again, the third curve shows the predicted distribution for a non-inter-ring machine. Bar-to-bar currents are therefore seen to limit the flux density at the ends of the core, causing the axial variation to repeat itself over each half of the machine.

The relationship between the thoretical and practical results presented above is thought to be sufficiently close to justify the analysis developed in Section 3. A brief theoretical study of inter-ring effects is given in Appendix 8.5.

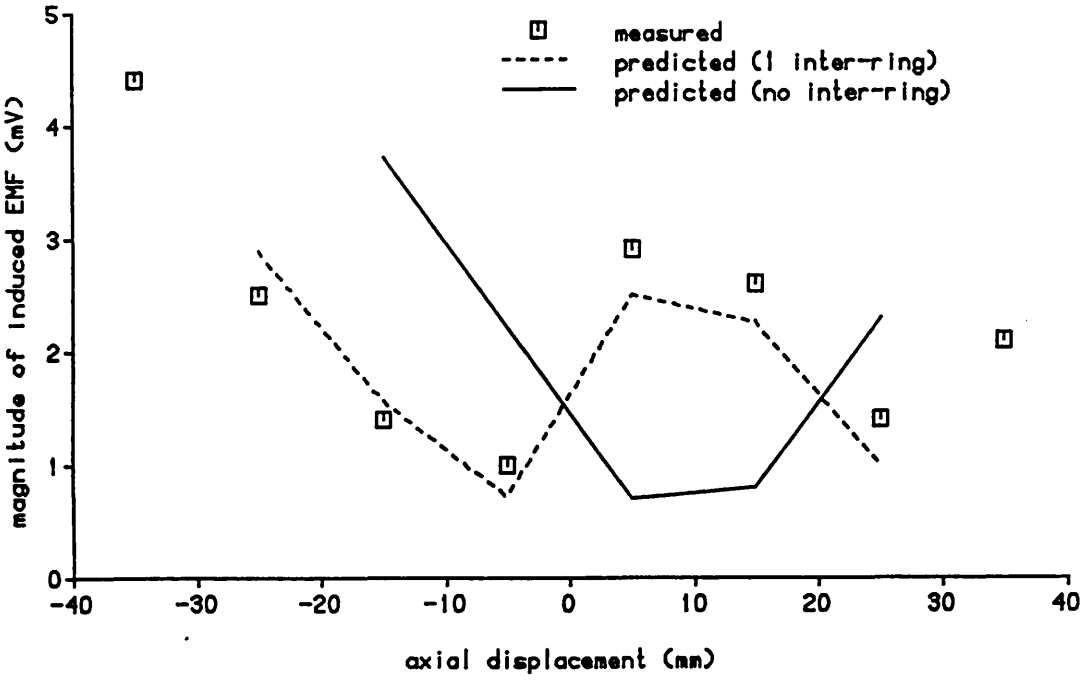


Fig.5.14a: Search coil EMF : set 1 : magnitude

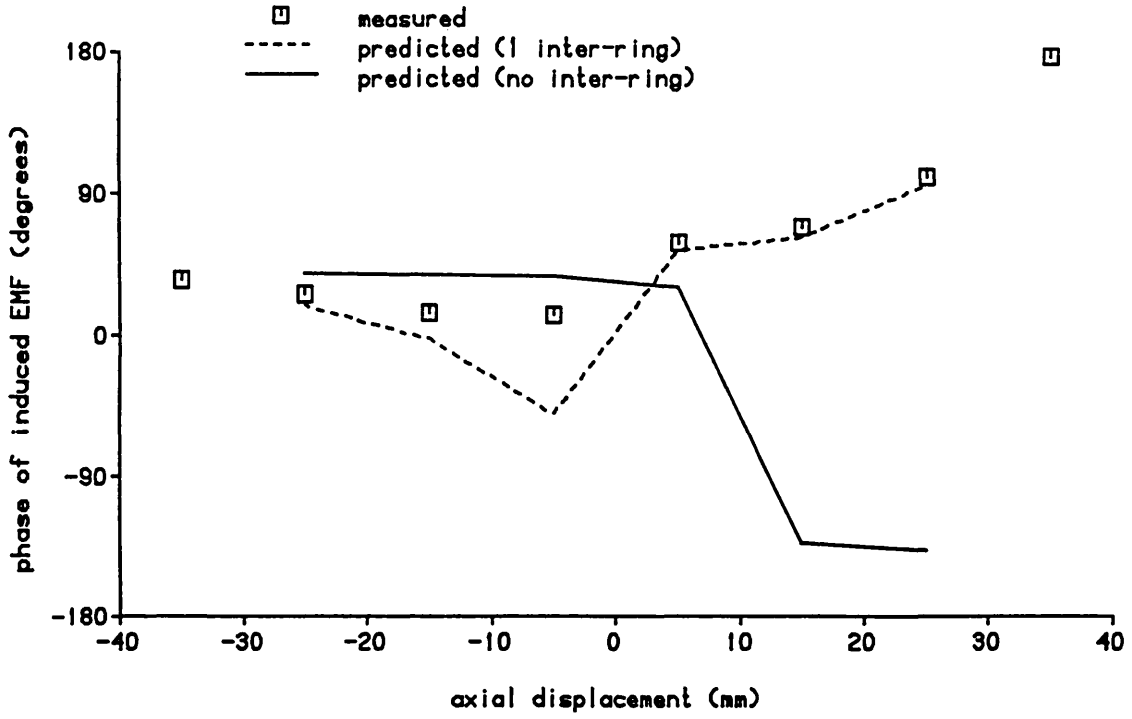


Fig.5.14b: Search coil EMF : set 1 : phase

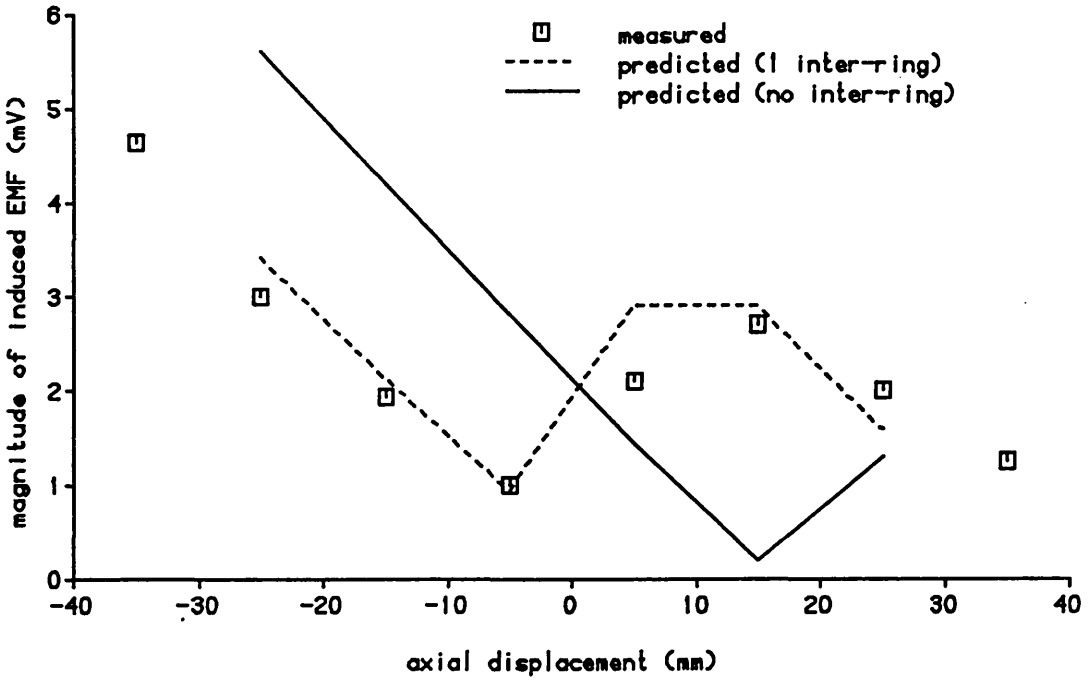


Fig.5.15a: Search coil EMF : set 6 : magnitude

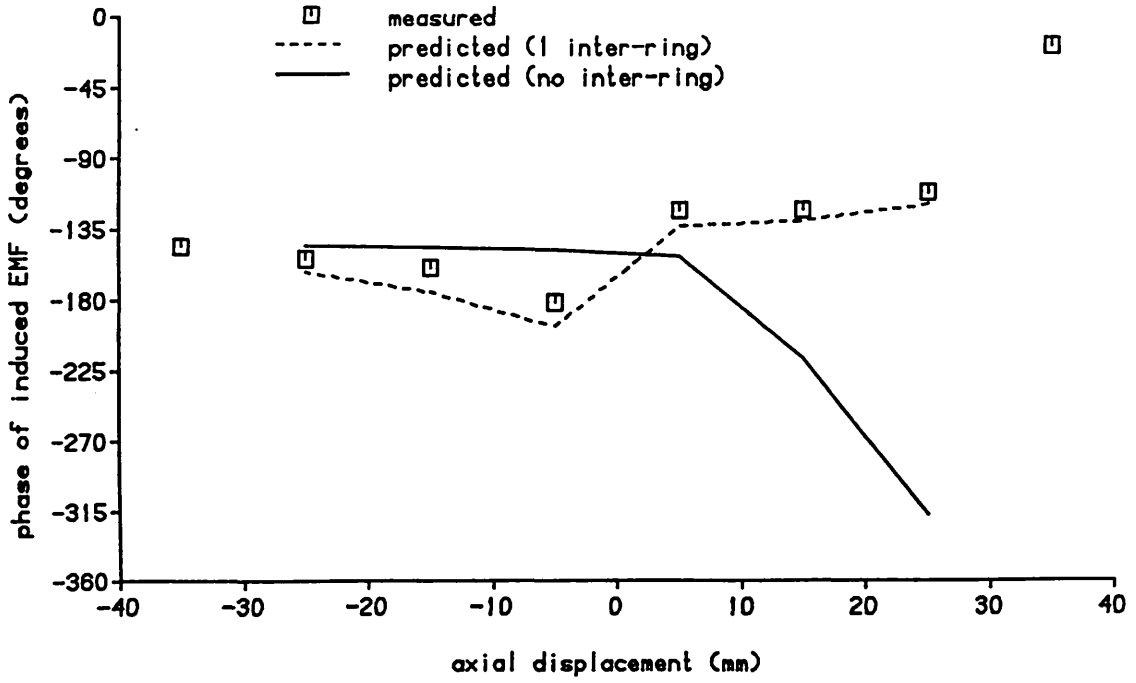


Fig.5.15b: Search coil EMF : set 6 : phase

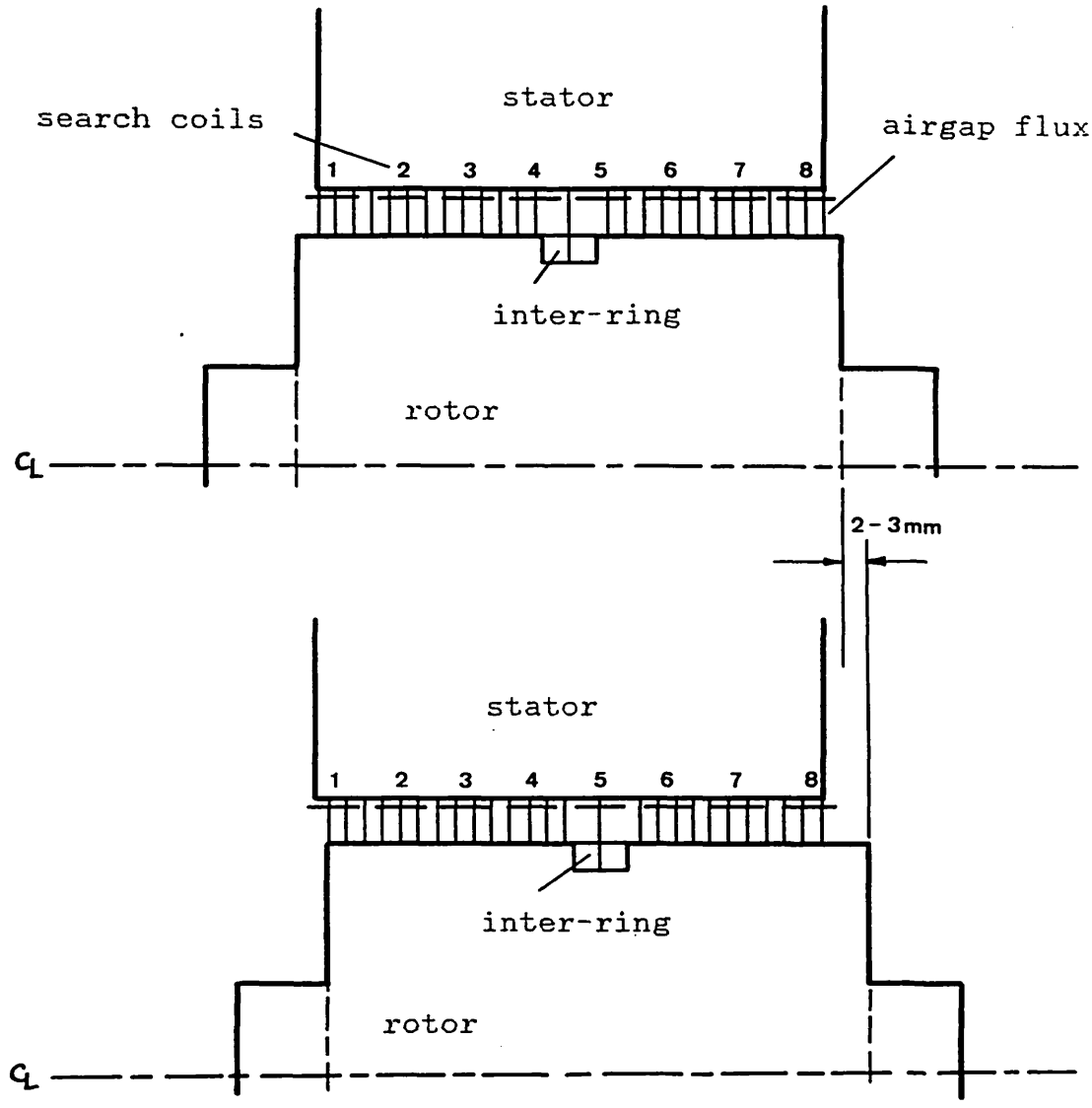


Fig.5.16: Axial misalignment of stator and rotor cores

5.3 Power-factor improvement

After the search-coil study had been completed, the original machine was rewound by a local firm. The existing stator coils were removed and discarded, and new main and subharmonic windings were installed to the specification of Table.4.3. Some difficulty was experienced in arranging the end-winding overhang, presumably due to the slightly unusual combination of 4- and 2-pole concentric windings. As a result the winder preferred to use a 'split-concentric' [14] arrangement for the subharmonic windings, in which all coils were of the same pitch. The ends of each phase were brought out through the existing terminal box and left trailing.

Before the modified machine was tested to examine experimentally any VAr-reducing effects of the subharmonic field, several preliminary checks were carried out. Having coupled the test motor to the DC load machine, and re-aligned the torque transducer, the end-windings were allowed to reach a constant temperature of 65 ° C, and the following resistances measured:

$$\left.\begin{aligned} R_{s1} &= 4.00\Omega \\ R_{s2} &= 3.98\Omega \\ R_{s3} &= 4.04\Omega \end{aligned}\right\} \text{mean} = 3.10\Omega \qquad \left.\begin{aligned} R_{s4} &= 2.20\Omega \\ R_{s5} &= 2.21\Omega \\ R_{s6} &= 2.19\Omega \end{aligned}\right\} \text{mean} = 2.20\Omega$$

As discussed in Section 5.2.2, the stator end-windings played an important part in determining the overall performance of the singly-wound machine, particularly at low speeds. It was therefore decided to excite each winding separately to try to obtain approximate values of the main and subharmonic end-turn leakage reactances in anticipation of any calculation of airgap power factor, efficiency, etc.

Fig.5.17 illustrates the measured and predicted torque- and input power-speed characteristics, obtained with half rated voltage applied to the set of 4-pole windings alone. A stator end-turn leakage reactance of 4.3Ω was used to achieve the predicted variations. This value is a little higher than the 4.0Ω obtained simply by scaling the original value provided by Bull. The corresponding subharmonic reactance could not be estimated from experimental results, however, since it proved impossible to obtain stable operation of the test motor with only the 2-pole winding connected to the supply. Presumably this was because the torque produced on the subharmonic pole-number wave was not large enough to overcome the frictional torque required to accelerate the machine to no-load speeds. An appropriate figure for the subharmonic end-turn leakage reactance was therefore calculated from the main-winding value by assuming it to be proportional both to the square of the number of turns, and to the mean coil span. Addition of the slot leakage component (eqn.3.35) gave

main winding leakage reactance per phase = 6.0Ω
subharmonic winding leakage reactance per phase = 2.9Ω

The test procedure used to measure the performance of the combined-winding machine was similar to that described in Section 3.2.1. The main and subharmonic windings were connected in series, as shown in Fig.4.7a, and readings of torque, input power and current were recorded at various speeds for full, three-quarters and half rated terminal voltage. Figs.5.18-5.20 show variations in measured values of power factor, efficiency and input VArs to output watts ratio for the original and modified machines. Whilst some degree of power-factor improvement at half rated voltage is

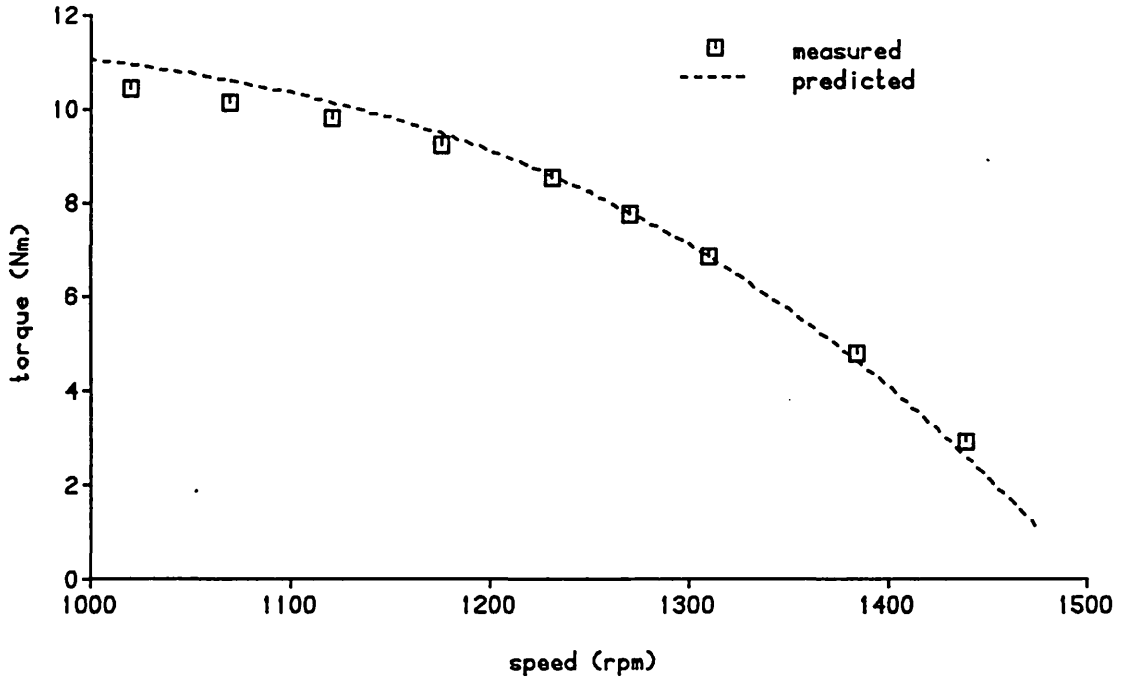


Fig.5.17a: Torque-speed : modified machine : 4-pole winding only

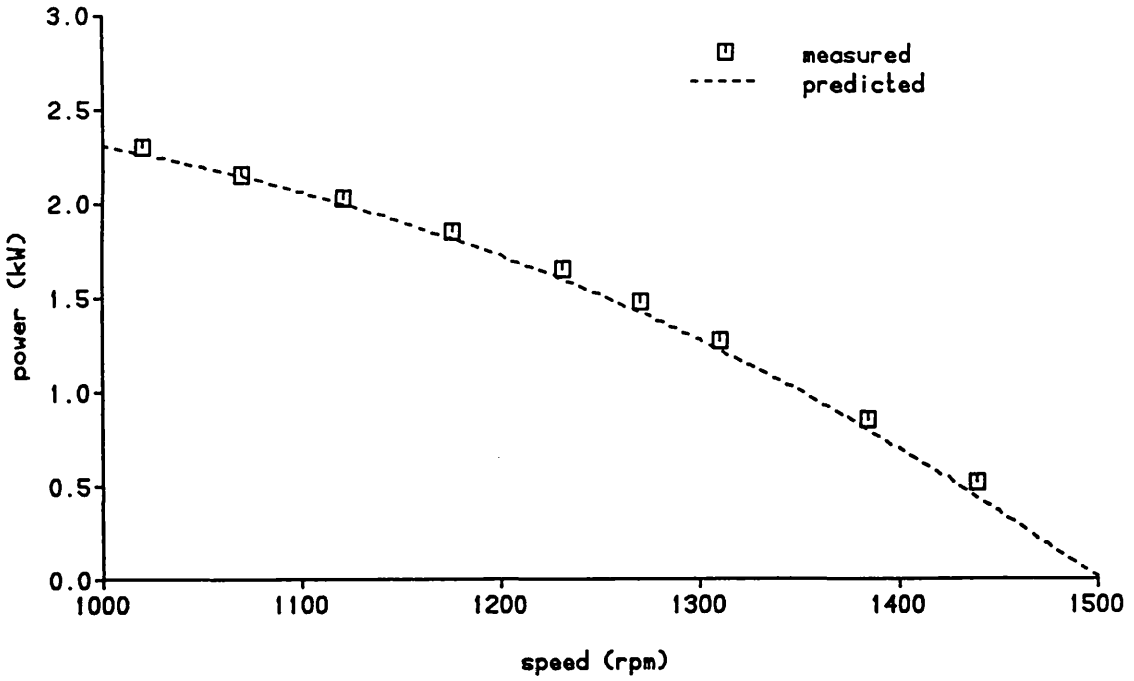


Fig.5.17c: Input power : modified machine : 4-pole winding only

apparent from Fig.5.18a, inspection of Figs.5.18b and c reveals that the addition of the extra set of windings has, in fact, increased the input VArs to output watts ratio and reduced the efficiency. At higher excitations, poorer power factors, lower efficiencies and higher input VArs to output watts ratios are indicated by Figs.5.19 and 5.20.

In Section 4.3 it was stated that the theoretical effects of the subharmonic field on the complex power flow in the combined-winding machine could not be fully determined until suitable values of stator resistance and end-turn leakage reactance were available. Figs.5.21 and 5.22 illustrate the predicted variations in terminal power factor and input VArs to output watts ratio, calculated on the basis of the stator leakage impedances given above, at half and full rated voltage. Although it appears from the experimental characteristics that the addition of the subharmonic field has not resulted in the desired effect on VAr demand, Figs.5.21 and 5.22 show that little, if any, effective power-factor improvement was to be expected from this design.

As further verification of the harmonic analysis, Fig.5.23 illustrates a comparison between measured and predicted variations in terminal input VArs to output watts ratio, calculated at full voltage for the modified machine . The agreement between theory and practice is marginally better for the singly-wound motor. As discussed in Section 4.3, the subharmonic winding was designed on the basis of equal contributions to the rotor copper loss from two harmonic fields. As a result the flux densities in the iron portions of the magnetic circuit produced by the subharmonic field cannot justifiably be neglected. It will be recalled from Section 5.5, however,

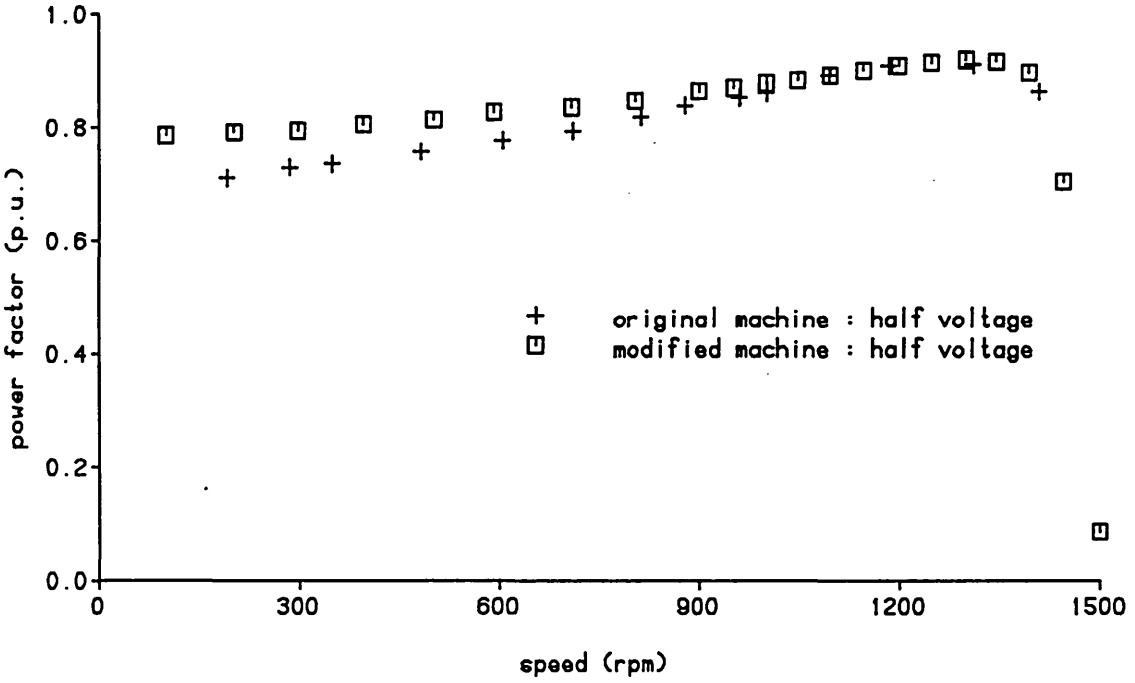


Fig.5.18a: Measured power factor : before and after modification

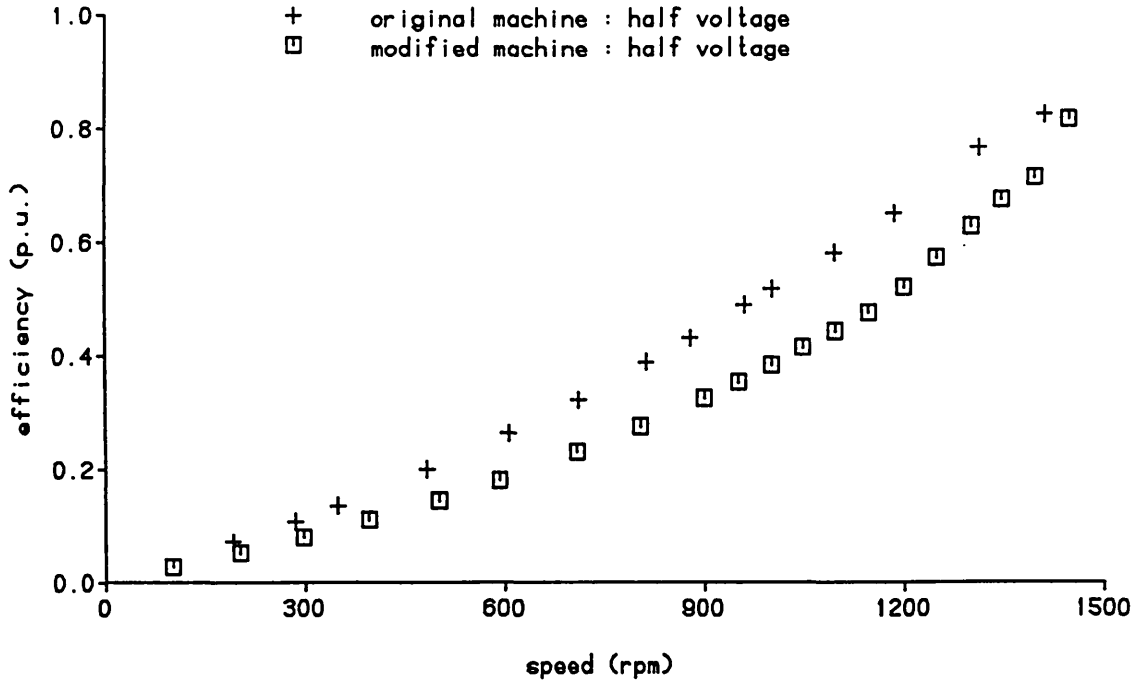


Fig.5.18b: Measured efficiency : before and after modification

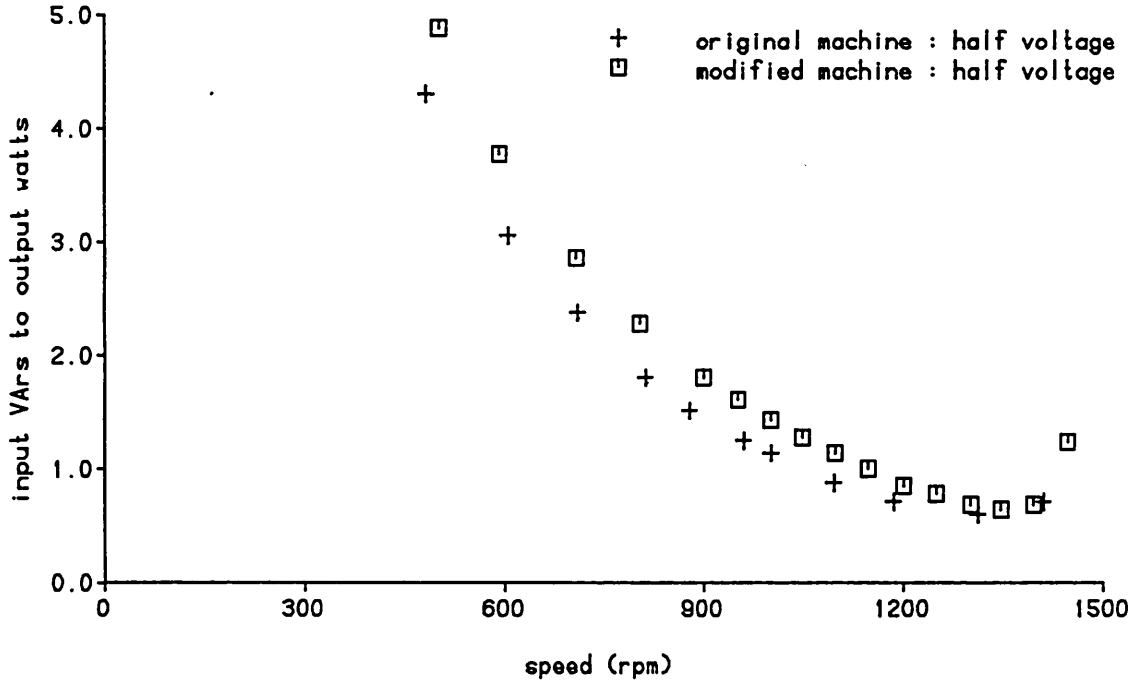


Fig.5.18c: Measured Vars/watts : before and after modification

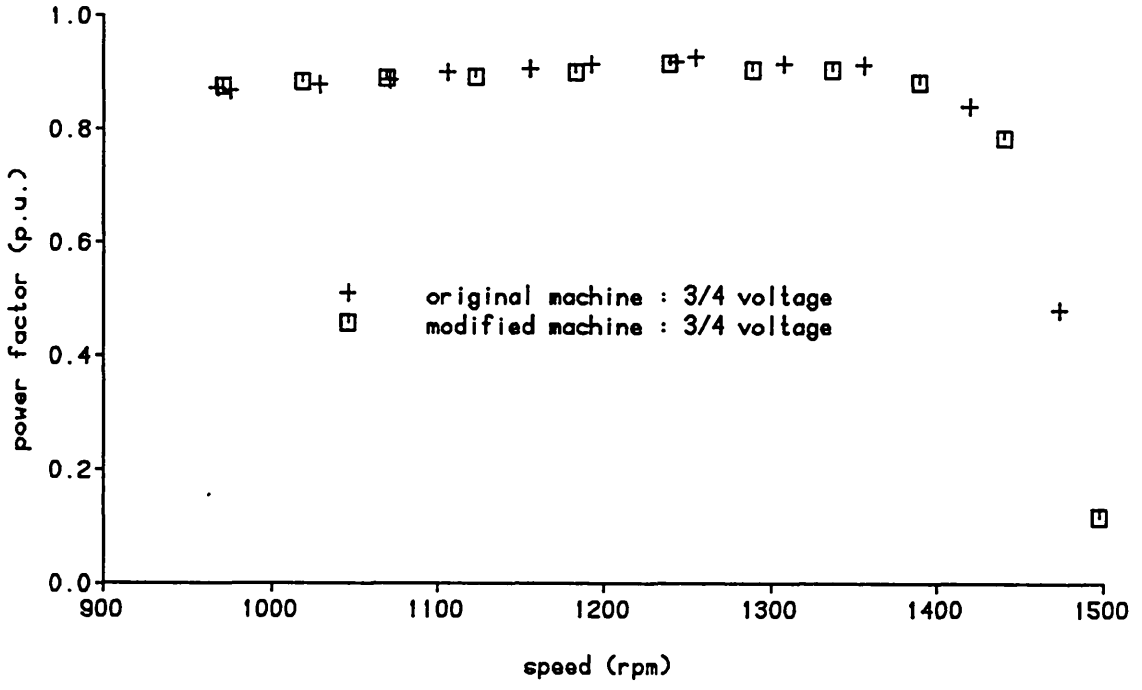


Fig.5.19a: Measured power factor : before and after modification

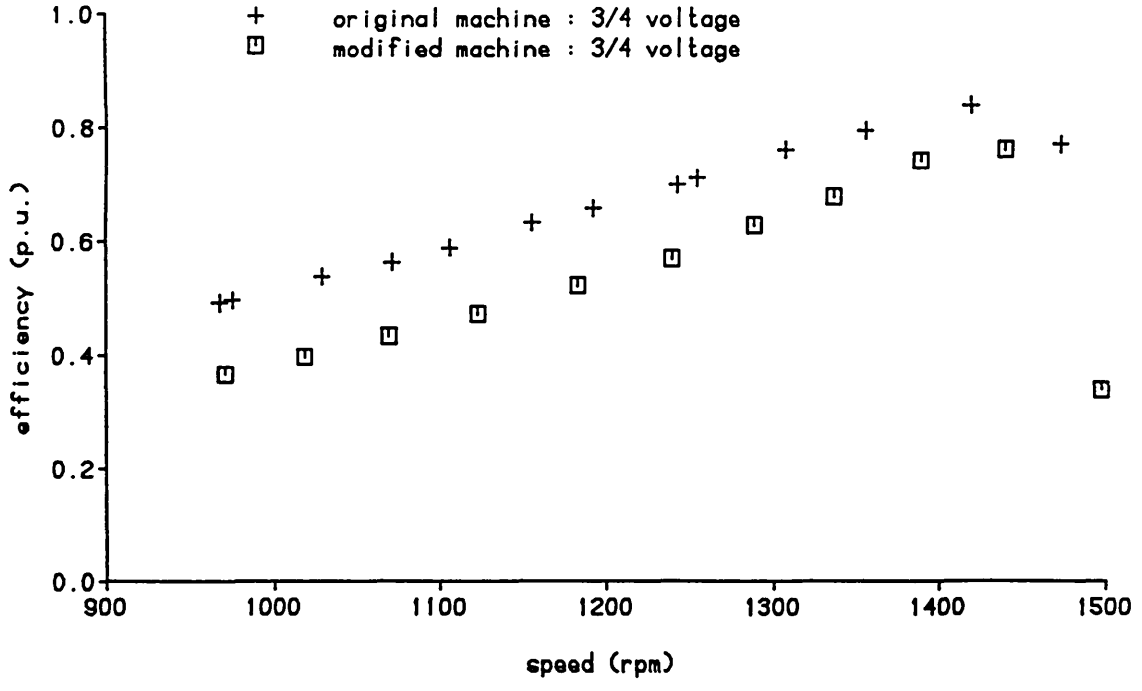


Fig.5.19b: Measured efficiency : before and after modification

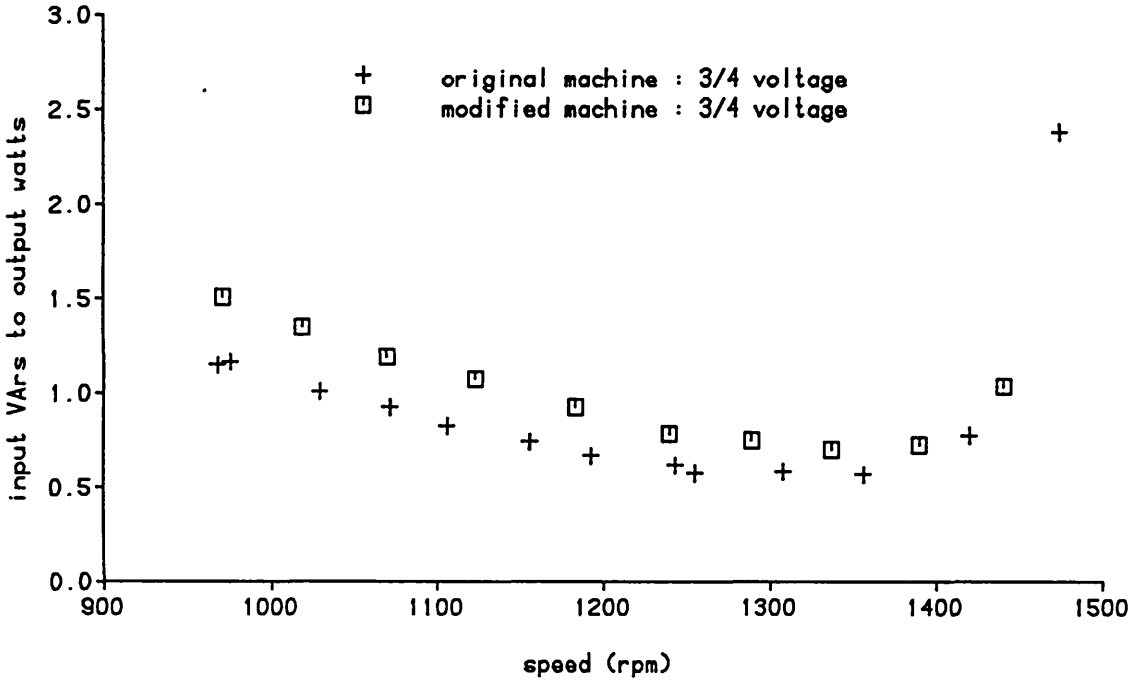


Fig.5.19c: Measured Vars/watts : before and after modification

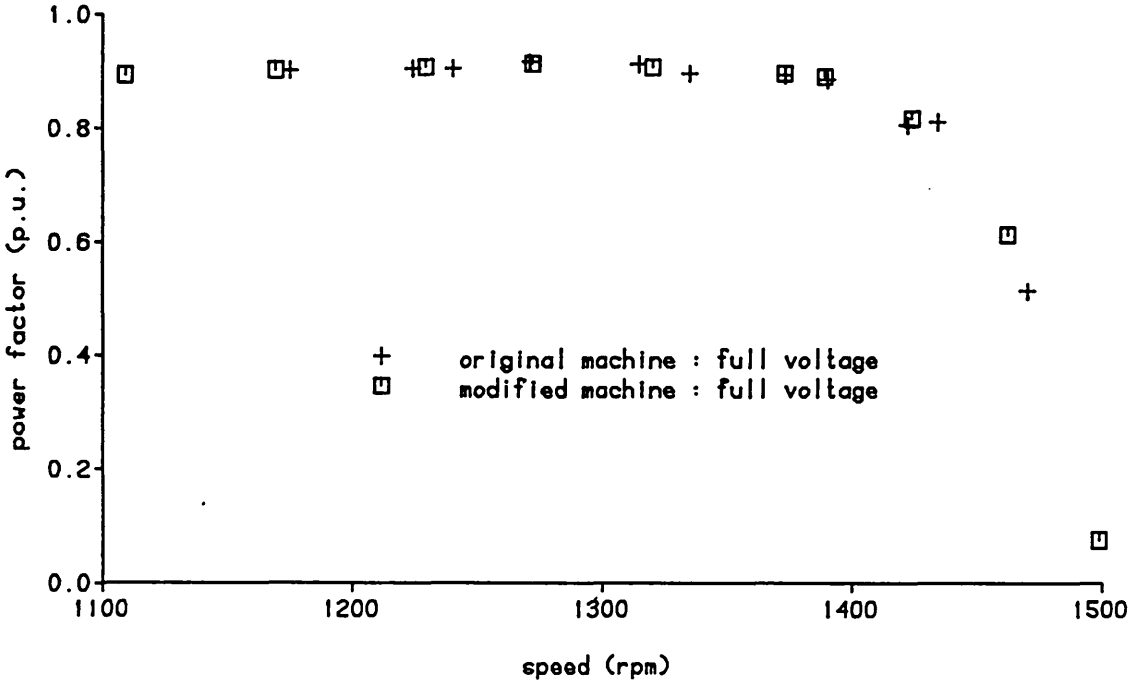


Fig.5.20a: Measured power factor : before and after modification

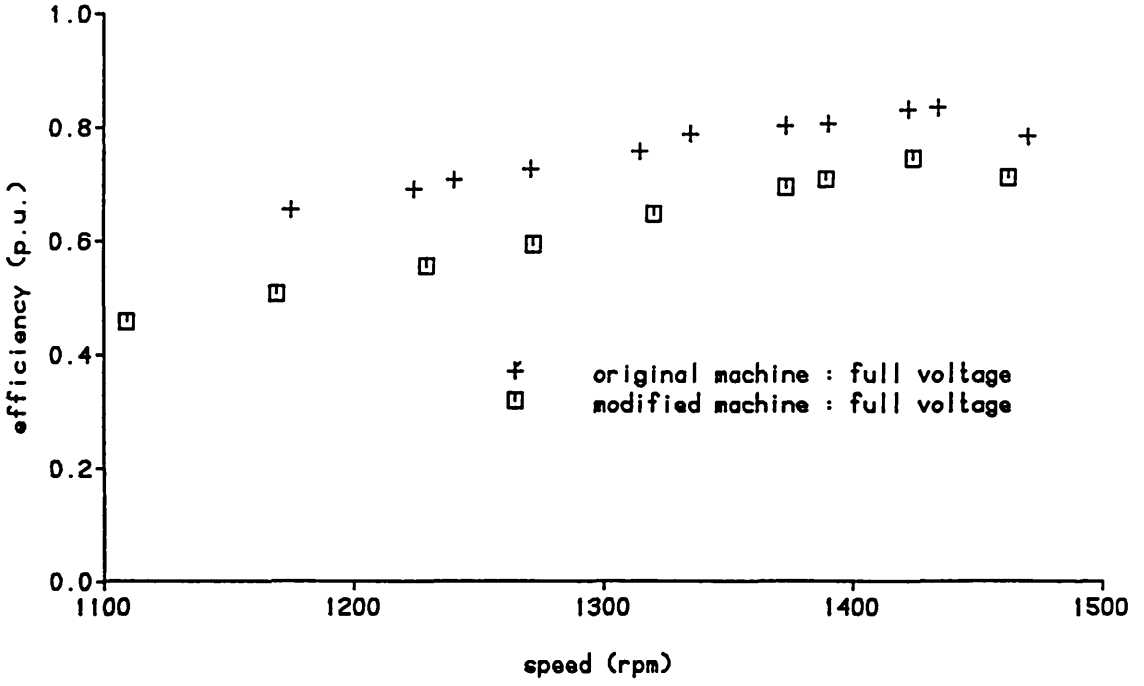


Fig.5.20b: Measured efficiency : before and after modification

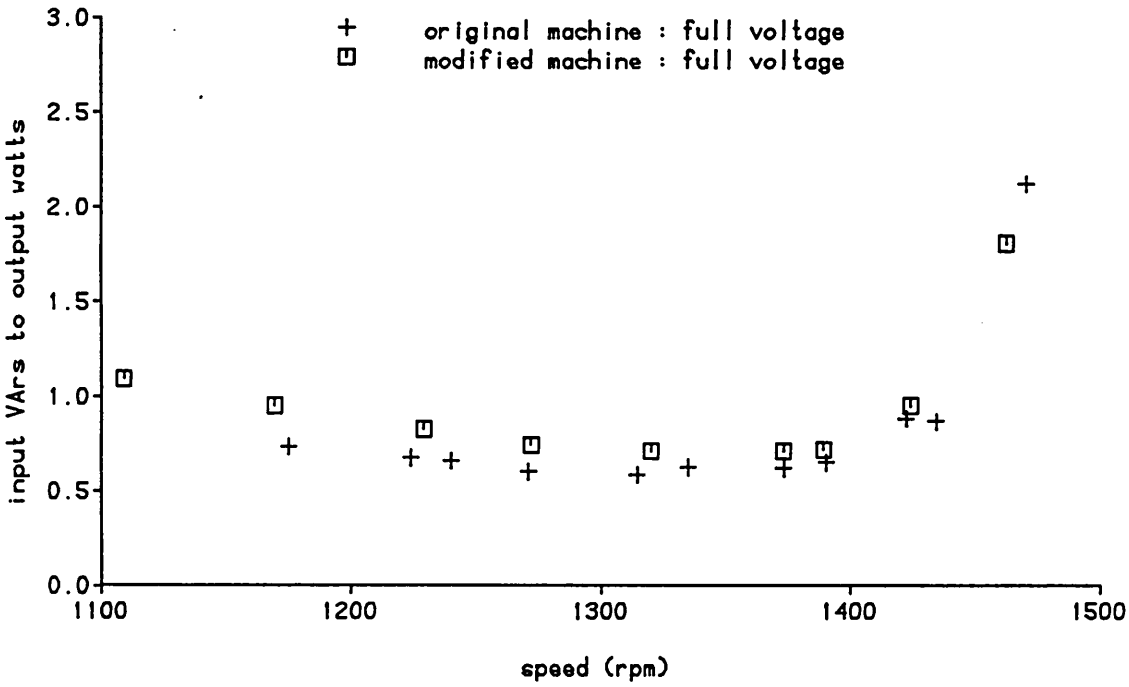


Fig.5.20c: Measured VArs/watts : before and after modification

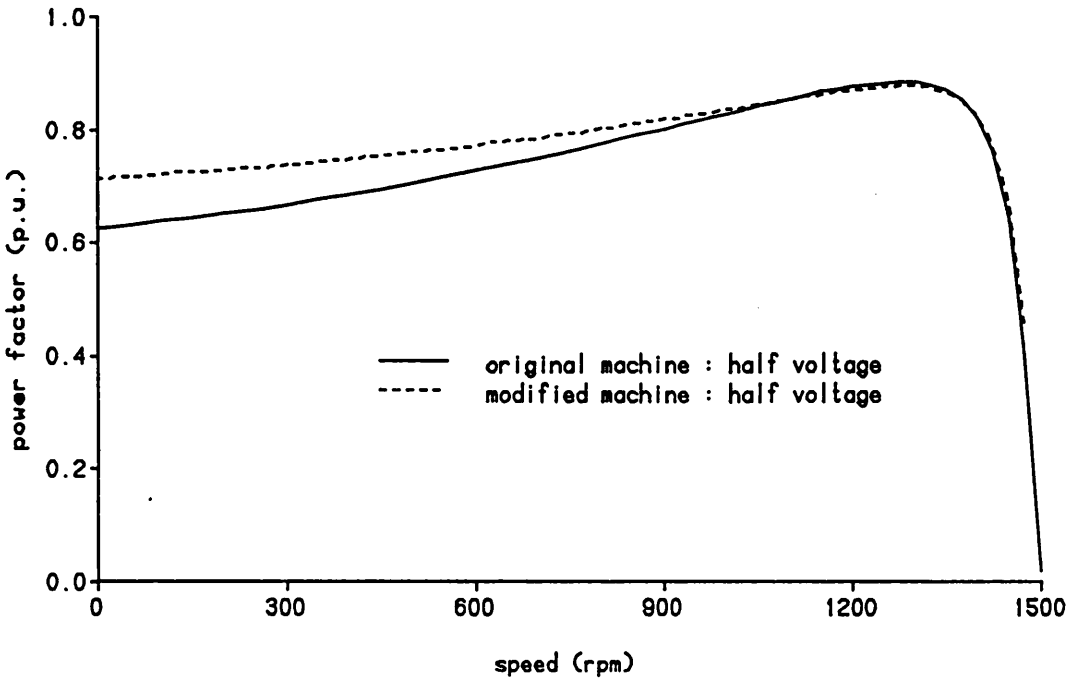


Fig.5.21a: Predicted power factor : before and after modification

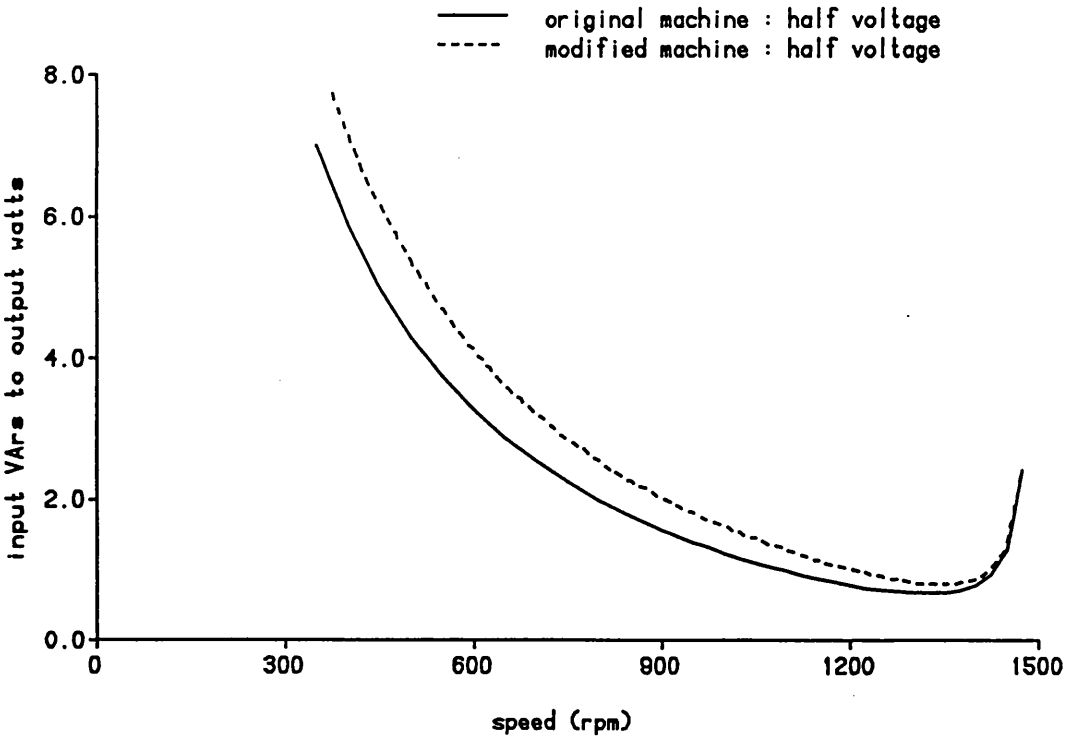


Fig.5.21b: Input VArs to output watts : before and after

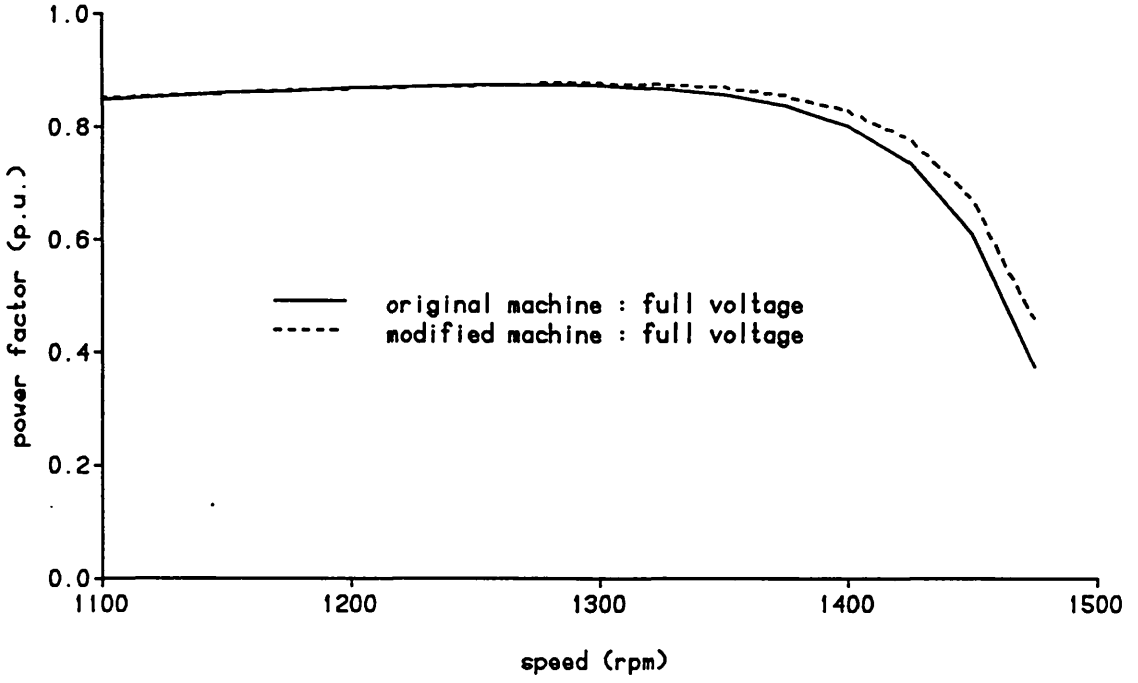


Fig.5.22a: Predicted power factor : before and after modification

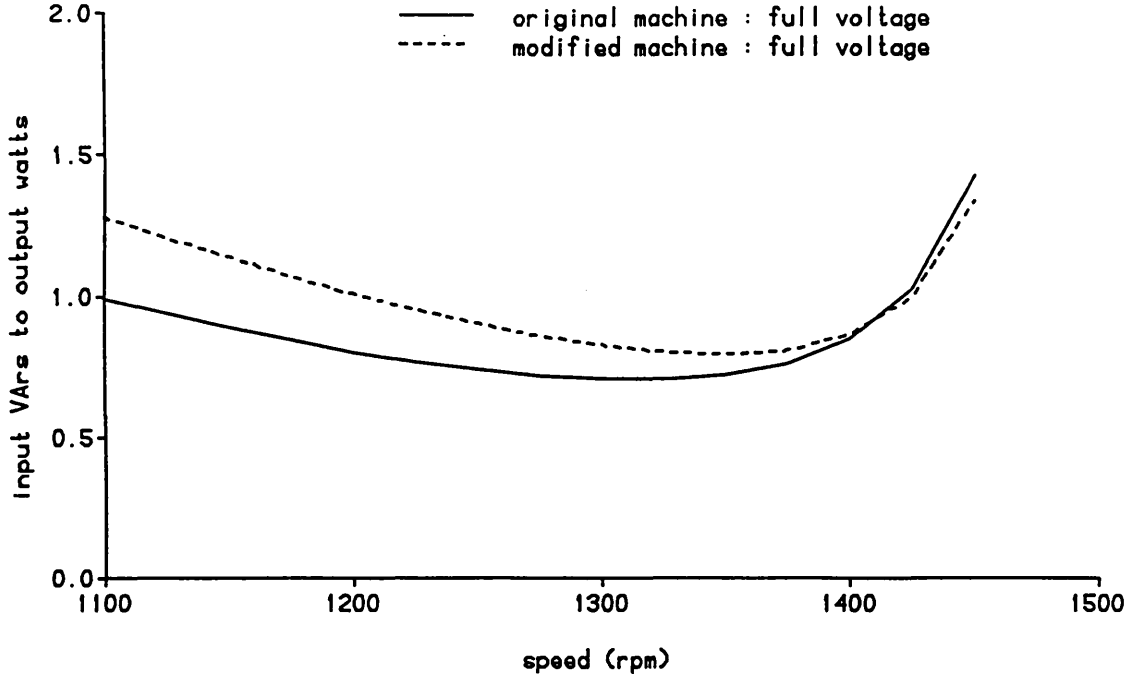


Fig.5.22b: Input VArs to output watts : before and after

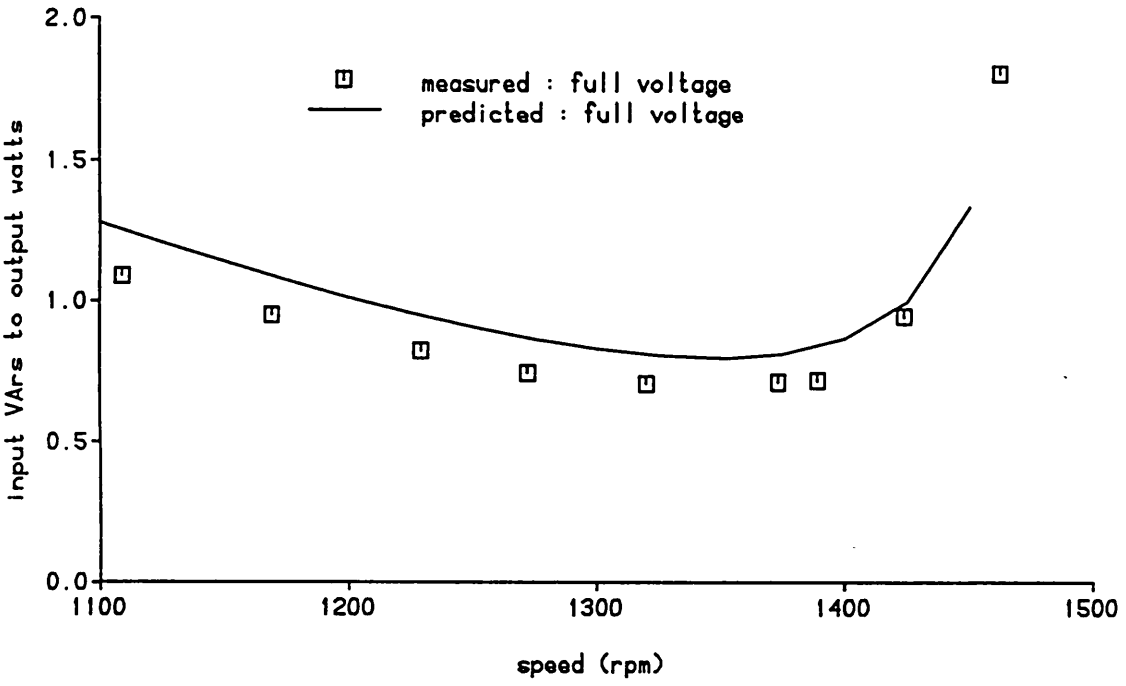


Fig.5.23: Input VArs to output watts : after modification

that it was necessary to make such an assumption in the present saturation-factor calculations. The problem is aggravated by the inclusion of a subharmonic field in particular, since the higher core flux levels and increased magnetic path lengths associated with longer wavelengths imply that the MMF dropped in the iron forms a larger proportion of the total MMF demanded by the complete magnetic circuit.

During the design of the modified windings, only the complex power flowing into the airgap from the stator was considered. The effect of the subharmonic field on the various **airgap** quantities may now be observed by subtracting the complex power consumed in the stator from that flowing in at the terminals. Fig.5.24 shows the variations in terminal and airgap power factor and input VArs to output watts ratio obtained experimentally at half-rated voltage. As the principal slip approaches zero, the stator leakage impedance has only a small effect on the relative magnitudes of overall input watts and VArs. It is therefore justifiable to equate the airgap power factor to the terminal power factor, at rated speed.

The solid-line characteristics included in Figs.5.24 represent the variations in airgap power factor and input VArs to output watts ratio predicted by the simplified analysis used in the selection of the prototype machine (Section 4.2). These results were obtained from the main computer program by neglecting the stator leakage impedance, and by reducing the number of bands from four to two, ensuring a constant airgap length. The saturation factor calculation was omitted entirely, and only the principal and subharmonic components of airgap MMF were included. Fig.5.24 shows that the errors resulting from these assumptions are

considerable at low speeds, although the agreement generally improves as the principal slip decreases. At rated speed, the discrepancy between theory and practice is thought to be sufficiently small to justify the use of the simplified analysis in assessing the derating required to achieve a given improvement in power factor. Fig.5.25 indicates the relationship between VAr reduction and output power for several Bull designs listed in Table 4.1. As the VAr demand is reduced, the contribution to the copper losses from the subharmonic field is increased.

The use of subharmonic fields as a method of power-factor improvement would seem to be a more realistic possibility in higher pole-number machines. For example, from Fig.5.25 it can be seen that a 40% reduction in VAr consumption could be achieved with a derating of approximately 33% for a 12-pole machine, compared to a figure of 39% for a four-pole motor. It should also be noted, however, that the maximum possible VAr reduction decreases as the pole number rises.

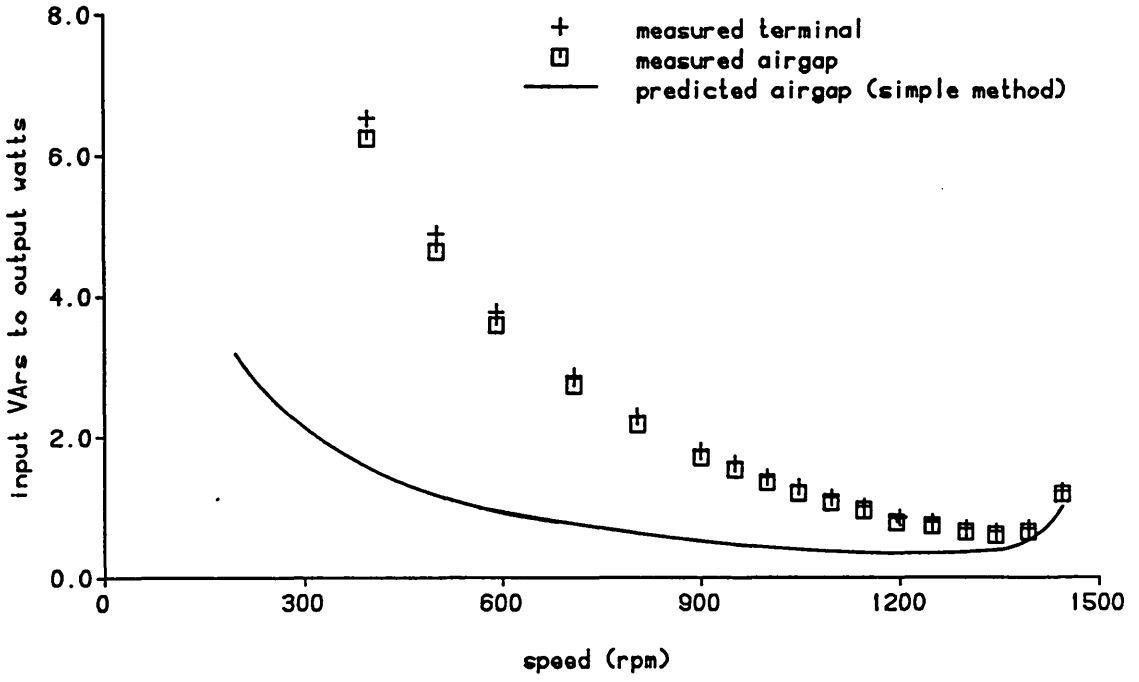


Fig.5.24: Measured terminal/airgap input VArs to output watts

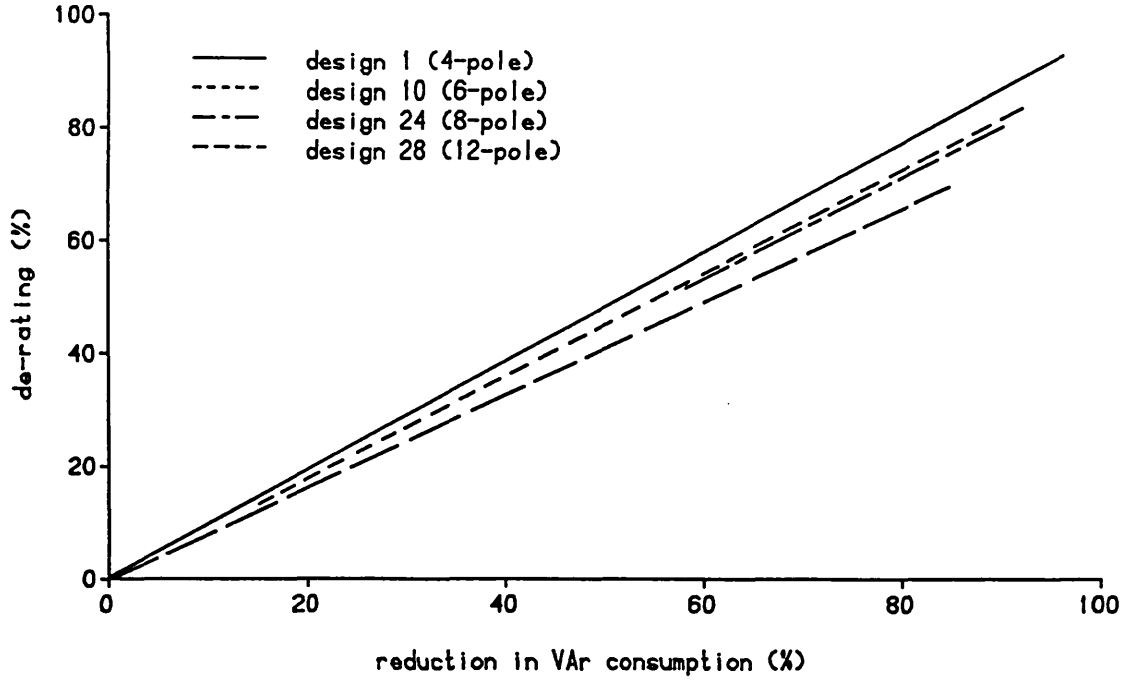


Fig.5.25: De-rating necessary for a given reduction in VAr demand

6. CONCLUSIONS

The main aim of this project was to improve the power factor of a squirrel-cage induction motor at rated speed by stator-winding design alone. It was shown that, subject to certain design constraints, the addition of a forwards-rotating subharmonic field fulfilled the requirements for an effective reduction in reactive power consumption. Approximately half of Bull Electric's induction motors were found to satisfy these constraints, and a four-pole prototype machine was selected as a suitable candidate for an experimental investigation of power-factor behaviour. A procedure was then formulated which enabled separate four- and two-pole windings to be designed on the basis of varying contributions to the rotor copper loss from the subharmonic field.

Although an improvement in power factor was not achieved in practice for the prototype motor, the results presented in Section 5.3 demonstrate the validity of the harmonic analysis employed to predict active and reactive power flow conditions within the modified machine. The simplified calculations described in Section 4 may be used to assess the feasibility of incorporating subharmonic fields into an existing design. Equipped with a set of characteristics similar to those illustrated in Fig.5.25, it is possible for the machine designer to obtain an estimate of the required derating for a given improvement in power factor at rated speed. The answer to the final question of economic viability will ultimately depend on the intended application.

Although secondary to the main theme of the project, the development and verification of an analysis of induction

machines with one or more inter-rings is a useful extension to previous coupling-impedance techniques. One of the most significant effects of adding inter-rings is that the effective skew is reduced. This is the cause of the apparent increase in torque over the entire speed range. In fact, Appendix 8.4 shows that it is necessary to increase the circumferential rotor skew in proportion to the number of bands, if the original reduction of undesirable harmonic currents in the rotor cage is to be maintained.

The distinction between the discrete nature of the circumferentially-directed currents that flow along the low impedance path provided by the inter-ring, and that of the continuous inter-bar current distribution observed in diecast-rotor machines with poor bar-iron insulation, is important. In the inter-ring case, the airgap flux density variation repeats itself over each band of the machine. It is suggested that such a redistribution of flux may be of some benefit in preventing the imbalance of radial forces from producing transverse vibration, thus helping to reduce audible noise at high values of slip. This area of the work deserves further attention. It would be appropriate to perform a comparison of sound emission spectra of skewed and unskewed machines, with and without inter-rings. In this way it might be possible to isolate the sources of vibration.

In terms of performance prediction, a reasonably simple modification to the basic analysis may find application in skewed machines with and without inter-rings. The division of the core into a relatively large number of 'sub bands' would seem to be a possible way of incorporating the significant axial variations in flux denstiy into the magnetic-circuit calculations. Different saturation factors would be obtained for each sub band, high resistance

inter-rings forming the band boundaries. It would, however, then be necessary to employ an iterative technique to determine flux density levels in the iron portions of the magnetic circuit, since tooth saturation in particular is likely to affect the final flux distribution.

7. REFERENCES

1 LAITHWAITE, E.R., and KUZNETSOV, S.B.: 'Cage-rotor induction motor with unity power factor', IEE Proc.B, 1982, **129**, (3), pp.143-150

2 LAITHWAITE, E.R., and KUZNETSOV, S.B.: 'Reactive power generation in high-speed induction machines by continuously occurring space transients', IEEE Trans. Mag., 1980, **MAG-16**, pp.716-718

3 LAITHWAITE, E.R., and KUZNETSOV, S.B.: 'Test results obtained from a brushless unity-power-factor induction machine', IEEE Trans. Power App. Syst., 1981, **PAS-100**, (3), pp.2889-2897

4 KUZNETSOV, S.B., 'Brushless asynchronous induction machines with leading VAr capability', Ph.D thesis, 1981, Imperial College, London

5 LAITHWAITE, E.R., and KUZNETSOV, S.B.: 'Development of an induction machine-commutated thyristor inverter for traction drives', IAS Conference Record, September 1980, pp.580-585

6 LAITHWAITE, E.R., and KUZNETSOV, S.B.: 'Natural commutation of current-source inverter by cage-rotor induction machines', IAS Conference Record, September 1980, pp. 897-902

7 LAITHWAITE, E.R, and KUZNETSOV, S.B.: 'A magnetically self-compensated inducion machine for natural thyristor commutation', IEEE Trans. Mag., 1982, **MAG-18**, pp.256-260

8 PHILLIPS, K.P., 'Current-source inverter for AC motor drives', IEEE Trans. Ind. Appl., 1972, **IA-8**, (6), pp. 679-683

9 WILLIAMSON, S.: 'Power-factor improvement in cage-rotor induction motors', IEE Proc.B, 1983, **130**, (2), pp. 121-129

10 WILLIAMSON, S., and LAITHWAITE, E.R.: 'Generalised harmonic analysis for the steady-state performance of sinusoidally-excited cage induction motors', IEE Proc.B, 1985, **132**, (3), pp.157-163

11 WILLIAMSON, S., and SMITH, A.C.: 'Steady-state performance of 3-phase cage motors with rotor-bar and end-ring faults', IEE Proc.B, 1982, **129**, (3), pp.93-100

12 LAITHWAITE, E.R.: 'The goodness of a machine', Proc. IEE, 1965, **112**, (3), pp.538-541

13 LIWSCHITZ-GARIK, M.M.: 'Computation of skin-effect in bars of squirrel-cage induction motors', Trans. Am. Inst. Electr. Engrs., 1955, **74**, (3), pp.768-771

14 SAY, M.G.: 'Alternating current machines', (Pitman, London, 1984)

15 VEINOTT, C.G.: 'Theory and design of small induction motors', (McGraw Hill, New York, 1956)

16 BINNS, K.J., HINDMARSH, R., et al.: 'Effect of slot skewing on flux distribution in induction machines', IEE Proc., 1971, **118**, (3/4), pp.543-549

17 WILLIAMSON, S., and SMITH, A.C.: 'Field analysis for rotating induction machines and its relationship to the equivalent-circuit method', IEE Proc.B, 1980, **127**, (2), pp.83-89

18 LIWSCHITZ-GARIK, M., and WHIPPLE, C.C.: 'Electric machinery', (Van Nostrand, New York, 1946)

19 ADKINS, B.: 'The general theory of electrical machines', (Chapman and Hall, London, 1964)

20 HELLER, B., and HAMATA, V.: 'Harmonic field effects in induction machines', (Elsevier Scientific Publishing Company, Amsterdam, 1977)

21 SMITH, A.C.: 'A field analysis for rotating induction machines', PhD thesis, 1980, University of Aberdeen

22 HENRICI, P.: 'Applied and computational complex analysis' Vol.1, (Wiley-Interscience, 1974)

23 BINNS, K.J., and DYE, M.: 'Effect of slot skew and iron saturation on cogging torques in induction machines', Proc.IEE, 1970, **117**, (7), pp.1249-1252

24 BINNS, K.J.: 'Cogging torques in induction machines', ibid., 1968, **115**, (12), pp.1783-1790

25 ALGER, P.L.: 'Induction machines', (Gordon & Breach, New York, 1970)

26 LINKOUS, C.E.: 'Effect of skew on induction motor magnetic fields', Trans. Amer. Inst. Elect. Engrs., 1955, **74**, Pt.III, pp.760-765

27 KREYSZIG, E.: 'Advanced engineering mathematics', (Wiley, New York, 1983)

28 STEPHENSON, G.: 'Mathematical methods for science students', (Longman, London, 1973)

29 HELLER, B., and JOKL, A.L.: 'Losses in squirrel-cage motors due to rotor skew', IEEE Trans. Pow. App. Syst., 1971, **PAS-90**, (2), pp.556-563

30 SUBBAO RAO, V., BUTLER, O.I.: 'Stray losses of polyphase cage-induction motors with particular reference to the condition of imperfect bar-iron insulation', Proc. IEE, 1969, **116**, (5), pp.737-749

31 SMIKAL, F.: 'Induction machines with interrings', Proceedings of international conference on electrical machines', Brussels, 1978

32 CHEN LI-REN: 'The analysis and computation of stability characteristics of a squirrel-cage induction motor with middle ring', Proceedings of international conference on electrical machines, Munich, 1986

33 YANG, S.J.: 'Low-noise electrical motors', (Clarendon Press, Oxford, 1981)

34 DIGITAL EQUIPMENT CORPORATION.: 'Microcomputers and memories', (DEC, 1982)

8 APPENDICES

8.1 Self-compensating induction motor tests

In the latter part of the power-factor improvement work undertaken by Kuznetsov [1,2,3], the VAr-generating ability of the so-called 'self-compensating induction motor' was harnessed by driving a 112 kW protoype machine from a simple six-step current-source inverter (CSI). The SCIM was said to have supplied sufficient reactive power to effect natural, load commutation of the inverter thyristors [4-7], without the usual need for complicated forced-commutation circuitry, or large capacitor banks [8]. As the prototype motor was still available at the time this project was started, it was decided to check these claims independently by re-evaluating the performance of the CSI-SCIM combination.

8.1.1 Construction of current-source inverter

It was soon apparent that the existing CSI hardware was inadequate for the purpose of testing the SCIM. The control logic functioned in a somewhat haphazard manner, so it was decided to replace this with a custom-designed circuit. The completed inverter was then connected to a constant-current supply, using capactiors in parallel with a resistive load to commutate the thyristors. At first it seemed that several devices were turning on at the wrong times, causing considerable distortion of the load current waveform. Eventually the fault was traced to the snubbers, which were located some distance away from the CSI thyristors. This problem was easily solved by strapping the R-C network

directly across the device terminals. Further protection was afforded by inserting a small (0.05 mH) choke in series with each thyristor. The rate of rise of current was thus limited, protecting each device from excessive di/dt stress, and, in conjunction with the R-C network, reducing dv/dt.

Some consideration was given to the nature of the constant-current supply to be used for the inverter tests. It was envisaged that 'commutation' capacitors would at first remain connected across the load, gradually being switched out to see if self-commutation was indeed possible. Should a commutation failure occur, however, two of the inverter thryistors would remain on, and the constant-constant-current supply would be short-circuited, causing the DC link current to rise with a finite time constant. Some form of overcurrent protection was therefore necessary if devices were not to be destroyed each time a commutation failure occurred.

A phase-delay rectifier (PDR) was the best choice for the DC source, permitting greater flexibility in controlling the link current. By blanking off the gating signals applied to the PDR thyristors, it was possible to reduce the current in the link rapidly to zero, should it rise above a preset level. In normal operation, the gating angle of the thyristors determined the magnitude of the link current, which was therefore set manually as required. A similar design (without overcurrent protection) had been adopted in the previous arrangement [4], but, although the 'power' hardware was evident, no control logic could be found. As a result, new electronic circuits had to be designed, built and tested. It was also necessary to uprate the cables and fuses in the existing PDR hardware. The completed PDR-CSI converter was tested and found to work satisfactorily at

currents up to 50 A.

8.1.2 Sinusoidal (50 Hz) Testing

Although the primary objective was to test the SCIM when driven from the inverter, some preliminary sinusoidal tests were necessary. These served firstly as an independent check on previous leading power factor claims, and secondly as a means of establishing which terminal connections to use with the inverter. The SCIM had a main winding and a recovery, or asynchronous condenser (ASC) winding, which were to be connected in parallel. It was not clear which of the ASC terminals should be connected to which of the main windings, so confusion arose as to the particular orientation necessary for unity power factor operation. The problem was further compounded by the actual terminal labelling corresponding neither to that given previously [4], nor to that indicated by simple continuity tests. It was eventually decided that, having corrected the labelling system, the 50 Hz tests would be performed using all possible main - ASC winding interconnections with two fixed star points. Full details are given in Table 8.1.

The test arrangement is shown in Fig.8.1. The three-phase autotransformer provided a variable-voltage supply, and independent speed control of the load machine enabled the specified slip to be set. Experimental results are given in Table 8.2. A dual-beam oscilloscope was used to determine the relative phase relationship between load voltage and current. Measurements were taken under conditions as close as possible to those given by Kuznetsov:

Slip 3.3%

Table 8.1: Definition of winding interconnections

Main winding terminals labelled	A1	B1	C1
star point	A2	B2	C2
ASC winding terminals labelled	D1	E1	F1
	D2	E2	F2

a) ASC star point D2 E2 F2

connection no.	A1	B1	C1	(remains fixed)
1	D1	E1	F1	
2	D1	F1	E1	
3	E1	D1	F1	(connect as shown)
4	E1	F1	D1	
5	F1	D1	E1	
6	F1	E1	D1	

b) ASC star point D1 E1 F1

connection no.	A1	B1	C1	(remains fixed)
7	D2	E2	F2	
8	D2	F2	E2	
9	E2	D2	F2	(connect as shown)
10	E2	F2	D2	
11	F2	D2	E2	
12	F2	E2	D2	

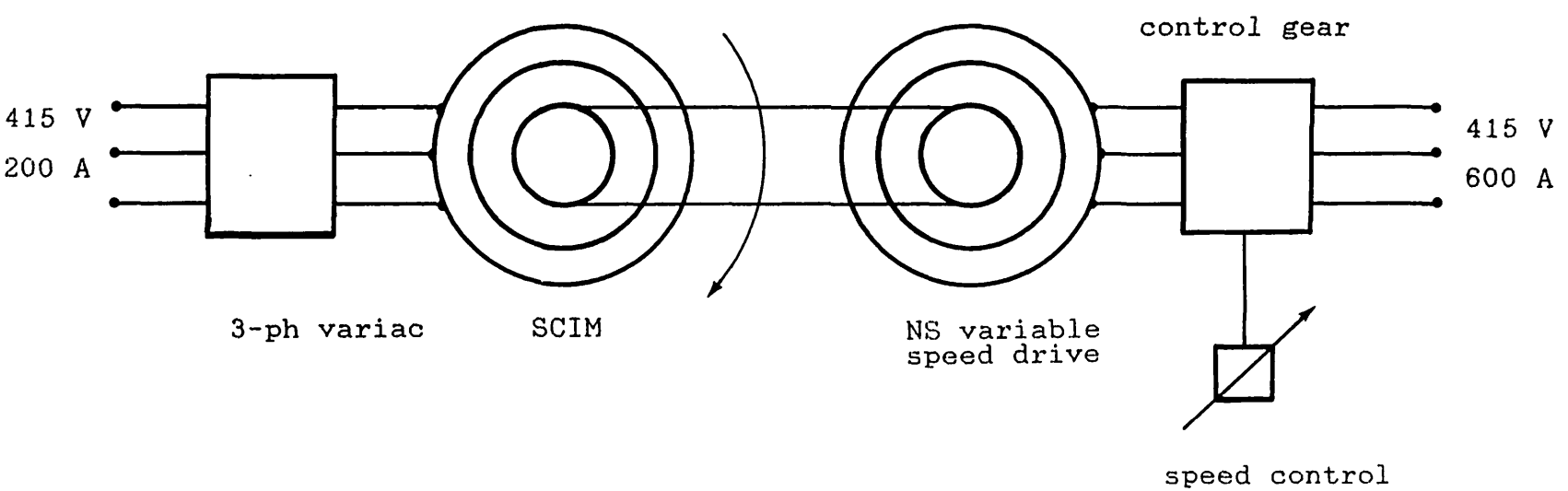


Fig.8.1: SCIM test schematic

Table 8.2 Preliminary sinusoidal tests

		Phase A				Phase B				Phase C			
		V	A	kW	pf	V	A	kW	pf	V	A	kW	pf
Conn.1	MAIN	127	80	7.7	-	124	63	5.8	-	124	87	7.1	-
729 rpm	ASC	127	21	2.3	-	124	33	4.2	-	124	20	2.3	+
Conn.2	MAIN	64	82	1.9	-	64	123	1.7	-	61	123	3.9	-
726 rpm	ASC	64	54	1.8	-	65	84	-1.0	-	61	134	2.3	-
Conn.3	MAIN	62	102	0	-	65	100	3.1	-	63	64	1.2	-
748 rpm	ASC	62	134	-2.7	-	65	140	6.0	-	64	8	0.7	-
Conn.4	MAIN	61	160	5.8	-	63	152	6.2	-	65	142	5.5	-
727 rpm	ASC	61	100	-1.6	-	63	72	-2.6	-	65	110	-4.0	+
Conn.5	MAIN	62	120	-1.6	-	66	132	-0.4	-	61	114	0.7	-
732 rpm	ASC	62	57	3.4	-	66	82	4.2	-	61	81	7.2	-
Conn.6	very noisy; very high currents; extremely unbalanced												

Notes
1. Currents via 200:1 C.T.'s.
2. Amps, volts and watts measured using Cambridge Test Sets.
3. Seperate instrumentation for main and ASC windings.
4. In pf (power factor) column, - signifies lag; + signifies lead.

Table 8.2 Preliminary sinusoidal tests (continued)

		Phase A				Phase B				Phase C			
		V	A	kW	pf	V	A	kW	pf	V	A	kW	pf
Conn.7	MAIN	45	121	1.2	-	49	124	5.8	-	48	110	1.9	-
727 RPM	ASC	45	99	-0.8	-	49	95	4.2	-	48	66	1.6	-
Conn.8	MAIN	58	122	3.1	-	65	92	4.1	-	64	82	1.6	-
727 RPM	ASC	58	137	1.3	-	65	74	3.9	-	64	70	-2.4	-
Conn.9	MAIN	90	63	3.3	-	64	88	0.9	-	63	123	2.7	-
728 RPM	ASC	90	88	-4.5	-	64	10	-0.8	-	63	108	0.4	-
Conn.10	MAIN	92	84	-1.5	-	96	112	-1.7	-	87	103	0.9	-
727 RPM	ASC	92	129	10.8	+	96	86	7.5	-	87	114	8.1	+
Conn.11	MAIN	79	156	10.0	-	78	136	9.3	-	78	138	8.2	-
726 RPM	ASC	79	36	-2.9	+	78	67	-4.7	-	78	56	-2.8	+
Conn.12	very noisy; very high currents; extremely unbalanced												

Notes
1. Currents via 200:1 C.T.'s.
2. Amps, volts and watts measured using Cambridge Test Sets.
3. Seperate instrumentation for main and ASC windings.
4. In pf (power factor) column, - signifies lag; + signifies lead.

Main Current	191 A
ASC Current	95 A
Input Power	112 kW

The NS load macine was rated at 150 hp (112 kW) at 1450 rpm, although the actual maximum generated power at 743 rpm was 92 kW. As expected, for several main - ASC connections, the motor was excessively unbalanced and no measurements were taken.

The most important point to note from Table 8.2 is that whatever the terminal connection, the SCIM drew a lagging current from the supply. Connection no. 1 produced the best power factor, and it was this orientation which was used for the majority of the inverter tests. It can be inferred [4], however, that it is connection no. 4 which should yield leading power factor, so some inverter tests were performed with this arangement. As a final check, the phase relationship between motor voltage and current was observed for **all** possible main - ASC winding interconnections. The power factor was lagging in all cases.

8.1.3 Inverter Tests

As mentioned earlier, the original idea was to ensure thyristor commutation by connecting static capacitors across the motor terminals. These could then gradually be switched out to see if commutation would continue as a result of motor action alone.

The SCIM was therefore driven by the load machine, with a three-phase capacitor bank connected in delta across its terminals. Before the inverter could be switched on,

however, the SCIM was found to self excite with more than approximately 500 uF/ph connected. This phenomenon demonstrated an inherent weakness of the system. The capacitance required to correct the motor power factor to unity was very nearly that required to self excite the machine in the generator mode [14]. In both cases the function of the capacitor was to supply the reactive volt-amperes demanded by the machine. Dangerous overvoltages occurred whenever the SCIM was motoring and the inverter supply cut off, due, for example, to a commutation failure. In general, the problem is solved using diodes [8] to isolate the capacitance from the load. As this was undesirable in the present system, series resistance was inserted between the capacitor bank and the machine, as illustrated in Fig.8.2.

The addition of extra series resitance had two major effects. Firstly, when operating as a generator, the capacitor voltage was reduced, thus decreasing the generated reactive power and preventing self excitation. Secondly, when motoring, the overall losses were increased, the terminal voltage reduced, and the reactive power demand decreased. Less capacitance was required for unity power factor, while more was necessary for self excitation.

It was then possible to switch on the inverter supply with the SCIM running, without any danger of self excitation. Preliminary tests indicated, however, that even with 0.4Ω/phase added resistance, capacitor values of 320 uF were required to achieve load commutation. With zero external resistance, the over-current protection circuitry shut down the PDR irrespective of commutaton capacitance, slip or inverter frequency. Further sinusoidal tests were therefore performed to obtain an approximate idea of the likely minimum commutaton capacitance.

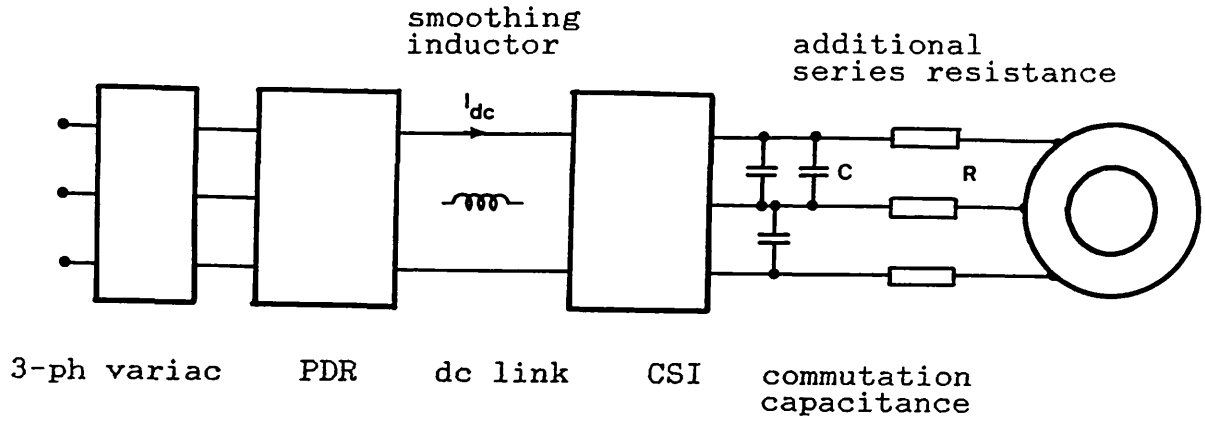


Fig.8.2: Current-source inverter tests

The motor was fed from a variable-voltage supply, as described in Section 8.1.2. Measurements of terminal voltage, line current and power were taken for all three phases, and the power factor calculated. Readings were recorded with zero and 0.4Ω/phase additional resistance over a limited range of slip. Fig.8.3 demonstrates the effect of added series resistance on the capacitance necessary for unity power-factor operation. It is appreciated that the capacitances indicated in Fig.8.3 are not necessarily those required for thyristor commutation, but at least they give some indication of likely values.

As a true test of the ability of the SCIM to load-commutate the CSI thyristors, it was appropriate to perform the final inverter tests with zero additional series resistance. This proved impossible, however, since whenever the extra resistance was reduced below 0.2Ω , the system seemed to become unstable. The DC link current started to oscillate at approximately 2-3 Hz, increasing in amplitude

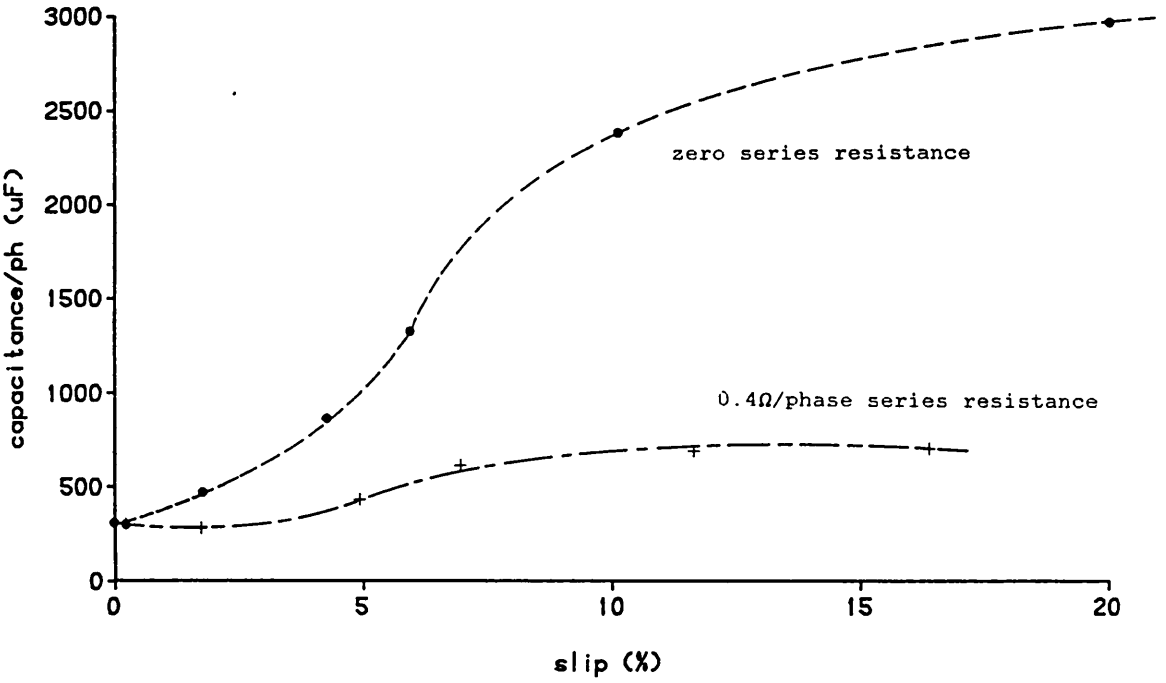


Fig.8.3: Effect of series resistance on commutation capacitance

until the overcurrent trip was activated. The effect was more marked at low values of slip.

As a result, 0.4 Ω/phase series resistance was included in the circuit so that some qualitative results could be obtained. The test procedure was as follows. With the capacitors set to the values calculated above, and 2.2 Ω /ph series resistance inserted to prevent self excitation, the SCIM was accelerated to the required speed by the load machine. The inverter frequency was set to give the required slip and the PDR supply switched on, supplying the motor with a fairly low current (approximately 50 A). The rotor speed was maintained constant as the power input to the SCIM was increased and the series resistance reduced. The commutation capacitors were then gradually switched out and the values immediately preceeding commutation failure recorded.

The majority of tests were performed using connection no.1, although some measurements were taken with no.4, as mentioned earlier. Readings of DC link current, inverter output voltage and motor voltage were taken for slips of between one and twenty per cent. Results are given in Tables 8.3 and 8.4. Note that in all cases a substantial capacitance is necessary, despite the additional series resistance.

8.1.4 Conclusions

The lack of experimental data from previous research dictated a somewhat haphazard approach to the work presented here. This is illustrated in the sinusoidal test procedure, where every 'reasonable' permutation of main-ASC winding connection was tried. The inverter tests, while by no means exhaustive, certainly gave a clear indication of SCIM performance under most of the more commonly encountered operating conditions.

Firm conclusions can be drawn as to the performance of the SCIM. When fed from a sinusoidal supply, a lagging power factor was observed for all main-ASC winding connections. Using a constant-current, variable-frequency inverter supply, some compensatory commutation capacitance was always needed, irrespective of supply frequency, slip, etc. Indeed, the capacitor values necessary for commutation were remarkably similar to those required for unity power factor operation from a sinusoidal supply, as can be seen by comparing results presented in Fig.8.3 and Table 8.4. There would seem to be little doubt that the so-called self-compensated induction machine always absorbed reactive power from the supply.

Table 8.3: Inverter-fed tests : connection no.1

Rotor speed (rpm)	Inverter frequency (Hz)	Slip (%)	Added resistance (Ω/ph)	Minimum commutation capacitance (uF/ph)	DC Link current (A)	Motor current (A rms)	Output voltage (V rms)	Motor voltage (V rms)
569 *	39.7	4.4	0.4	320	88	62.8	55.0	30.6
569 *	43.0	7.6	0.4	320	128	96.3	78.8	39.7
569 *	42.2	10.5	0.4	320	100	85.6	58.0	28.0
569 *	44.3	14.0	0.4	320	116	94.0	65.3	30.0
569 *	47.5	20.7	0.4	>1240	-	-	-	-
650	43.9	1.0	0.4	280	62	48.0	83.5	69.5
650	45.2	4.0	0.4	320	100	79.6	70.0	41.2
650	46.7	7.0	0.4	320	106	86.2	63.8	33.3
650	48.2	10.0	0.4	420	128	116.2	64.5	23.8
650	51.0	15.0	0.4	680	126	130.0	72.5	27.5
650	54.2	20.0	0.4	>1240	-	-	-	-
700	47.2	1.0	0.4	260	90	68.0	86.5	63.7
700	48.7	4.0	0.4	300	115	94.2	75.8	42.0
700	50.2	7.0	0.4	320	120	105.6	71.0	38.0
700	51.9	10.0	0.4	620	126	110.1	70.5	37.5
700	54.8	15.0	0.4	680	130	108.8	70.3	37.1
700	20.0	20.0	0.4	>1240	-	-	-	-
750	50.5	1.0	0.4	260	46	38.0	64.8	52.0
750	52.2	4.0	0.4	280	102	83.2	73.0	43.2
750	53.8	7.0	0.4	400	102	86.0	64.5	35.5
750	55.5	10.0	0.4	540	138	107.2	75.2	40.8
750	58.8	15.0	0.4	620	130	100.4	70.0	38.0
750	62.5	20.0	0.4	>1240	-	-	-	-
800	53.8	1.0	0.4	260	84	51.2	113.3	98.6
800	55.5	4.0	0.4	260	116	92.4	87.5	54.5
800	57.3	7.0	0.4	420	124	98.0	75.0	42.7
800	59.3	10.0	0.4	640	128	107.2	75.0	42.3
800	62.7	15.0	0.4	720	150	116.0	79.0	44.6
800	66.7	20.0	0.4	1220	120	92.5	62.5	35.9

Notes
1. Capacitance available 0 - 1240 uF in 20 uF steps.
2. Voltages and currents are for phase A only.
3. * indicates speed obtained with control set to minimum

Table 8.4: Inverter-fed tests : connection no.4

Rotor speed (rpm)	Inverter frequency (Hz)	Slip (%)	Added resistance (Ω/ph)	Minimum commutation capacitance (uF/ph)	DC Link current (A)	Motor current (A rms)	Output voltage (V rms)	Motor voltage (V rms)
650	43.8	1.0	0.4	920	152	128.0	71.0	27.1
650	45.2	4.0	0.4	820	154	126.4	70.3	25.0
650	46.7	7.0	0.4	640	170	137.6	75.8	25.7
650	48.2	10.0	0.4	760	152	124.0	67.5	22.6
650	51.0	15.0	0.4	840	152	123.2	66.3	23.0
650	54.2	20.0	0.6	840	151	123.6	67.5	23.8
750	50.5	1.0	0.4	920	150	129.2	74.0	31.1
750	52.3	4.0	0.4	940	140	118.8	67.0	26.4
750	53.8	7.0	0.4	940	142	115.6	66.0	24.3
750	55.5	10.0	0.4	920	142	116.2	64.5	23.8
750	58.8	15.0	0.4	920	160	130.0	72.5	27.5
750	62.5	20.0	0.4	920	162	133.6	75.0	29.3
850	59.0	4.0	0.4	840	150	122.9	73.0	29.8
850	63.0	10.0	0.4	920	151	119.6	71.5	27.9
850	70.8	20.0	0.4	920	150	120.4	74.0	29.9

Notes 1. Capacitance available 0 - 1240 uF in 20 uF steps.

2. Voltages and currents are for phase A only.

8.2 Conductor-density distributions

Consider the general case of a skewed N-turn coil of span α depicted in Fig.8.4. The conductor density is a function of axial (x), as well as circumferential (y) position, indicated in Fig.8.4 by assuming the coil to be centred at $y=y_0-x\tan\gamma$, where γ is the angle of skew, and y_0 is the circumferential position of the coil centre at the middle of the machine.

The so-called 'complex form' of the Fourier series [27] may be used to resolve the conductor density into an infinite series of harmonic distributions. For a piecewise regular function f(y) [28] of period 2L:

$$f(y) = \sum_{v_k} \bar{F}^k \exp(-jv_k\pi y/L) , \qquad (8.1)$$

where v_k is the harmonic number (an integer), and

$$\bar{F}^k = (1/2L)\int_{L}^{L} f(y) \exp(jv_k\pi y/L)\, dy . \qquad (8.2)$$

In this case $L=\pi d/2$ and the wavenumber k is defined by

$$k = 2v_k/d . \qquad (8.3)$$

Substitution into eqns.8.1 and 8.2 enables the conductor density to be written as

$$c(x,y) = \sum_{v_k} \bar{D}^k(x)\, e^{-jky} , \qquad (8.4)$$

where

$$\bar{D}^k(x) = \frac{1}{\pi d} \int_{-\pi d/2}^{\pi d/2} c(x,y)\ e^{jky}\ dy \ . \qquad (8.5)$$

The integration in eqn.8.5 may be performed with reference to Fig.8.4 to give

$$\bar{D}_s^k(x) = -\frac{2j}{\pi d} K_{bs}^k\ N \sin(k\alpha/2)\ e^{jky_0}\ e^{-jkx\tan\gamma}, \qquad (8.6)$$

in which the slot-mouth width factor K_b^k is given by

$$K_b^k = \frac{\sin(kb/2)}{kb/2} \ . \qquad (8.7)$$

The dependence of $\bar{D}_k$ on axial position may be emphasised by writing

$$\bar{D}^k(x) = \bar{C}^k\ e^{-jkx\tan\gamma} \ , \qquad (8.8)$$

where

$$\bar{C}^k = -\frac{2j}{\pi d} K_{bs}^k \sin(k\alpha/2)\ e^{jky_0} \ . \qquad (8.9)$$

Substituting into eqn.8.4,

$$c(x,y) = \sum_{v_k} \bar{C}^k\ e^{-jk(y+x\tan\gamma)} \ . \qquad (8.10)$$

Note that, if the coil is unskewed, as is usual in the case of a stator winding, eqn.8.10 reduces to the form derived previously [10] :

$$c(y) = \sum_{v_k} \bar{C}^k\ e^{-jky} \ .$$

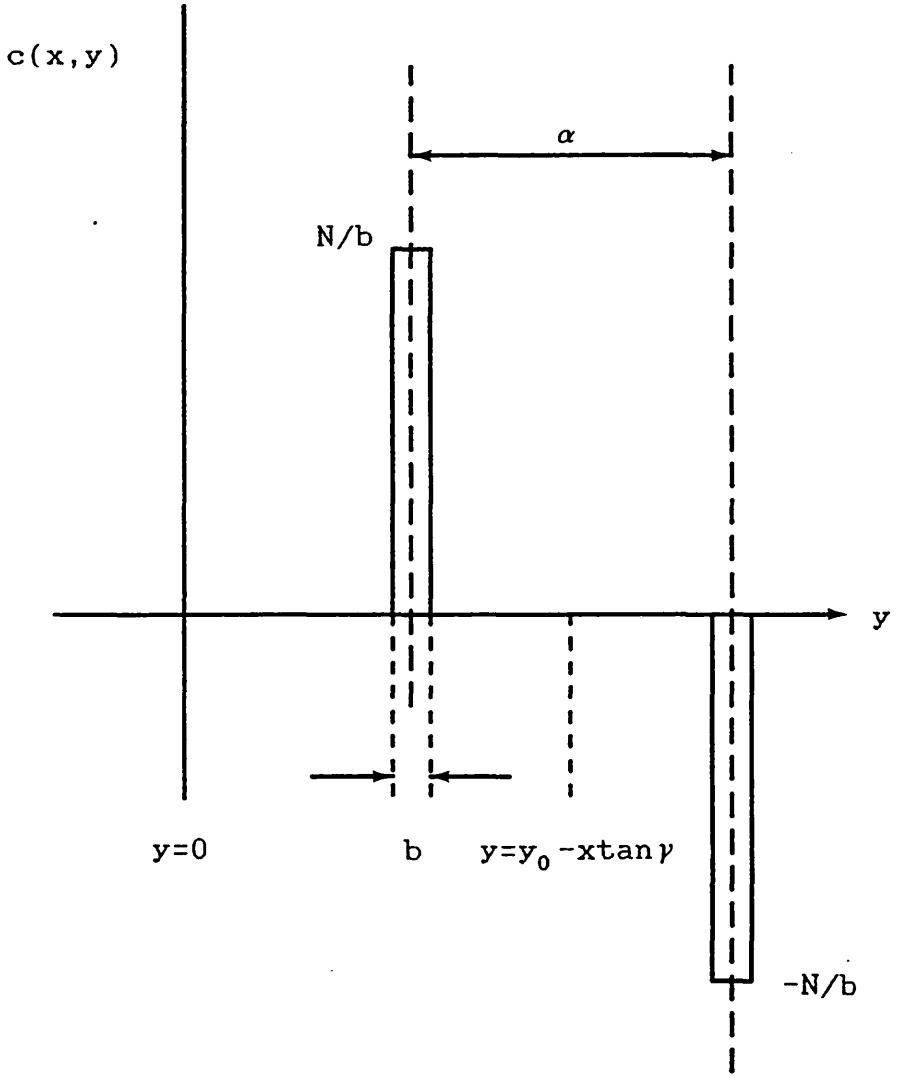


Fig.8.4: Idealised coil model

8.3 Magnetic-circuit calculations

As discussed in Section 3.4, the MMF dropped in the various portions of the magnetic circuit is estimated from the principal harmonic component of airgap flux density. The method described here is a development of the procedure used by Bull in their routine design calculations.

Expressions for the ν_k-th harmonic stator- and rotor-driven airgap flux densities were derived in Section 3.3. The total stator-driven wave is the sum of the contributions from all N_s windings :

$$b_i^k(y,t) = \mathrm{Re}\ \{\sqrt{2}\ \bar{B}_{si}^k\ e^{j(\omega t - ky)}\}\ , \qquad (8.11)$$

where

$$\bar{B}_{si}^k = \frac{j\mu_0}{kg_i}\ \bar{J}_s^k \qquad (8.12)$$

$\bar{J}_s^k$ is the ν_k-th harmonic stator MMF, defined by eqn.3.129. In general, the resultant airgap flux density is the sum of the stator- and rotor-driven components, and it is this quantity which is responsible for establishing the flux levels in the machine. In order to avoid complications arising from axial variations in flux density due to rotor skew, the expressions developed here are derived under no-load conditions, for which it is assumed that the rotor-driven flux is negligible. From eqn.8.11, the peak principal harmonic component of airgap flux density in the i-th band is therefore given by

$$\hat{B}_{gi} = \sqrt{2}\ |\bar{B}_{si}^{k1}|\ . \qquad (8.13)$$

As far as the rotor and stator teeth are concerned, the airgap flux occupying one slot pitch is assumed to pass entirely through the body of the tooth; no fringing is allowed. The stator tooth density is then given by

$$\hat{B}_{sti} = (2/kt_{st}) \sin(k\lambda_s/2) \hat{B}_{gi} , \qquad (8.14)$$

in which t_{st} is the mean width of a stator tooth. For the portion of rotor tooth occupying the i-th band,

$$\hat{B}_{rti} = (2/kt_{rt}) \sin(k\lambda_r/2) \hat{B}_{gi} , \qquad (8.15)$$

The corresponding expressions used by Bull are

$$\hat{B}_{st} = (\lambda_s/t_{st}) \hat{B}_g \; ; \; \hat{B}_{rt} = (\lambda_r/t_{rt}) \hat{B}_g , \qquad (8.16)$$

where it has been assumed that the width of the tooth is negligible in comparison to the principal harmonic wavelength.

The corresponding field strengths (H_{sti}, H_{rti}) are obtained from the steel manufacturer's magnetisation curves. The teeth MMFs are

$$F_{sti} = H_{sti} \, h_{st} \; ; \; F_{rti} = H_{rti} \, h_{rt} , \qquad (8.17)$$

where h_{st} and h_{rt} are the overall lengths of a stator and rotor tooth respectively.

In order to calculate the core MMFs on a similar basis it is necessary to divide the back-iron within half a principal pole pitch into N segments, as shown in Fig.8.5. As N increases, the path taken by the flux in the core becomes short enough for the field strength to be assumed to remain sensibly constant along its length. The peak flux in

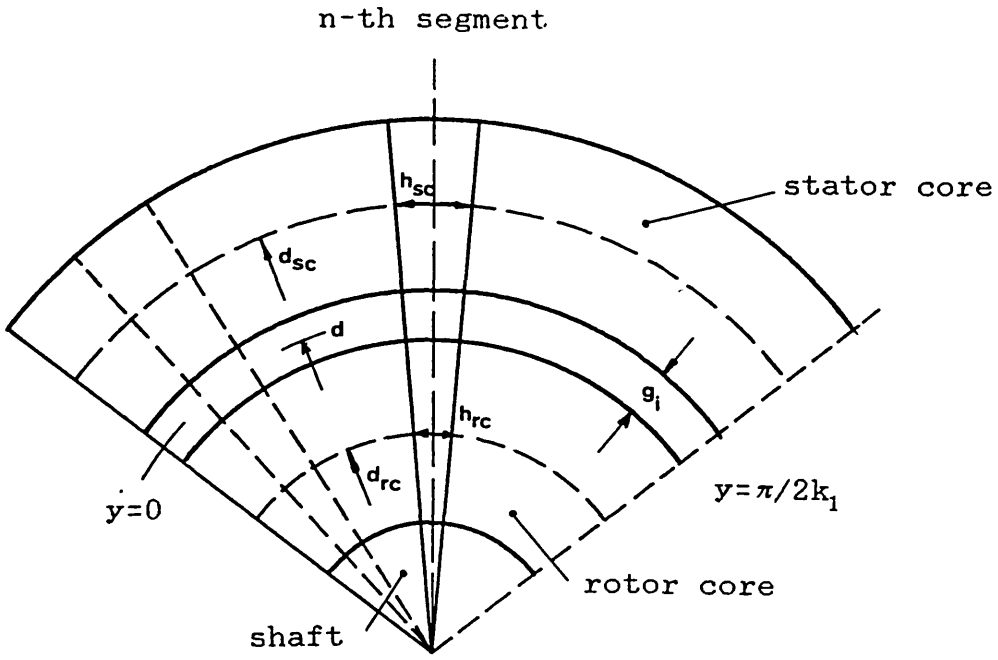


Fig.8.5: Axial cross section: core MMF calculation

the n-th core segment is given, in the i-th band, by

$$\hat{\Phi}_{cni} = (a_i/k)\,\hat{B}_{g_i} \sin(n\pi/2N) \quad . \tag{8.18}$$

The flux density in this segment is then

$$\hat{B}_{cni} = \hat{B}_{g_i}/(k_1 d_c) \sin(n\pi/2N) \quad , \tag{8.19}$$

where d_c is the effective mean depth of the back-iron, taking into account any ventilation holes. It is assumed that the flux distributes itself uniformly over the cross-sectional area of the core. As above, the field strength (H_{cni}) is obtained from the magnetisation curve, and the MMF becomes

$$F_{cni} = H_{cni}\, h_c \quad , \tag{8.20}$$

where the path length h_c is given, from Fig.8.5, by

$$h_c = d_c/(4v_{k1}N) \ . \tag{8.21}$$

The total stator and rotor core MMFs are the sums of the segmental components. For the stator,

$$F_{sci} = h_{cs} \sum_{n=1}^{N} H_{scni} \ , \tag{8.22}$$

while, for the rotor,

$$F_{rci} = h_{cr} \sum_{n=1}^{N} H_{rcni} \ , \tag{8.23}$$

In practice, a figure of N=9 was deemed acceptable, although this could be increased as required.

The total MMF required in the i-th band of the machine is then given by

$$F_i = F_{sti} + F_{rti} + F_{sci} + F_{rci} + F_g \ , \tag{8.24}$$

where

$$F_g = \sqrt{2} \left| \bar{J}_s^{k1} \right| \ . \tag{8.25}$$

The i-th band saturation factor is then

$$f_{sat,i} = F_i \ / \ F_g \ . \tag{8.26}$$

The fundamental-frequency iron losses in the stator teeth and core are calculated from the respective flux densities using specific loss figures supplied by the lamination manufacturer.

It is interesting to note that the division of the machine into axially-distributed bands provides a simple method of accounting for the flux density variations in the iron produced by the rotor skew. Suppose the number of bands is increased until the axial variation in flux over each band becomes insignificant. The core and teeth fluxes are then piecewise constant, enabling the magnetic-circuit calculations to be repeated at any speed. It is a simple matter to specify high inter-ring resistances for the additional band boundaries; in this way it is also possible to include circumferential inter-bar currents arising from imperfect bar-iron insulation [29,30].

Note, however, that at speeds other than synchronous it is important to employ the above calculations as part of an iterative procedure, since the high flux levels at the ends of the machine [16,21] may result in heavy saturation of the core and teeth. The following procedure is suggested. First, the airgap flux density is calculated on the basis of infinite iron permeability. A different saturation factor for each band is then determined following the method outlined above. Updated coupling impedances are obtained from the modified airgap lengths, and the flux densities are recalculated from the revised currents. Improved saturation factors are then obtained and the procedure repeated until the solution converges. It is strictly necessary to adopt such a technique even when considering only the stator-driven airgap field, although only a single iteration is included in the present software, as described in Section 3.4.

8.4 Inter-ring effects

Having developed and verified an analytical technique capable of modelling induction machines with inter-rings, it is appropriate to attempt to assess the consequences of their inclusion in the basic design.

An extensive literature survey revealed only two papers on the subject of machines with inter-rings. Smikal [31] likened the phenomenon of circumferential current flow from bar to bar along a single inter-ring positioned midway along the rotor core to a deep-bar effect, giving improved starting performance. He developed an approximate equivalent circuit derived by considering the principal harmonic components of airgap flux and rotor current. A coupling-impedance approach was recently presented by Chen Li-Ren, [32] who showed that the addition of a single inter-ring increased the torque over the entire motoring speed range, the effect being more marked in machines with higher principal pole numbers. He also observed that the starting torque varied somewhat with inter-ring resistance, and that, as far as the principal harmonic torque was concerned, the effect of an ideal bar-to-bar short circuit at the middle of the machine (zero inter-ring resistance) was to reduce the effective skew to half its actual value. These conclusions can be verified here using the analysis of Section 3.

Consider a skewed-rotor machine incorporating one inter-ring of negligible width and depth, positioned at the axial centre of the rotor core. The band details are as follows

$$N_b = 2 \; ;$$
$$a_1 = a_2 = w/2 \; ; \qquad (8.28)$$
$$x_1 = -w/4 \; ; \; x_2 = w/4 \; .$$

Axial symmetry of the cage means that a simpified expression for the effective stator coupling impedance may be derived. From eqns.3.56 and 3.79,

$$\bar{Z}^k_{sm,r1} = K^k_1 \, \bar{Z}^k_{sr}/2 \; e^{j\theta} \; ; \; \bar{Z}^k_{sm,r2} = K^k_1 \, \bar{Z}^k_{sr}/2 \; e^{-j\theta} \qquad (8.29)$$

and

$$\bar{Z}^k_{r1,sn} = K^k_1 \, \bar{Z}^k_{rs}/2 \; e^{-j\theta} ; \; \bar{Z}^k_{r2,sn} = K^k_1 \, \bar{Z}^k_{rs}/2 \; e^{j\theta} \; , \qquad (8.30)$$

where

$$\theta = (kw/4) \tan\gamma = k\delta \, /4 \; . \qquad (8.31)$$

δ is the circumferential rotor skew. The ν_k-th harmonic skew factor for each band is then

$$K^k_1 = (\sin\theta)/\theta \qquad (8.32)$$

The rotor-rotor impedances are defined by eqn.3.99 :

$$\bar{Z}^k_{r1,r1} = \bar{Z}^k_{r2,r2} = \bar{Z}^k_{rr}/2 - \bar{Z}^k_{r1,r2} \; , \qquad (8.33)$$

where

$$\bar{Z}^k_{ri,ri} = \frac{j\omega\mu_0 w\pi d}{N_r g} \, s_k \left[1 - \frac{2N_r b_r}{3\pi d} \sin^2\left(\frac{k\lambda_r}{2}\right) \right]$$

$$+ 4 \, \bar{Z}^k_b \sin^2(k\lambda_r/2) + 2 \, \bar{Z}^k_{er} \; , \qquad (8.34)$$

and

$$\bar{Z}^k_{r1,r2} = \bar{Z}^k_{r2,r1} = - \, \bar{Z}^k_{a1} \; . \qquad (8.35)$$

$\bar{Z}^k_b$ is the impedance of a single bar, as given by eqn.3.93, while $\bar{Z}^k_{a1}$ is that of a single segment of inter-ring. The two

by two rotor-rotor impedance matrix may be inverted explicitly to give the admittance components $\bar{W}^k_{ri,rj}$. The resulting expressions can then be substituted, along with eqns.8.29 and 8.30, into eqn.3.10 to give

$$\bar{Z}_{m,n} = \bar{Z}_{sm,sn} - \sum_{v_k} \frac{[K_1^k]^2 \; \bar{Z}^k_{sr} \; \bar{Z}^k_{rs} \; [\bar{Z}^k_{rr} + 4 \; \bar{Z}^k_{a1} \cos^2\theta]}{[\bar{Z}^k_{rr}]^2 + 4 \; \bar{Z}^k_{rr} \; \bar{Z}^k_{a1}} \; . \tag{8.36}$$

If the inter-ring forms an ideal short circuit, i.e., $\bar{Z}^k_{a1}=0$, eqn.8.36 reduces to

$$\bar{Z}_{m,n} = \bar{Z}_{sm,sn} - \sum_{v_k} [K_1^k]^2 \; \frac{\bar{Z}^k_{sr} \; \bar{Z}^k_{rs}}{\bar{Z}^k_{rr}} \; . \tag{8.37}$$

For a machine without inter-rings skewed by δ_0, the effective coupling impedance $\bar{Z}'_{m,n}$ is given by eqn.3.11

$$\bar{Z}'_{m,n} = \bar{Z}_{sm,sn} - \sum_{v_k} [K_0^k]^2 \; \frac{\bar{Z}^k_{sr} \; \bar{Z}^k_{rs}}{\bar{Z}^k_{rr}} \; , \tag{8.38}$$

in which

$$K_0^k = \sin(k\delta_0/2) \; / \; (k\delta_0/2) \; . \tag{8.39}$$

By comparing eqns.8.42 and 8.43, it can be seen that the two impedances $\bar{Z}_{m,n}$ and $\bar{Z}'_{m,n}$ are equal if

$$K_1^k = K_0^k \; , \tag{8.40}$$

i.e., if

$$\delta_o = \delta/2 \; . \tag{8.41}$$

Eqn.8.41 verifies that the addition of a single inter-ring of zero impedance is equivalent to reducing the skew to half its original value.

The effect of inter-ring resistance on starting performance is illustrated in Fig.8.6 for a 12-pole machine with three inter-rings and a skew of four stator slot pitches. Also indicated for reference purposes are the starting torques for similar machines from which the inter-rings have been removed and the skew reduced. As expected, the starting torque at low ring resistances approximates to that obtained in a single-band machine skewed by one stator slot pitch. The standstill torque is a maximum for ring resistances of approximately $3\times10^{-3}\Omega$; beyond this value the torque falls off sharply as the ring currents decrease. Complete torque-speed characteristics for the single- and four-band machines at this value of inter-ring resistance are shown in Fig.8.7.

It would seem that there is little point in including inter-rings solely as a method of improving steady-state performance, since the above results indicate that it is possible to achieve similar effects simply by reducing the skew and increasing the bar and end-ring resistances. In terms of higher-order harmonic reduction, the addition of inter-rings means that it is, in fact, necessary to increase the skew by way of compensation. Eqn.3.8 implies that the magnitude of the ν_k-th harmonic loop current in the i-th band is proportional to the i-th band skew factor, defined by

$$K_i^k = \frac{\sin\{\frac{ka_i}{2}\tan\gamma\}}{\frac{ka_i}{2}\tan\gamma} = \frac{\sin\{\frac{ka_i\delta}{2w}\}}{\frac{ka_i\delta}{2w}} \quad . \qquad (3.51)$$

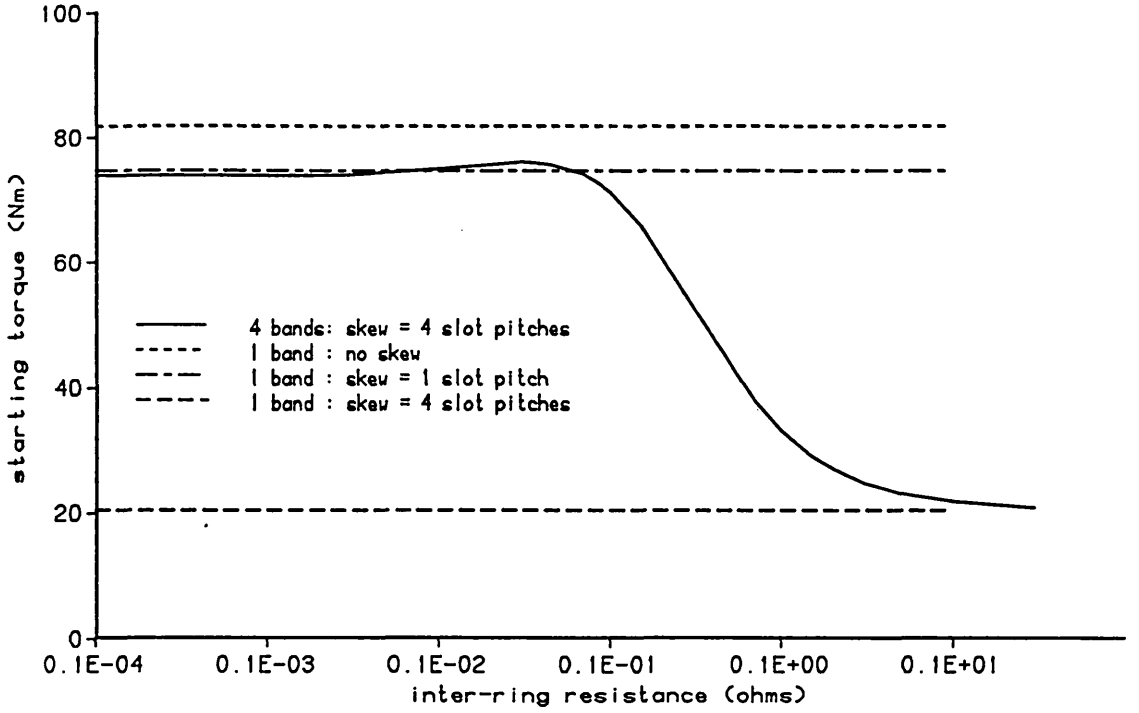


Fig.8.6: Effect of inter-ring resistance on starting torque

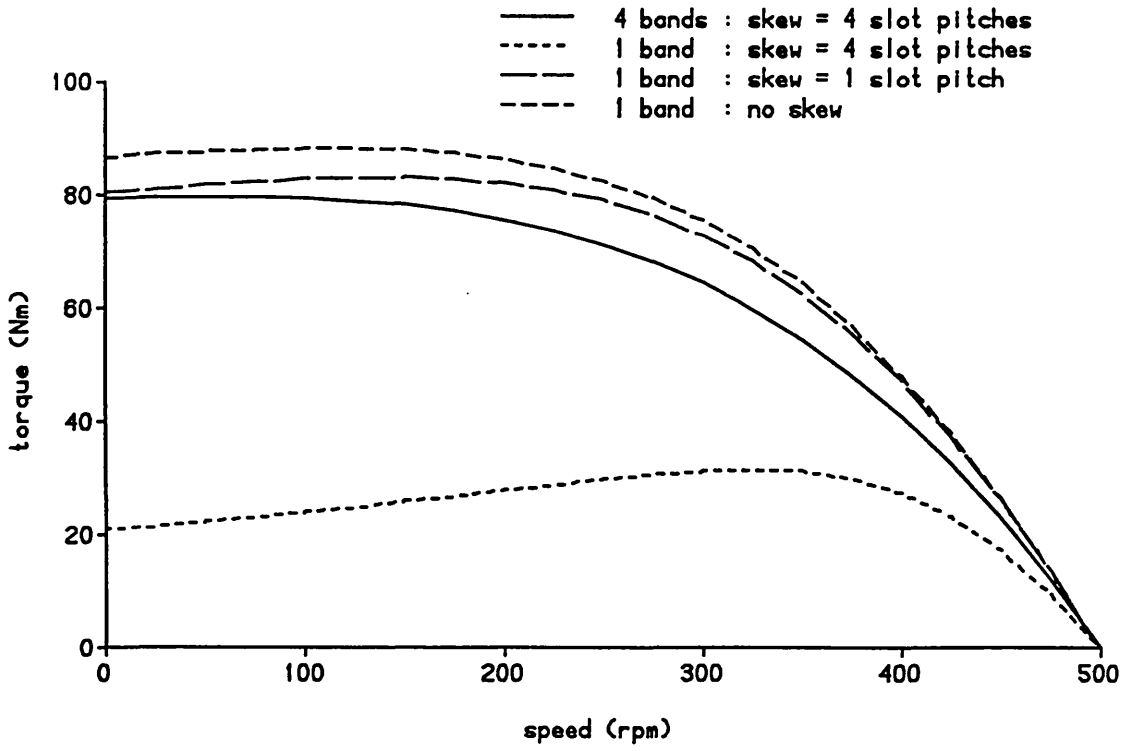


Fig.8.7: Inter-ring effects : torque-speed characteristic

If the N_b bands are each of equal width, $a_i = w/N_b$ and

$$K_i^k = \frac{\sin\{\frac{k\delta}{2N_b}\}}{\frac{k\delta}{2N_b}} \quad . \tag{8.42}$$

In order to 'skew out' the ν_k-th harmonic current, it is necessary to choose δ such that

$$K_i^k \simeq 0 \ , \tag{8.43}$$

implying that

$$k\delta/\ (2N_b) \simeq n\pi \qquad \text{for } n = 1,2,3 \ldots, \tag{8.44}$$

i.e.,

$$\delta = 2n\pi N_b \ / \ k \ . \tag{8.45}$$

The total amount of circumferential skew should therefore be proportional to the number of bands, if the desired reduction of unwanted harmonic currents is to be maintained. In all but the shortest of Bull's machines, criterion 8.45 is obeyed, since

$$\delta = \lambda_s \ N_b \ . \tag{8.46}$$

According to Bull, inter-rings are employed for noise-reduction purposes, and are incorporated into each high-torque machine in the lift-application range. High sound emission levels are particularly troublesome in the case of two-speed doubly-wound machines. Typically, the normal-speed winding has six poles, and the low-speed twenty four. The addition of one or more symmetrically-positioned inter-rings is said to reduce the objectionable audible

whine which occurs when the machine is switched from the six- to the twenty-four-pole connection. As mentioned in Section 3.1, the number of inter-rings specified for different designs depends upon the core length. The longest machines have three additional rings; the shortest, only one.

It would appear that these design features have been arrived at purely by experiment, in the absence of any relevant theoretical background. Although a thorough study of the phenomenon of noise radiation from induction machines is beyond the scope of this project, it is nevertheless appropriate to offer a possible explanation for the reduction in sound levels.

In general, the most important source of airborne noise in electrical machines is the radial vibration produced by the magnetic forces of attraction between the stator and rotor cores. At any point on the airgap surface there exists a radial force per unit area whose magnitude is given by

$$p_r(x,y,t) = [b_s(x,y,t) + b_r(x,y,t)]^2/2\mu_0 \ . \qquad (8.47)$$

If the flux were sinusoidally distributed, and if there were no flux pulsations, the radial force wave would itself be sinusoidal with twice as many poles of force as there are magnetic poles. In practice, however, there is also the myriad of harmonic flux-density waves to consider, each of which produces force waves of a particular wavelength. Vibration and excessive noise occur when the frequencies of the exciting forces are near to the natural frequencies of the machines concerned.

Slot skewing is an established method of decreasing vibration [33], since it introduces phase angles between the radial forces at different axial positions, reducing the

average exciting force. It has been pointed out, however, that such phase differences may result in the so-called transverse vibration of the stator core [20], the resultant displacement curve having maximum and minimum values at the ends of the machine, and a point of inflection at the axial centre. Fig.8.8 illustrates the variation in radial force per unit area due to the princpal harmonic component of airgap flux at each end of a non-inter-ring version of the 4-pole prototype machine. Instantaneous forces were calculated from the resultant of the stator- and rotor-driven airgap flux-density waves by substituting t=0 into eqns.3.148 and 3.150. Note that the force wave has eight poles, as expected, and that the axial variation in exciting force is negligible at rated speed, becoming increasingly apparent as the principal slip increases.

A developed three-dimensional representation of the radial force distribution is shown in Fig.8.9. The 'surface' formed by the axial and cicumferential contours may be imagined to be moving in the positive y direction at the synchronous speed of the principal harmonic (1500 rpm). If the skew were reduced to zero, the axial contours would be straight lines, since the phase difference between the stator- and rotor-driven MMF waves would not vary along the length of the core. The effect of introducing a single inter ring and doubling the skew is illustrated in Fig.8.10. Large peaks in the force waves now occur at two axial positions as a result of the re-distribution of airgap flux in each half of the machine.

In terms of transverse vibration, there will now be two nodes and three stationary points in the deflection curve, resulting in a shorter vibration wavelength and an increase in the frequency of the radiated sound. It is possible that

such an increase in vibration mode number [33] would avoid the natural resonant frequency of the stator, accounting for the fact that more inter-rings are required to achieve the same noise-reduction benefit as the core length increases. Although transverse vibration is said to produce objectionable noise only in long machines [20], it is perhaps significant that, in the square-frame design adopted by Bull, the stator may well be more flexible than usual since the laminations themselves form the outer frame, there being little extra stiffening material to restrict radial movement.

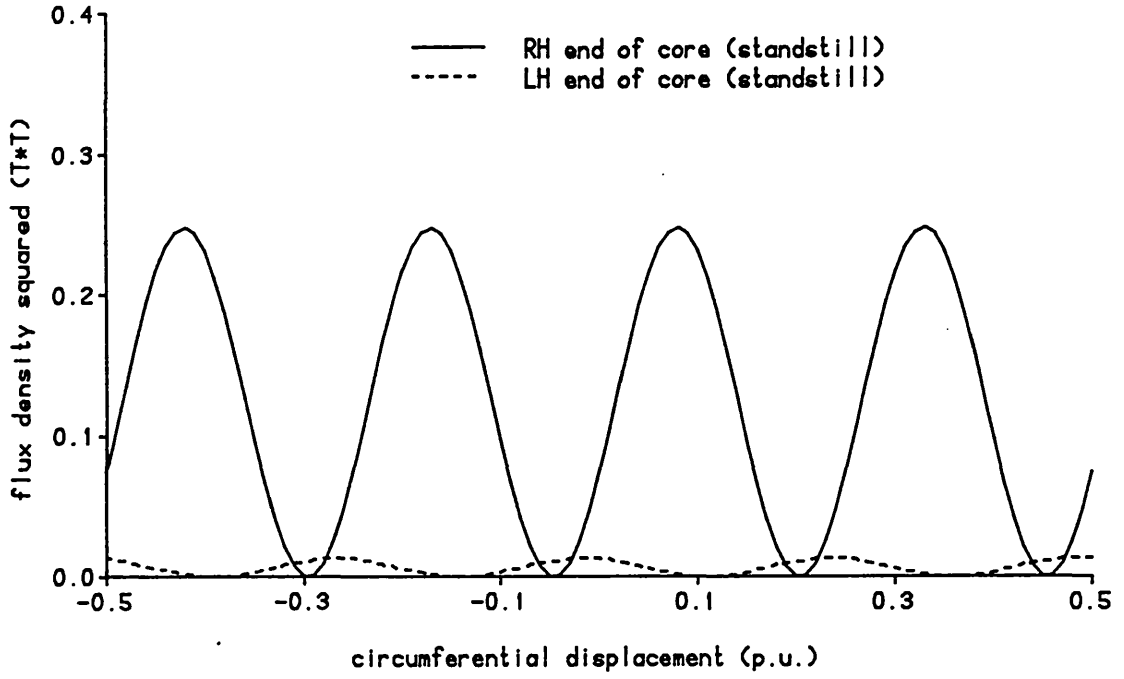


Fig.8.8a: Principal harmonic radial force wave

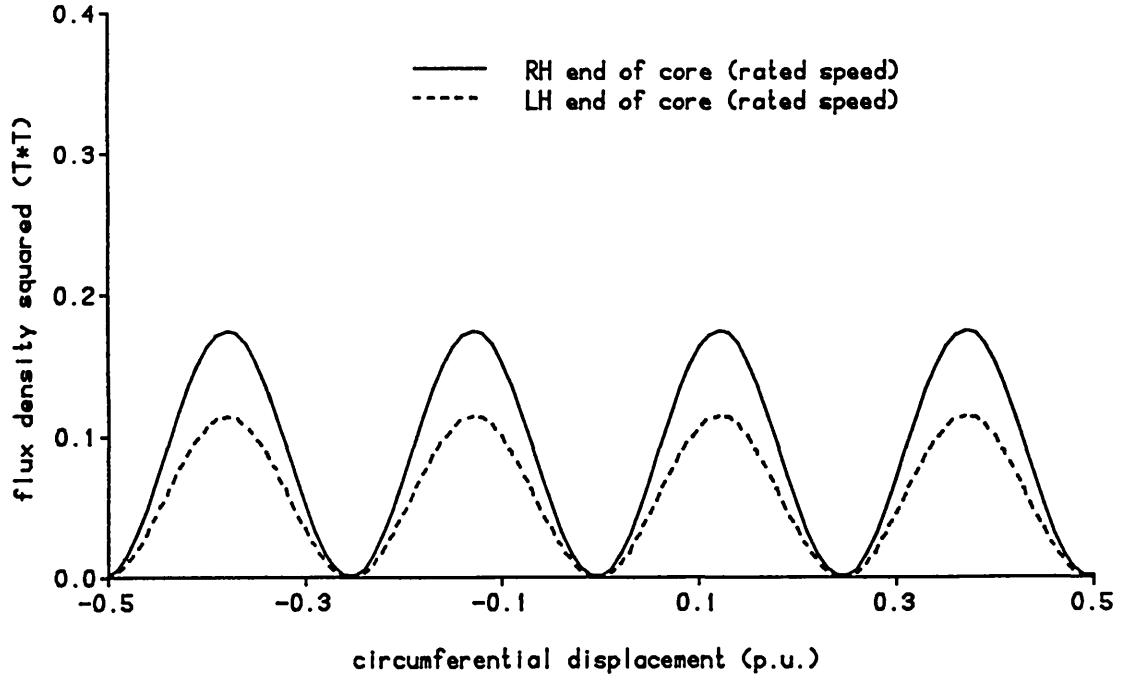


Fig.8.8b: Principal harmonic radial force wave

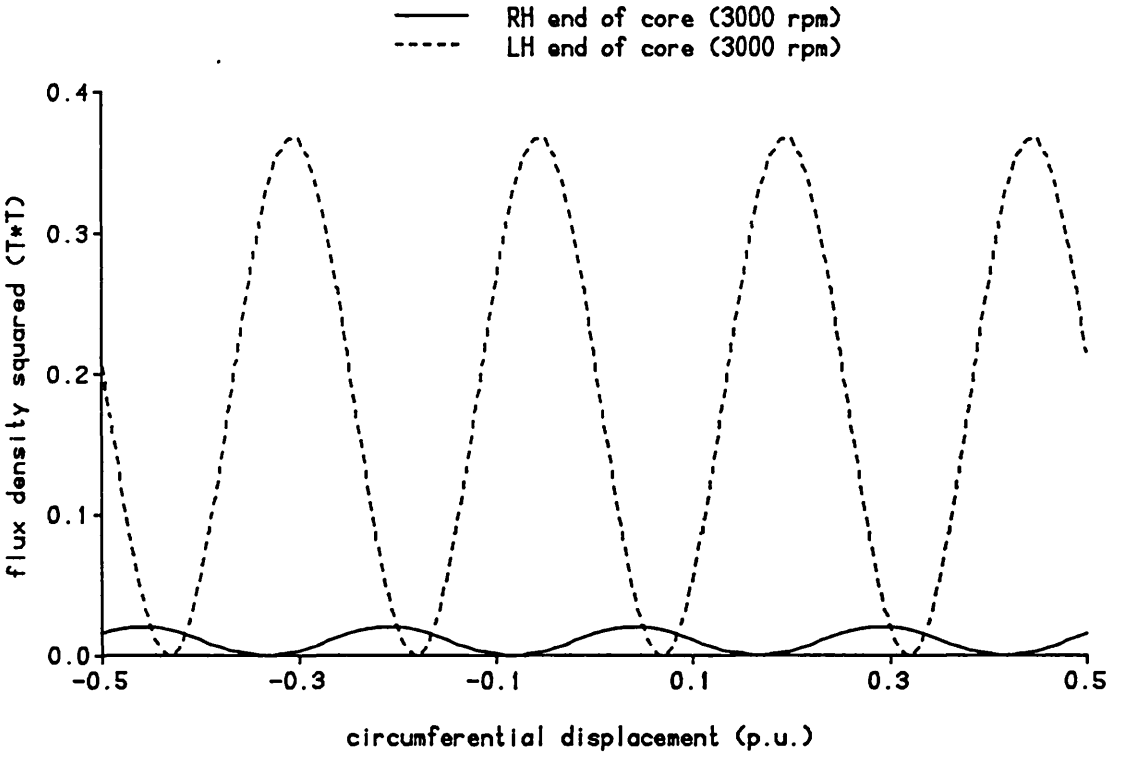


Fig.8.8a: Principal harmonic radial force wave

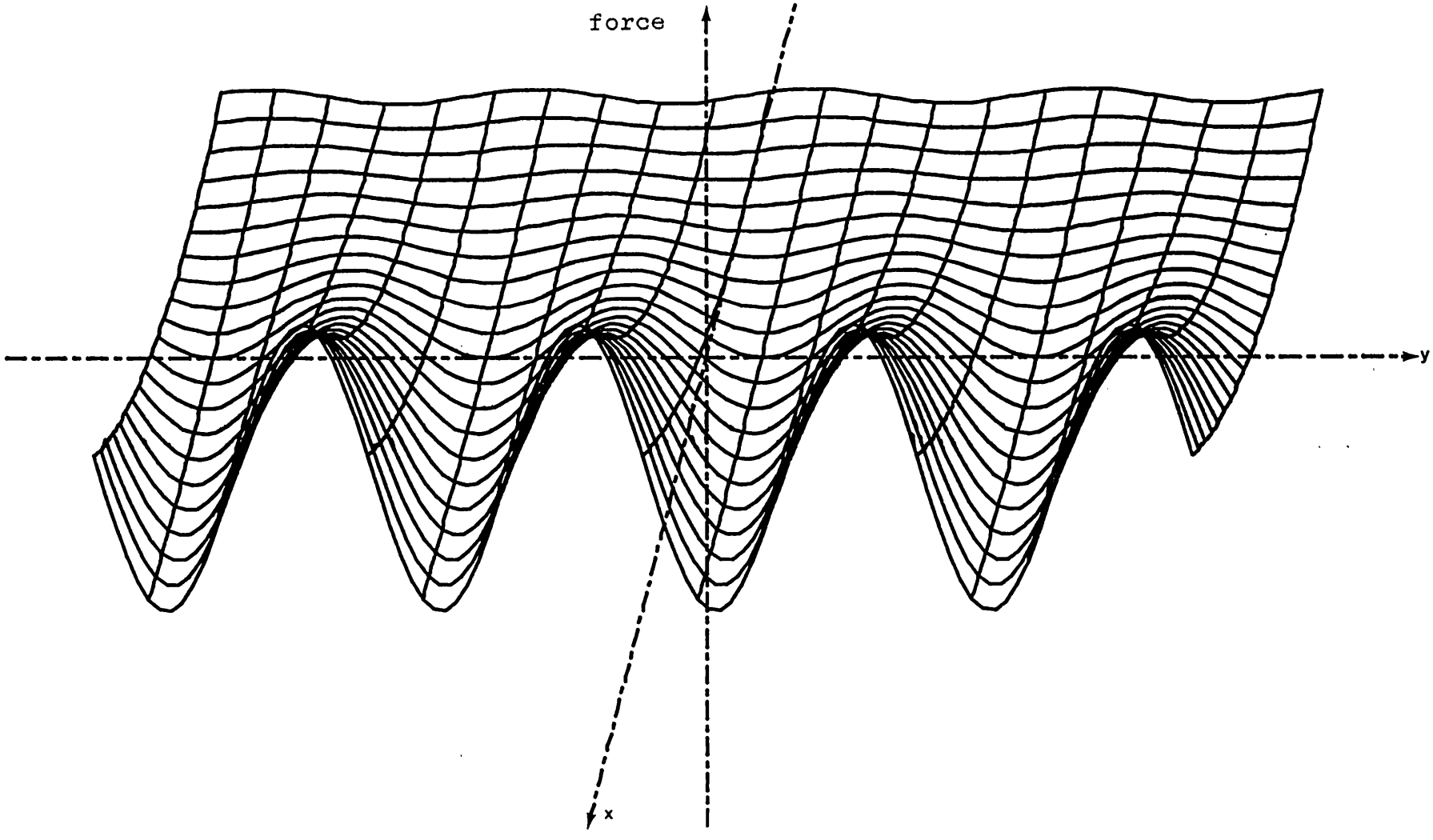


Fig.8.9: Three-dimensional representation of radial force wave

4-pole machine : no inter-rings : 3000 rpm

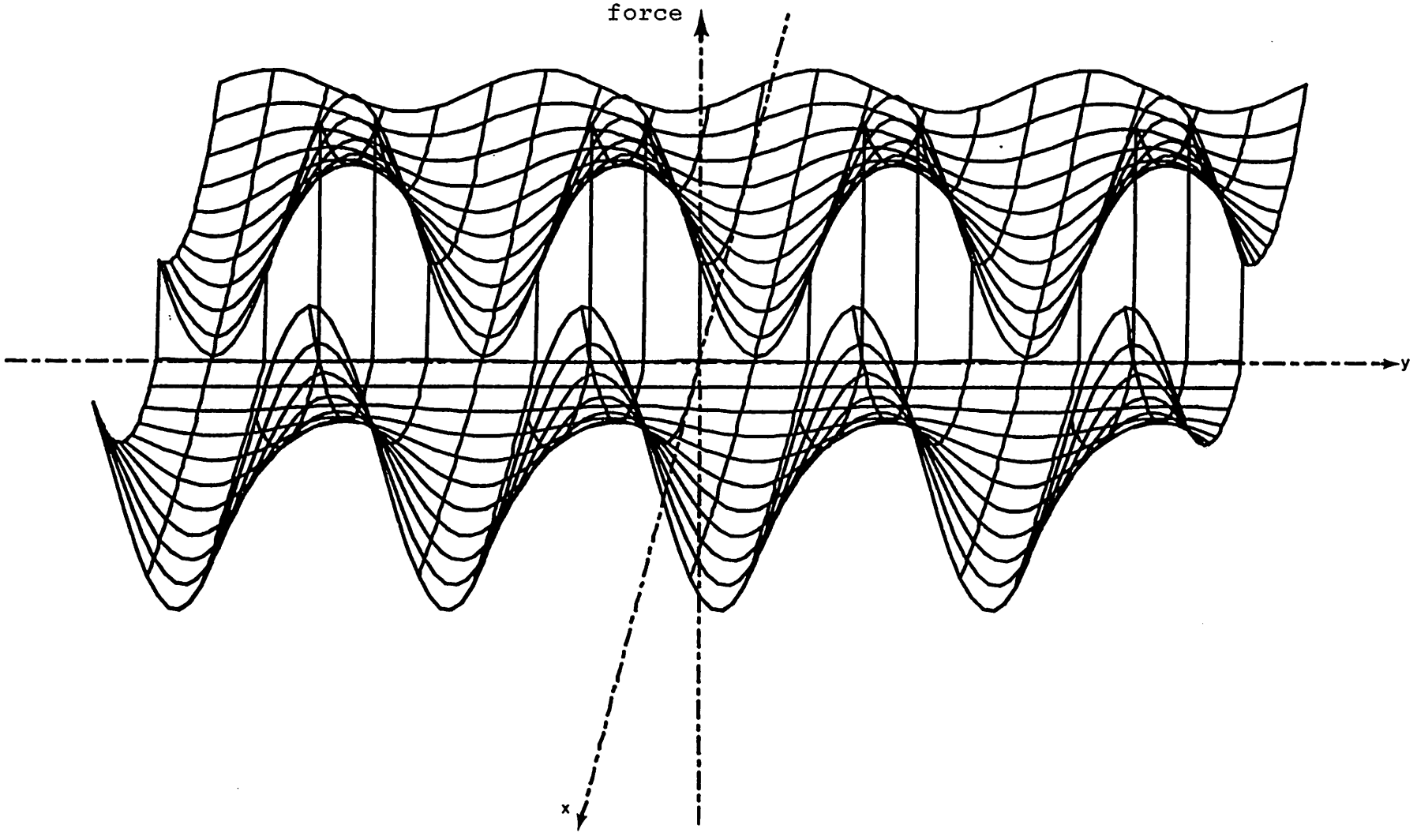


Fig.8.10: Three-dimensional representation of radial force wave
4-pole machine : 1 inter-ring : 3000 rpm